Innovations in pulsed plasma thrusters to enable CubeSat science missions

Paige Northway

A dissertation
submitted in partial fulfillment of the
requirements for the degree of

Doctor of Philosophy

University of Washington

2020

Reading Committee:
Robert Winglee, Chair
Michael McCarthy
Erika Harnett

Program Authorized to Offer Degree:
Earth and Space Sciences

University of Washington

Abstract

Innovations in pulsed plasma thrusters to enable CubeSat science missions

Paige Northway

Chair of the Supervisory Committee:
Robert Winglee
Department of Earth and Space Sciences

CubeSats and other small satellites in the 3-25 kg range are increasingly able to conduct meaningful science through advances in technology and miniaturization. However, much of the proposed science requires satellite mobility, which has advanced more slowly due to constraints on CubeSat launches. Pulsed Plasma Thrusters (PPTs) are a potential means of propulsion for these satellites that do not require fluid or gas tanks and feeds and are relatively compact. This makes them an ideal candidate as a low risk propulsion system for secondary payloads capable of passing safety concerns related to launch. Previously, the specific thrust, or thrust output per

power input (mN/kW) of PPTs developed for space flight was low for the desired propulsion applications. This work examines the development of a PPT specifically for CubeSat propulsion. It also investigates how several science questions could be answered with these advances, with examples of missions to the asteroid belt and Europa. It is shown that the power, geometry, and propellant are influential factors that can lead to substantial gains in thruster performance. Where Teflon™ has been the propellant of choice for previously launched PPTs, the novel use of solid Sulfur propellant is demonstrated with a twofold increase in specific thrust, which is the highest of any material tested in this study. Furthermore, a switch from smooth to serrated coaxial electrodes provides an increase in the specific thrust by up to an additional factor of 2. These changes bring the current test system capabilities to 45 mN/kW with a specific impulse of 1200 sec. This provides the opportunity for CubeSat missions to execute orbital maneuvers with changes in velocity on a range from 50 to 500 m/s. A fully integrated flight model was built and tested to overcome issues arising from the transition from a benchtop system to a CubeSat formfactor and then further tested for launch and space environment compatibility. The miniaturized flight model achieves 25 mN/kW performance and is being tested on the University of Washington built HuskySat-1 3U+ CubeSat, which was launched Nov 2nd 2019 and deployed January 31st 2020.

Table of Contents

Table of Figures

Chapter 1. Introduction

This chapter defines CubeSat and Smallsat and reviews missions as prior art. It establishes current applications and capabilities as a basepoint to motivate further advances in hardware to extend science capabilities. Examples of past and planned CubeSat missions are provided with a particular interest in capabilities and successes enabled by onboard propulsion. To set the stage for discussions on propulsion and introduce pulsed plasma thrusters, the chapter also includes background information on propulsion metrics and current state-of-the-art CubeSat propulsion.

1.1 Defining CubeSats and SmallSats

For the purpose of this paper, the term CubeSat is used for any satellite conforming to the CubeSat formfactor, which requires some multiple, or Unit (U), of "cubes" ~10 cm per side. A satellite that is ~20 x 10 x 10 cm is then 2 of these units, or a 2U CubeSat. CubeSats range in size from 0.25U to 12U, with a proposed 27U CubeSat being 3U x 3U x 3U.

CubeSats are also distinguished by having rails on four edges with flat square ends. The rail system is the interaction point between the CubeSat and the deployer. The standardization of this interaction combined with the standardized cube shape allows CubeSats to be designed in detail prior to securing a launch vehicle. This feature of CubeSats enables groups with varied or uncertain funding like university teams to reach a mature design in order to secure launch funding, providing easier access to space for these groups.

The standard mass of a CubeSat is ~1.33 kg per U, but the mass may vary widely from the standard. Thus, the proposed range in mass of CubeSats is roughly 0.5 kg to 40 kg. This range spans portions of the Pico, Nano, and Micro classifications defined in Table 1-1. The majority of CubeSats launched to date have been 1U to 3U in size and fall into the nano satellite, or nanosat, classification.

Satellites that are smaller than the typical CubeSat are also being produced and launched. PocketCubes and ThinSats are two examples of smaller satellite standards that are 5x5x5 cm and a deployable 10x10x1 cm, respectively. At the close of 2019, ten PocketCubes and twelve ThinSat boards had been launched. Only six of the PocketCube satellites reported any contact [Kulu].

Smallsat is sometimes used as a descriptor for any satellite under 500kg. In this work, the term Smallsat is used for any satellite between 3 and 25 kg. CubeSats require a particular formfactor and can theoretically span a wide range of masses. Smallsats overlap considerably with CubeSats but have a smaller mass range and are not required to be a particular shape. The distinction is useful as CubeSats at the upper end of the mass range start to have the mass and volume budget for higher power electric propulsion systems or more complex chemical propulsion systems.

Table 1-1 Classification of Satellites by Mass

Classification	**Mass (kg)**
Large	>1000
Medium	500 - 1000
Mini	100 - 500
Micro	10 - 100
Nano	1 - 10
Pico	0.1 - 1
Femto	<0.1

1.2 Increasing utility and use of small satellites motivating need for improved propulsion

Small satellites of the nanosat and microsat scale are a growing tool in space exploration and industry. Current and ongoing component miniaturization is further enabling the use of small satellites in far reaching applications, and NASA Technology Roadmaps and solicitations like the Europa CubeSat and CubeQuest Centennial Challenge exemplify the interest in development of propulsion systems and novel small satellite applications. A review of current Smallsat science missions and technologies is presented to motivate the development of additional propulsion technology, which provides an increased breadth of possible missions.

1.2.1 Broad growth in launched nano- and pico- satellites.

CubeSats have been launched for the last 20 years. A marked increase in the overall number of launches and commercially built CubeSats started around 2013, as shown in Figure 1-1. The figure also shows the general increase in small satellite launches holds true not just for Universities and private industry but also for military, non-profit, space agencies, and even K-12 schools. A total of 1681 CubeSats and other Nano- and Pico-class satellites have been launched or are planned to launch by the end of 2020. This excludes ~70 university satellites that are scheduled to launch in 2020 but have not yet reported a launch opportunity. A large portion of the 1681 satellites are a result of commercial constellations. Planet Labs, Inc. has launched over 300 CubeSats as part of the Dove, RapidEye, and SkySat constellations, while Spire Global has launched over 100 CubeSats as part of the Lemur constellations [Kulu].

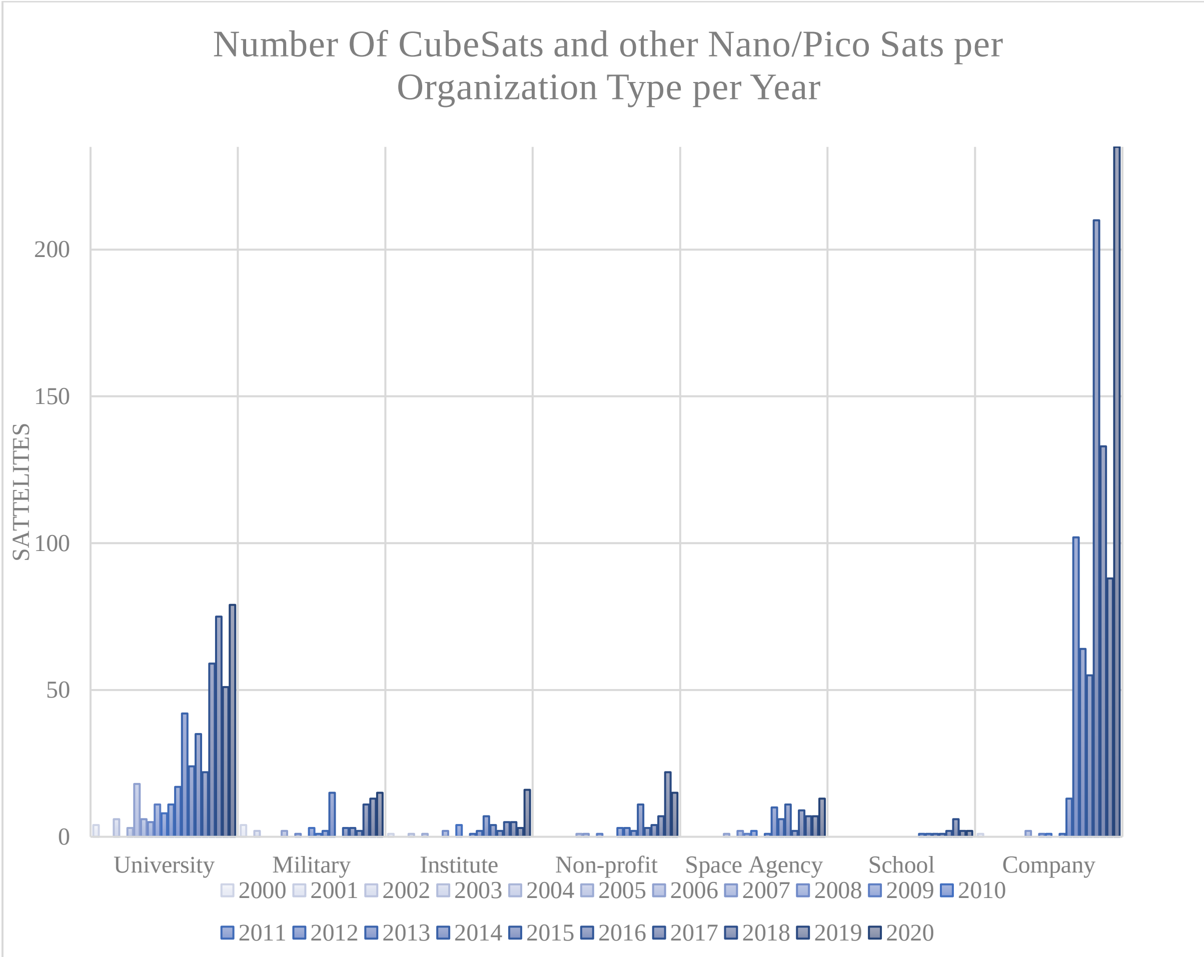

Figure 1-1 The growth of CubeSat launches across organizations: CubeSats and other <10 kg satellites launched each year since 2000 by different organizations

The nanosat.eu CubeSat database has categorized the 1200 CubeSats launched by the end of 2019 in several ways. It is important to note that the 1200 number excludes those satellites not conforming to the CubeSat standard, including ThinSats, PocketCubes, and other nanosats and picosats. The number does include satellites that were never operational and those on failed launch vehicles [Kulu]. That total number of 1200 is broken down by type of organization in and country of origin in Figure 1-2 and Figure 1-3, displaying the breadth of interest in CubeSat use.

The “mission type” characterization breaks these CubeSats into the smallest number of groups, with the groups being space science (90 CubeSats), space technology (495 CubeSats), and space activity (641 CubeSats). The space science group is composed mainly of studies of the upper atmosphere, solar and interplanetary physics, and astronomy. Space technology covers system design and verification, including RF communications, space debris mitigation and in-space propulsion, among others. Space activity is a broad group composed mainly of Earth observation satellites, but also including meteorology, telecommunications, and robotic exploration.

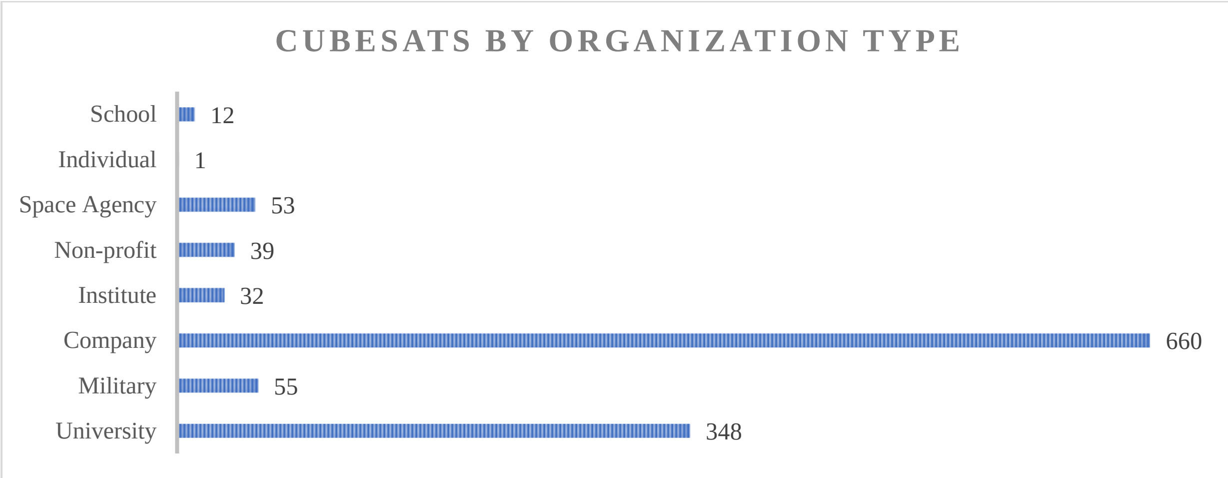

Figure 1-2 Total number of CubeSats launched by the end of 2019 by organization type

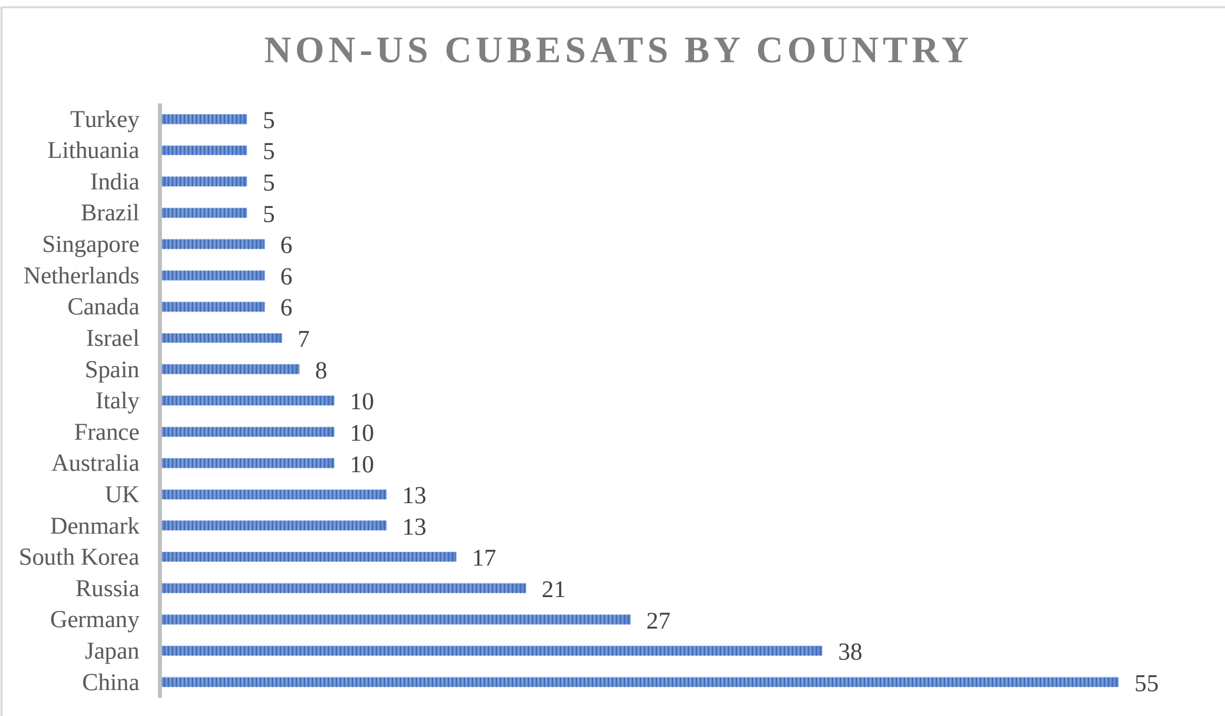

Figure 1-3 Countries that have five or more launched CubeSats, excluding those launched for US entities.

1.2.2 Opportunities from lowering costs of space access

The growth in CubeSat launches follows a growth in the general space sector, which has been contributing to more affordable space access. Recent improvements in hardware and software enable considerable capability in small packages [Behrens]. Smaller satellites cost less to develop due, in part, to smaller teams and shorter development times. Launch costs for small satellites, as secondary payloads or as one of a hundred or more payloads, scale with mass. For example, quoted launch costs from rideshare provider Spaceflight Industries for 5kg, 50kg, and 450kg satellites into low-Earth orbit are $295k, $1,750k, and $17,500k, respectively [Spaceflight]. The CubeSat standard for deployment containers further reduces costs by allowing reuse of deployers and mitigating the need for customized containers. Finally, new launch vehicles on the domestic and international stage have led to increased launch availability. New vehicles capable of launching many small satellites include Rocket Lab's Electron rocket and SpaceX's Falcon 9 rocket. The Indian Space Research Organization's PSLV rocket, while not as new, holds the record for 104 satellites deployed from the PSLV- C37 launch in 2017 [PSLV]. CubeSats launched on these rockets may obtain waivers for propulsion that are not available for launches to the International Space Station.

The lower cost and shorter timeline of small satellites has multiple benefits to space access and mission design. It provides access to space for smaller players like small companies, universities, and even high schools. This access is frequently through NASA grants, but more grants are available because of the lower cost. This lower risk on a smaller investment also allows for the undertaking of missions with a higher risk of failure. The high-risk missions, in turn, provide a testing ground for more advanced and experimental technologies. The reflectarray antennas tested on the Mars Cube One mission are an example of a space technology gaining flight heritage [Klesh]. The missions also provide an opportunity for scientific return. Some proposed science from high-risk Smallsat missions is currently not considered feasible to attain through a lower risk mission.

The small size of CubeSats and Smallsats has other advantages. They are more easily constructed in and tested in small clean room facilities. There are fewer components, which allows for more cost-effective construction of full duplicates for testing and backup. Taken a step further, small and large constellations of small satellites are more feasible. Having several of the same satellites in orbit can provide insight into the timing and physical extent of atmospheric or space weather phenomenon not characterized by single satellites. Constellations of Earth observing satellites provide higher time resolution on changing terrestrial conditions.

1.2.3 Increasing support in systems, launch, and orbit operations through industry interest

Industry interest and support has been an additional key factor of the proliferation of CubeSat launches. Pumpkin, GomSpace, Blue Canyon Technologies, Ariane Space, and ISISpace are all examples of companies that sell partial or full satellite bus systems. The advent of commercial CubeSat buses would not be possible without the CubeSat standard, and it provides the opportunity for serious science missions to focus on payload development instead of full satellite systems.

Companies including Nanoracks and SpaceFlight Inc. now provide launch coordination for small satellites. This service fills a missing link between the larger space launch operations and small customers. As early as 2020, Momentus will join the rideshare providers with the added benefit of propulsion services to deploy in a desired orbit.

Companies providing ground station networks and support, for downlinking small and large amounts of satellite data across the globe, have also grown in number and size. Notably, Amazon AWS has created a pay-per-minute ground station network linked directly to their cloud offerings. This system is beneficial to budget and schedule limited projects. The cloud base does have a potentially negative feature in X-band, or 8-12 GHz, downlink for $20 per pass, with a monthly subscription minimum. The RBC network uses over 60 antennas worldwide. [RBC Signals].

1.3 Current Propulsion and Science on CubeSats

CubeSats are already being utilized to assist in science missions both within and beyond Earth orbit. Several examples are provided to demonstrate the scope of science available on small satellites and to motivate the need for advancement in propulsion specifically designed for this class of satellites. Several very low thrust options result in extended exposure to radiation or are unable to generate the thrust for desired maneuvers. Higher thrust options are frequently not throttleable, require considerable mass and volume budgets, or have complex hardware more prone to failure.

1.3.1 CubeSats in Low-Earth Orbit

CubeSats are traditionally launched into low-Earth orbit, LEO, at altitudes of 600km or less. This guarantees a passive orbit decay within the 25 years proscribed to mitigate space debris as part of NASA-STD-8779.14b. The three following examples of CubeSat science are also considered precursors enabling further science through validation of emerging software and miniaturization of technologies:

- The MinXSS (Miniature X-ray Solar Spectrometer) 3U CubeSat carries the X123 soft X-ray spectrometer. The X123 measures solar soft X-rays in the 0.5 to 12 keV range. The data has proven comparable to that of the Geostationary Operational Environment Satellites' (GOES) X-ray sensors. The measurements are pertinent to determining solar atmospheric plasma conditions for a better understanding of solar flares. [Moore].
- ASTERIA (Arcsecond Space Telescope Enabling Research in Astrophysics) has achieved photometric precision better than 1000 parts per million per minute with an advanced system of attitude and thermal control. These capabilities enable the satellite to look for transiting planets around nearby stars. The autonomy features tested on the satellite are a benchmark for future CubeSat science missions requiring accurate pointing and/or orbits beyond Earth with limited ground communication. [Fesq]
- PolarCube is an Earth observing 3U CubeSat carrying the MiniRad instrument. MiniRad is a 118.75GHz scanning passive microwave temperature sounder. With the MiniRad instrument, PolarCube will characterize sea ice edges and concentrations in conjunction with temperature variations. [Periasamy]

In the private sector, large constellations of CubeSats in LEO from both Planet Labs and SPIRE Global image the earth in visible and IR spectrums at a high resolution with greater frequency than previously possible. These CubeSat constellations are enabling science like the monitoring of dynamic surface water bodies, as in Cooley et al., 2017, and landslide detection, exemplified in Ghorbanzadeh et al., 2019.

To date, fewer than 20 LEO CubeSats have successfully flown and published propulsion systems. Several contributing factors include short mission lifetimes not requiring propulsion, safety concerns with propulsion on secondary payloads, and the difficulty of designing small and effective low-cost propulsion systems for CubeSats. As demand increases for formation flying, extended mission lifetimes in lower orbits, and the ability to avoid collisions, propulsion is becoming more commonplace on CubeSats and microsats in LEO.

One successful example of CubeSat propulsion is the Canadian Advanced Nanospace eXperiment (CanX) program. CanX-2 comprised a 3U CubeSat with a cold-gas Nano Propulsion System [Sarda]. This module used liquid sulfur hexafluoride (SF6) propellant, which achieved a maximum thrust of 35 mN, and was estimated to deliver a total ΔV of about 35 m/s. The NANOPS was later used on nanosats CanX-4 and 5 for formation flying [Roth].

1.3.2 Landing coverage on Mars with Mars CubeSat One

MarCO, for Mars Cube One, comprises two 6U CubeSats, MarCO-A and MarCO-B. These CubeSats were launched with the NASA InSight lander in 2018 but deployed from the Atlas V booster after separation of the InSight lander. They then made their way to Mars independently using VACCO cold gas MarCO Micro Propulsion System [Klesh]. One of the propulsion modules leaked outside of specified values and had to be creatively incorporated into the attitude control loop to get the CubeSat to Mars. The MarCO CubeSats provided a near real-time relay to Earth for the landing of the InSight lander. This data arrived an hour ahead of what would have been possible using only the Mars Reconnaissance Orbiter [Klesh]. Despite the leak in the propulsion system, the successful demonstration of communication and propulsion on interplanetary CubeSats sets the stage for future science missions of this formfactor with even greater scope.

1.3.3 Asteroid science with the Mobile Asteroid Surface Scout

The Mobile Asteroid Surface Scout (MASCOT) lander is an example of science being conducted by CubeSats beyond Earth orbit. The MASCOT lander, a 12U CubeSat in a 30 x 30 x 20 cm form-factor weighing approximately 10 kg, deployed from the Hyabusa-2 spacecraft at the asteroid Ryugu in October of 2018. MASCOT has no traditional propulsion but is instead able to "jump" and adjust its position and orientation using a tungsten swing-arm.

Data from MASCOT has allowed scientists to conclude that there is no regolith on the asteroid and that the asteroid is composed mainly of two separate types of rock [Jaumann]. A similar mission is proposed in section 2.1 with a more traditional propulsion system for orbital operations and extended capabilities.

1.3.4 Lunar and deep space CubeSats on planned Artemis 1 launch

The Artemis 1 launch of the NASA Space Launch System (SLS) will carry up to thirteen 6U CubeSats with 3U x 2U x 1U envelopes and 14 kg mass. Lunar Ice Cube, NEA-Scout, and the Japanese CubeSat OMONTENASHI are three of those thirteen secondary payloads. Each of these three CubeSats utilize different propulsion methods for different goals.

- Lunar Ice Cube has proposed to use a Busek Bit-3 RF ion thruster for a low energy, nine-month, journey to the moon. After lunar orbit insertion, it will use a broadband IR spectrometer to measure the abundance and distribution of water and water components on the lunar surface. The year between deployment and reaching science orbit required by the low thrust propulsion option results in longer exposure to radiation than a higher thrust option. [Clark]

- NEA-Scout, or Near-Earth Asteroid Scout, will deploy a solar sail and use cold gas thrusters for initial propulsion maneuvers in order to travel beyond the moon to a NEA over an estimated two years. The mission involves and close (~1km) flyby to image a small NEA. The sub-100 km size range of NEAs are difficult to approach with conventional satellite missions. [Pezent]
- OMOTENASHI is a demonstration of a low-cost method for landing a small payload on the lunar surface. The payload is originally part of a 6U CubeSat. A high thrust solid rocket motor slows the descent towards the moon. The drawback to this method is the inability to use any form of active attitude control to effectively control the orientation during the rocket motor burn phase. [Hernando-Ayuso]

1.4 PROPULSION SYSTEMS BACKGROUND

The depth and breadth of research and commercially available propulsion systems for nanosat and microsat class satellites has increased significantly in the last eight years with the growth in number of launches of smaller satellites. The breadth of mission designs is aided by the breadth of propulsion types, and it is often impractical to compare any one characteristic of a propulsion system. Several pertinent characteristics are described, as well as state-of the art in development and with flight heritage. Pulsed plasma thrusters are introduced in more detail as a propulsion solution. Further advances in CubeSat propulsion enable these science goals.

1.4.1 Metrics for propulsion

Several metrics are regularly used in discussion of Smallsat propulsion systems. The **wet mass** and the **envelope** are major considerations to determine what thrusters are an option for any given mission. If a propulsion system is too heavy or too large to fit within given mass and volume budgets for the project, there is no point in exploring that system further. For electric propulsion, the **power** needed to operate the propulsion system is another early consideration. Other metrics commonly used to describe propulsion systems include efficiency, thrust, specific impulse, total impulse, impulse bit, and specific thrust. Different metrics are more pertinent and applied differently to different propulsion types. Considerations for the ability to throttle the propulsion system and required warm-up times are also important.

Efficiency of a propulsion system can refer to several measurements. Specific impulse, *Isp,* is considered a measure of fuel efficiency. A higher *Isp* corresponds to faster fuel exhaust velocity, C_e, and requires less fuel to accelerate a given mass to the same speeds. Hence, higher *Isp* means a more efficient use of fuel. *Isp*, measured in seconds, can be calculated as

$$I_{sp} = \frac{C_e}{g_0} = \frac{F}{\dot{m} g_0} \qquad \textit{Eqn 1}$$

Where g_0 is the gravitational constant, F is thrust force, and $\dot{m}$ is the mass flow rate of the fuel exiting the spacecraft. High powered electric systems can reach Isp upwards of 3000 seconds, while cold gas thrusters have Isp in the range of 40 seconds.

The above calculations apply to both chemical and electrical propulsion systems, but electric propulsion systems are unique in the need for substantial power to operate. For those systems, electric efficiency, η_e, is often a measure of the efficiency of the power processing unit (PPU). Many electric propulsion systems require high voltage stepped up from the satellite bus or battery voltage which is done with the power processing unit (PPU). Common efficiencies of PPUs are on the order of 85% or higher, depending on the voltage required.

Ionization efficiency of the fuel is not pertinent to every electric system but will be defined here as the portion of fuel expelled which is ionized. In electric propulsion systems where ions provide the majority of the thrust, neutral atoms in the exhaust add negligible thrust.

Efficiency can be taken overall or as specific to a portion of the system. System dependent, there are several other ways to categorize efficiencies. The total efficiency is given by the ratio of the kinetic power in the exhaust to the total input power:

$$\eta = \frac{\frac{1}{2}\dot{m}C_e^2}{P_{in}} \qquad \textit{Eqn 2}$$

Where $\dot{m}$ and C_e are still the mass flow rate in the exhaust and the mass average exhaust velocity. P_{in} is the total input power. Since the thrust F_T is

$$F_T = \dot{m}C_e \qquad \textit{Eqn 3}$$

The efficiency can be written as:

$$\eta = \frac{T^2}{2\dot{m}P_{in}} \qquad \textit{Eqn 4}$$

For a system in which the propulsion occurs in very short pulses, this can be written in terms of the impulse bit, I_{bit}, the mass ejected per pulse, m_{bit} , and the energy input per pulse, E, all of which can be directly measured. These variables are derived from the integral over time of those it in the previous equation as the change in time, dt, goes to zero.

$$\eta = \frac{I_{bit}^2}{2m_{bit}E} \qquad \textit{Eqn } 5$$

It is then useful to define the metric **impulse bit**, I_{bit}, as the impulse from a single pulse or firing of a propulsion system. Impulse has units of Newton-seconds. In systems designed for precision adjustments or attitude control, the minimum impulse bit is a measure of the precision with which the satellite can be torqued or propelled. Imaging systems and formation flying are examples where a small impulse is beneficial. It can be calculated as

$$I_{bit} = m_{bit}C_e \qquad \textit{Eqn 6}$$

The **total impulse**, I, is the net momentum imparted to the spacecraft over the lifetime of the propulsion system. It is defined as the integral of the thrust force over the duration of the mission:

$$I = \int T\,dt \qquad \textit{Eqn 7}$$

And can be calculated as the sum of the impulse bits of a pulsed system:

$$I = \sum I_{bit} \qquad \textit{Eqn 8}$$

Thrust, T**,** is the force the propulsion system applies on the spacecraft. Given a spacecraft mass, it can be used as an inexact analogue of acceleration. The calculation is given in equation Eqn 3 but is an important factor in smallsat mission design, as orbital maneuvers may require a higher thrust than is available with current electric propulsion methods.

The above considerations apply to both chemical and electrical propulsion systems, but electric propulsion systems are unique in the need for substantial power to operate. This is an additional consideration in what propulsion systems are an option for any given mission. When considering power, there are several additional metrics commonly discussed. **Specific thrust**, *Tsp*, is a measure of thrust output to power with units of Newtons per Watt. Thrust divided by power is unit equivalent to impulse bit, I_{bit}, divided by stored energy, E, for pulsed systems:

$$T_{sp} = \frac{F_T}{P} = \frac{I_{bit}}{E} \qquad \textit{Eqn 9}$$

The ability of a propulsion system to change the velocity of a spacecraft, or impart ΔV, is dependent on the mass of the spacecraft, and is therefore not a metric for propulsion systems, but can be calculated using the above metrics, the initial mass of the spacecraft with the propulsion system, the mass of the fuel expelled, and the rocket equation:

$$\Delta V = C_e * \ln\left(\frac{m_{initial}}{m_{initial} - m_{fuel}}\right) \qquad \textit{Eqn 10}$$

1.4.2 Ratings for propulsion technology maturity

When describing propulsion systems, it is useful to introduce the Technology Readiness Level (TRL) assessment. The TRL of a system is measure of the maturity of that technology. The scale spans from TRL 1, as the lowest maturity, up to TRL 9. The descriptors in Table 1-2 are the requirements to be considered a particular TRL. Having met that standard does not move a technology into a higher level but qualifies it for that level.

Table 1-2 Technology Readiness Level (TRL) definitions

TRL	Description
1	Basic principles observed and reported
2	Technology concept and/or application formulated
3	Analytic and experimental critical function and/or characteristic proof-of-concept

4	Component and/or breadboard validation in a laboratory environment
5	Component and/or breadboard validation in a relevant environment
6	System/subsystem model or prototype demonstration in a relevant environment
7	System prototype demonstration in a space environment
8	Actual system "flight qualified" through test and demonstration (ground or space)
9	Actual system "flight proven" through successful mission operations

The wording in Table 1-2 comes from NASA directorates [Dunbar]. The scale describes the level of verification done on the system as the system development occurs. In TRL 1 and 2, the idea and design are still very speculative, and are being studied entirely on paper. TRL 3 is a switch to some proof-of-concept that the underlying ideas are valid. TRL 4 and 5 move the system into an early prototype where components can be tested for function independent of each other. To move into TRL 6 and 7, the testing of more complete prototypes needs to occur in space-like environments. For TRL 8 and 9, testing must occur on the completed system as it would operate on a satellite. At TRL 9, the system has been flight proven.

For the systems described in the following section, anything below a TRL 8 has likely not been assembled in a flight model. The move to an actual system is a difficult step that sets the two highest TRLs apart from the rest and is crucial in order for a propulsion system to be considered available.

1.4.3 Current state of the art in nanosat propulsion systems

The described systems span a broad range of propulsion types, including chemical, electric, and propellant-less systems. Only thrusters with a total volume of ~3U or less are considered for this comparison, as larger thrusters are not feasible for Smallsat science missions. In this highly dynamic field, these details are relevant as of the conclusion of 2019. The predominant types of propulsion and their range of characteristics are outlined in Table 1-3.

Commercial production of thrusters has recently led to the qualification of several feed systems, valves, and pressure tanks to fly as secondary payloads. This type of qualification is generally not feasible within the scope of thrusters developed by universities. Previously, most CubeSat propulsion systems were limited to solid fuel and cold gas systems in order to pass the safety requirements of available launch providers.

Table 1-3 A selection of CubeSat propulsion types with ranges for published capabilities [Propulsion].

Type	Specific Impulse (s)	Thrust	Power (W)
Hydrazine	200-235	0.5 -30 N	10-40
Cold Gas	40-70	0.01 - 10 N	~2
Alternative Propulsion	190 -250	0.1-27N	1-25
Pulsed Plasma and Vacuum Arc thrusters	500-3000	1 - 1300 µN	2-20
Electrospray propulsion	500-5000	10 - 120 µN	1.5-40
Hall Effect Thrusters	1000-2000	10 - 50 mN	175-200

Ion Engines	1000-3500	1 - 10 mN	40-60
Solar Sails	-	0.25 - 0.6 mN	-

Hydrazine thrusters have heritage on larger missions but have not been demonstrated on CubeSat missions. They are capable of comparatively high thrust, but the toxicity of the propellant makes them difficult to work with in a research setting and requires more mass to ensure safe handling and operation.

Alternative, sometimes called "green," propulsion, is an alternative to hydrazine. Ammonium DiNitramide (ADN) and Hydroxyl Ammonium Nitrate (HAN) are the two main "alternatives." Both alternatives have a greater fuel density, higher Isp, and are less toxic, making them superior all around. Many green monopropellant thrusters are available, but the 1N HPGP thruster from Bradford ECAPS has significant flight heritage with 46 thrusters in orbit. The HPGP system, as with most hydrazine and alternative propulsion systems, is not currently packaged in a modular CubeSat form [Bradford]. The NanoAvionics Enabling Propulsion for Small Satellites system (EPSS) is a CubeSat ADN thruster that was tested to TRL 7 on a 3U CubeSat in 2017 [NanoAvionics].With the exception of cold gas thrusters, this was considered the first ever test of chemical propulsion on a CubeSat The Hydros system from Tethers Unlimited is also considered and alternative propellant with water as fuel. It has a 4U volume, but it also has a total impulse of more than 2000 Ns and a completely safe fuel [Tethers].

Cold gas thrusters operate using energy stored in pressurized gas. The expansion out of the nozzle of the pressurized gas creates thrust. Cold gas thrusters are popular for being relatively simple and only requiring power for valve operations. They have the lowest Isp of any thruster type but produce significant thrust. Fuel for cold gas thrusters is generally an inert gas, commonly N_2. The MarCO CubeSats used a Vacco MiPS cold gas thruster with R236FA propellant commonly found in refrigerants. Several other cold gas thrusters for CubeSat propulsion are commercially available [Vacco].

Resistojet, or warm gas, thrusters, are essentially cold gas thrusters with a heating element to increase the Isp of the thruster. The added electronics increase the power draw and complexity r over the standard cold gas versions. Vacco sells a warm gas 1U thruster that operates with 15 W for 5.4mN thrust, 595 total impulse and 70 seconds specific impulse. [Vacco]

Hall Effect Thrusters have been used on larger satellites, notably as the propulsion for SpaceX's Starlink constellation of "table-sized" satellites. While miniaturized concepts are popular, and companies like Busek, Vacco, and Orbion are in testing, none of these thrusters can operate at less than 175 W. The power, mass, and volume requirements continue to make them a difficult prospect for even the larger CubeSat formfactors. [Busek, Orbion, Vacco]

Pulsed plasma systems use a high voltage arc between two electrodes to ablate and ionize propellant, typically a solid. The discharge creates a magnetic field which further accelerates the ions. The industry standard fuel is a solid Teflon, but other propellants have been used. These pulsed systems have a lower efficiency but also operate at a much lower power than many of the other electric propulsion options. The precision impulse bit and pulsed nature of the system have made them ideal for attitude control work, and Busek's Micro Propulsion Attitude Control System has heritage from a 2007 flight on FalconSat-3 [Busek].

Ion engines use electric energy to ionize propellant which is then accelerated with electrostatic grids. At around 40W operating power, they require a high but achievable input for a large CubeSat. They have a very efficient use of propellant with Isp of 1000-6000 s. Current state of the art CubeSat thrusters include the Bit-3 Busek iodine thruster which is scheduled to fly on two of the Artemis 6U CubeSats, and the Enpulsion indium field effect thruster, which has flight heritage as well as the highest reported Isp. [Busek, Enpulsion].

Electrospray propulsion is similar to ion engines in the electrostatic acceleration of the ions, but differs in that the liquid fuel, and ionic liquid, can be wicked up into very small droplets, and requires no additional ionization. This method does not require pressurized fuel storage and has lower power requirements than the available ion engines. Accion Systems has developed the Tile 500 0.5U system which has a proposed operating power of 8 W, 1250 s Isp, and 20-60 Ns total impulse [Accion]. The system has not yet been tested in flight to achieve a TRL level of 9.

Solar sails are a popular concept with a very low thrust but the potential for a large total impulse over long periods of time, and no propellant mass. They use reflected photons from a large surface area to impart momentum to the spacecraft. Solar sails have been tested on LightSail 2 in a low-Earth orbit [LightSail]. NEA Scout, with 86 m^2 of sail stowed in less than a 2U volume, will test solar sail propulsion beyond LEO for a close flyby of a Near Earth Asteroid. [Orphee].

1.4.4 Summary of CubeSat propulsion systems

Many methods of CubeSat propulsion have been proposed, but few have reached TRL 8 and even fewer have flight heritage as CubeSat systems. There are strengths and drawbacks to the current manifestations of different propulsion methods. In general, systems capable of delivering higher thrust require the mass and volume for pressure vessels and valves, while the most fuel-efficient Hall thruster systems only operate at high power levels. Propellant-less solar sail systems provide very low thrust, which limits their possible mission uses. While electrospray and ion thrusters show promise with further qualification, this work will focus on the opportunity provided by pulsed plasma thrusters to use solid fuel at a variety of power levels to produce mid-range thrust levels.

1.4.5 Summary

CubeSats are a class of satellite defined by their dimensions and use of a rail system in a deployer. They span several mass categories from micro- to pico- satellites, and the term SmallSat is used here to describe a mass range that is useful in CubeSats currently capable of propulsive science missions. CubeSats are increasingly used across university, government, military, K-12, and industry sectors. This increase in CubeSats occurs in conjunction with an increase in supporting systems and subsystems for small satellites. Current targets of science missions using or proposing to use 3-6U CubeSats range from LEO, to the moon, to near Earth asteroids, and even Mars. Further increases in propulsion technologies are needed to increase the scope of science missions CubeSats might undertake.

Chapter 2. Science questions enabled by propulsion advances

This Chapter proposes two science missions that would be enabled by the technologies discussed in the following Chapters. The first is an asteroid mission initiated from a spacecraft traveling to Mars, and the second is a Europa mission in conjunction with a spacecraft travelling to Jupiter. The following descriptions detail potential CubeSat missions to address these questions, including the instrumentation and propulsion necessary to enable these missions. Similar to the Mascot lander on the Hayabusa mission, the addition of CubeSats to a larger mission increases the science capability that could not be enabled by added instrumentation on the main spacecraft. The concept of operations for these missions motivates the requirements for propulsion advancements.

2.1 Mars to asteroid belt

An increase in the number of space faring countries and companies, as well as a popular interest in manned spaceflight, has led to a planned increase in the frequency of planetary missions, including Mars and Jupiter. Given a starting trajectory past Mars, a CubeSat with advanced propulsion could reach the asteroid belt. The use of CubeSats for missions of this type allows for the possibility of reduced costs launching lighter payloads or additional satellites for extended science goals. The science gains, mission overview, and propulsion requirements of a possible CubeSat mission to land in two locations on a target asteroid of the Flora family in the asteroid belt are presented.

2.1.1 Motivation and background

The National Research Council Planetary Science Decadal Survey and the 2014 NASA Science Plan both note that the big unanswered questions for planetary sciences include the primordial sources of organic material [Decadal]. This is related to the question of what governed the accretion, supply of water, chemistry, and internal differentiation of the inner planets. These questions are difficult to resolve with remote sensing alone. In situ measurements and sampling are expected to play a major role in solving these questions.

The study of primitive bodies such as asteroids and comets provide an important aspect of addressing these questions since they potentially include original components from the early formation of the solar system [Decadal]. A pioneer in this effort was the JAXA *Hayabusa* mission to asteroid Itokawa. This mission demonstrated that small asteroids could be rubble piles [Abe], and with the analysis of return samples from its surface showed that despite the lack of an atmosphere surface dust particles had erosive smoothing [Tsuchiyama]. *OSIRIS-Rex,* launched in September of 2016, will rendezvous with near-Earth asteroid Bennu and will use compressed gases to blow a surface sample of dust into a special collector during a touch-and-go encounter with the surface [Tsuchiyama]. The sample is expected to be returned to Earth by 2023 [Beshore].

To attain a sub-surface sample, *Hayabusa 2* used a hyper-velocity projectile to create a crater for subsurface access on the C-type asteroid 1999 JU3, or Ryugu [Tsuda]. A touch-and-go approach was again used to collect exposed material. Because the target is C-type there is the prospect of attaining organic samples. The spacecraft was launched in 2014, rendezvoused with Ryugu starting in June of 2018, and performed two touchdowns for sample collection before departing the asteroid in late 2019 to return the collected samples to Earth.

The *Rosetta* mission to the comet 67P/Churyumov-Gerasimenko had the goal of studying the chemical and physical properties of comet's nucleus. This mission included a daughter craft *Philae* that was to have a soft (~ 1 m/s) landing on the surface, then attach to the surface and provide in-situ measurements of the comet [Glassmeier]. Unfortunately, *Philae* was unable to attach to the surface and in fact bounced several times [Biele].

2.1.2 Science Goals

The mission proposed here is to study the Flora family of asteroids that are thought to originate from a core of magmatically differentiated planetesimal [Gaffey]. The properties of this family are poorly understood. This makes the Flora family of asteroids, of which Flora is the largest member, important astronomical targets. The Flora family is theorized to be the source of LL chondrites. A sample return mission could confirm or refute this theory. If confirmed, the additional data would provide insight into impact shocking of the parent body; inform models for near Earth asteroid sources; and aid in the characterization of the effects of atmospheric entry on meteorites. The low eccentricity and inclination of the Flora family are also ideal to limit the required propulsion for the mission. The family falls within 2.1 to 2.5 AU with an eccentricity of 0.065 to 0.19, and a sine of the inclination that ranges from 0.025 to 0.13 [Dykhuis].

951 Gaspra is part of the Flora family and would be the primary target. It has a lower escape velocity than Flora, and detailed imagery from the Galileo flyby exists. Thus, there is already excellent data to determine the landing site and to develop the recognition software for the landing [Veverka]. The Galileo observations showed that, in addition to cratering, there are long linear groves a few hundred meters long by tens of meters deep which suggest that Gaspra is a single coherent body and not a rubble pile.

The imaging from Galileo also showed the presence of old craters that appear relatively smooth as well what appear to be younger craters with much shaper features. There are also slight albedo differences that may be due to variations in the regolith [Clark, B]. That Gaspra has a regolith at all is a source of mystery and debate. In larger bodies, such as the Moon, micrometeorites create regolith in a process called gardening. The impacts from micrometeorites generate fine grain ejecta that falls back to the surface as regolith. The low escape velocity from Gaspra suggests that this ejecta material produced during micrometeorite impacts should be lost to space rather than settle back on the surface. An asteroid hopper has the potential of investigating such distinct sites including unique subsurface sampling to provide fundamental insight into the origin and evolution of asteroids and the solar system.

The specific objectives of going to two different sample regions are to address issues associated with the formation and evolution of the solar system including:

(1) Do the two landing sites have the same composition despite different surface appearances, indicating that they have the same origin and/or no differentiation has occurred. Alternatively, is the composition varied, indicating the presence of complex processing during the formation and evolution of the asteroid(s). Spectral information would enable us to determine whether these asteroids have the same mineral structure/composition as Flora. The propulsion electronics could be used to turn some of the sample material into plasma and the associated spectral lines would be used to determine composition. The remainder of the sample would be retained for potential recovery by another spacecraft.

(2) Is the material around the impact craters associated with impacts from other members of the Flora family or have they been produced by impacts from different remnants of the early solar

system? An examination of the Galileo data would determine the most interesting crater for the landing. Analysis of the spectra from sampling at different depths along with close-up imaging would provide information on potential stratigraphy and the processes leading to the formation of the crater.

(3) How deep and how recent is the gardening of the surface by solar wind interactions or by micro-meteorite impacts? There are a variety of mechanisms that may be contributing to the processing of surface material and relative importance of these mechanisms may change with the age of the solar system. Processing of surface material as seen by the reddening and darkening of asteroid surfaces in present times appears to be not fully explained microphase iron from micrometeorite impacts [Clark, B]. However, the presence of dusty craters as seen by Galileo would indicate that surface gardening by micro-meteorites was at least important during some part of the asteroid's past. The return sample from Hayabusa-1 indicated that seismic activity may lead to the rounding of the dust [Beshore]. Landing in a crater enables the examination of the relative importance of these processes, and thereby provides insight into the evolution of the solar system.

(4) Map the global properties using visible and infrared wavelengths to gain an increased insight into chemistry, and mineralogy of the target asteroid and thereby provide a better understanding of the origin of all components of the asteroid and increased insight into the evolution of the solar system. An important aspect is looking at how the asteroids formed. S-type asteroids formed in inner part of belt, where the temperature was high enough to prevent condensation and accretion of volatile species, and only refractory materials condensed out. Volatiles, such as carbonaceous materials and water ice, were able to condense in the lower-temperature outer region, forming C-type asteroids. However, recent studies suggest that the lower-temperature carbonaceous material present in the main belt formed much further out (~4-5

AU) and was scattered into the asteroid belt during the first major migrations of Jupiter and Saturn [Walsh].

The proposed remote measurements along with the subsurface samples will provide critical information of composition to resolve these issues on the origin of the asteroids.

2.1.3 Mission concept and instrumentation

The mission concept is depicted in Figure 2-1 and is distinguished by a drop-off near Mars, refelectarray communications, pulsed plasma propulsion, and a spring compression landing system to allow for semi-hard landings and later take-off to return towards Mars. The CubeSat described is 24U, in a 2U x 4U x 3U form factor, weighing less than 30kg. After deployment, the solar panels and communication system un-fold and a plasma thruster is used in conjunction with a Martian flyby to achieve the maximum of 3 km/s ΔV required to reach the target asteroid. The surface area of the power system is designed to produce 30 W_e at 2.2 AU, the radial distance of the proposed target asteroid. The communications system is designed to reach orbiting spacecraft around Mars providing the link back to Earth.

Initial mapping of the target asteroid occurs on approach and braking is performed using the plasma thruster. Once the CubeSat has reduced its velocity relative to the asteroid to 5-15 m/s and in final approach the solar panels and communication array are folded back into the SmallSat for safe storage. The landing spikes are then deployed, and the CubeSat impacts the surface at 5-15 m/s with the spikes producing firm attachment to the asteroid.

After landing, the solar panels and communication array are re-deployed and drilling commences, along with close-up imagery of the asteroid surface. Once sufficient sample has been collected, the compressed springs on the spikes are released to eject the satellite at a speed of 2-3 m/s, which will exceed the escape velocity of the asteroid. Remote sensing of the asteroid continues during this phase. The spacecraft is then accelerated back towards the asteroid, again at a speed of 5-15 m/s. The sequence for impact and sample gathering is repeated at this second site using the second pair of landing spikes. When all sampling and in-situ measurements have been completed, the Smallsat is again ejected from the asteroid and the spacecraft uses the plasma thruster to arrive at the point of deployment, with the potential that it could be picked up and return to Earth by the pickup spacecraft.

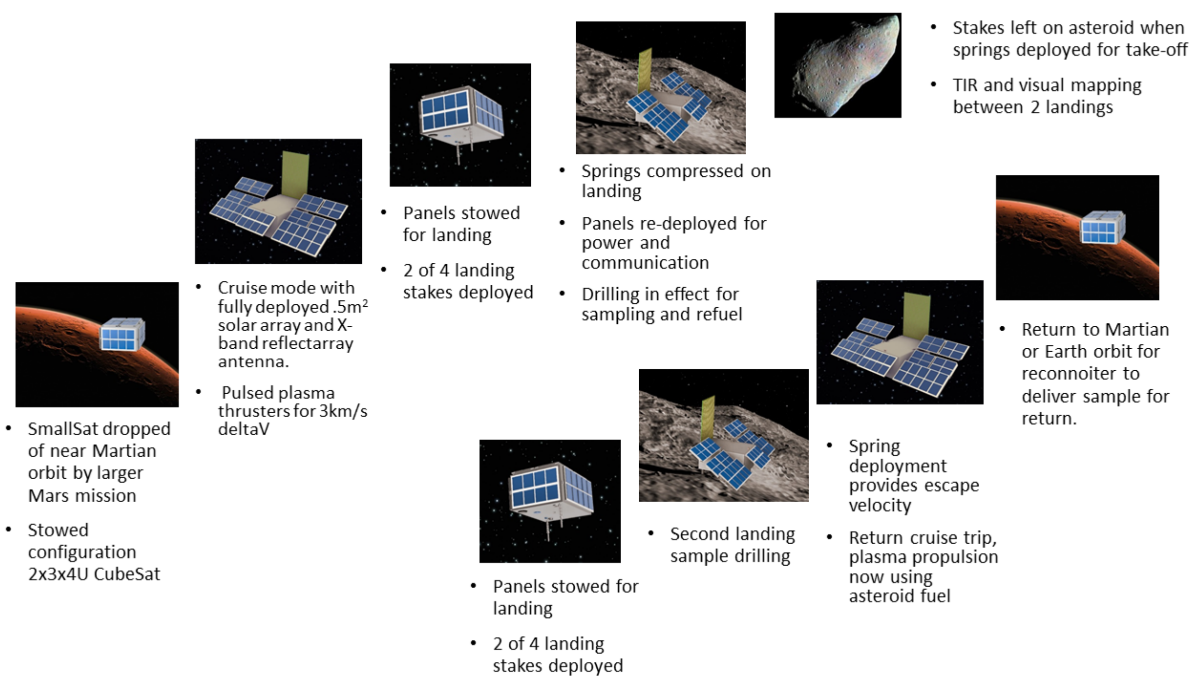

Figure 2-1 Mission concept for CubeSat to the asteroid belt

The instrument suite to enable the proposed science could easily fit in the planned dimensions as shown in Figure 2-2. The proposed components are either available or would need adjustment from instruments previously flown or tested. The instrument suite includes:

a. *Drill.* A drill system such as the Honeybee rotary-percussive corer (ROPEC) with a smaller, lighter weight version would be incorporated into the CubeSat. This system is specifically designed to take a core sample and have the sample extruded for initial sampling and final storage. The drill bit can be changed from an abrasive brushing tool to a powder acquisition tool, which is ideal for the proposed effort in attaining a subsurface sample.

b. *Pulsed Plasma Propulsion.* At relatively low inclination and eccentricity, as well as being located in the inner main belt, the Flora family is ideal as a main belt target group. Communication and power requirements become more difficult to achieve at greater distances from the Earth and Sun, respectively. The low inclination and eccentricity reduce propulsion requirements. Going specifically to Gaspra does limit the possible mission windows a maximum ΔV requirement of 3 km/s, a dual pulsed plasma propulsion system with several Kg of fuel could provide the needed thrust over time. Pulsed plasma systems are also able to use in-situ fuel, and could operate using material from the asteroid as a refuel [Johnson].

c. *Stereo Imaging System (SIS)* – The SIS would be used for guidance, navigation and control with a spatial resolution of 10 m at 1 km range. On approach, SIS would be used to accurately determine the asteroid's size, shape, and dynamic characteristics (period, orbital pole, and spin rate). An important aspect of the firm landing system is that the spacecraft velocity at impact. The impact velocity will be sufficiently higher than the rotation rate of the asteroid. Therefore, the trajectory need only match the rotation rate for the desired target area, and the spacecraft itself does not have to be slowed to match the rotation rate. For soft landing systems, matching the rotation rate is a significant and time-consuming effort. The approach imagery would be used to measure and characterize surface properties, including topography. After landing the stereo images not only provide views from the surface, they will be used to determine the actual proximity of the surroundings – an aspect that would be deceitful in 2D images, where depth perception relies on the perceived proximity of the horizon. After re-launch, SIS would be used to observe the landing site and the extent of the landing's effect across the asteroid's surface by comparison with before-landing images.

d. *VIS-IR spectrometer* - which will be a point spectrometer. Although it collects data from a single spot on the surface, multispectral images can be generated by combining measurements of the continuous path of the spacecraft as it orbits the asteroid. VIS-IR will cover the visible wavelength range to mid-infrared (~0.4 to ~5 micrometers) with sufficient spectral precision to identify compounds including silicates, oxides, carbonates, sulfates, water and organics. In addition to determining the surface properties, VIS-IR will be used to examine the light from the collected sample when it is injected into the PPT for analysis. Since the PPT does not use a propellant with a carbon basis, the spectrometer will be able to identify subsurface organics if present. Using the same instrument for orbital and in situ spectral measurements reduces the volume requires and enables a robust analysis in real time.

e. *Thermal Imager (TI).* In orbit, TI will measure the thermal properties of the asteroid, which will be used to determine surface properties of the asteroid, such as whether and where the surface has exposed solid rock versus granular or dusty regolith. TI can also characterize the structure and cohesion of the regolith. TI measurements can be used to characterize other surface properties that contribute to thermal effects, like changes in rotation resulting from the Yarkovsky/YORP Effect. After re-launch, measurements of the landing site will be compared to pre-landing. Residual thermal emission above pre-landing values (after

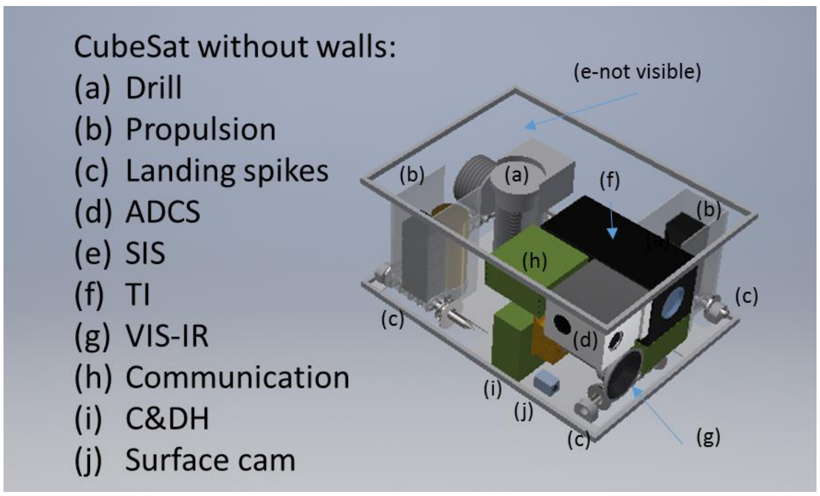

Figure 2-2 Internal view of instrumentation layout for asteroid science mission

removal of any solar irradiation, if applicable), at the landing site and elsewhere around the asteroid, will provide valuable information about the asteroid's deeper properties.

2.2 EUROPA CUBESAT ASSIST

Another application of the CubeSat technology developed here is a close Europa mapper. Mapping the magnetic fields around Jupiter's moon Europa, is the science goal of the of a proposed Europa CubeSat. An analysis of the science motivation, mission concept, and propulsion requirements follow.

2.2.1 Science and Motivation

The possibility of a liquid ocean on Europa was suggested by thermal models as early as 1971 [Lewis]. This was corroborated by evidence of tidal flexing [Cassen] and visuals of the ice cracks present on the surface [Gaidos]. Most recently, magnetic field data from Galileo displayed perturbations in the Jovian magnetic field near the non-magnetized Europa that are best described by a layer of conducting material within the moon [Kivelson]. The leading theory is that this layer is composed of high salinity water between the ice crust and rocky mantle. A large-scale water layer presents the possibility of hydrothermal vents similar to those found to support ecosystems of extremophiles here on Earth.

The Europa Clipper Mission seeks further evidence and details of this ocean and the possibility of life with instruments such as ice penetrating radar and optical and infrared cameras. However, fly-by magnetic field measurements on the main spacecraft, which require long booms or deployable masts in order to be isolated from these instruments, are currently low priority. The ICEMAG, for Interior Characterization of Europa using Magnetometry, instrument was cancelled due to cost overruns and replaced with a lower cost option [Foust]. Thus, taking these measurements from a separate satellite orbiting Europa would serve the double purpose of isolating the magnetometers from interfering signals and providing the opportunity to take important measurements over a range of altitudes not previously accessed by spacecraft.

The addition of magnetometers serves to characterize the magnetic field environment around the moon and to help map variations in the possible subsurface ocean. Europa Clipper's closest approach is planned to be ~25 km from the surface of the moon. Galileo's closest approach to Europa was 196 km [Kivelson]. When mapping magnetic fields via satellite, the smallest scale size of the features that can be observed is a function of the altitude of the satellite. An ideal mission would be for the CubeSat to have a spiral orbit towards the moon's surface, to an altitude on the order of a kilometer, and then spiral back out, through a sequence of thruster maneuvers. This would achieve the goal of producing a complete mapping of the magnetic field. It would also allow for the identification of any small-scale magnetic structures, possibly associated with localized subsurface heat or mineral sources. An on-board stereo imaging system would allow for detailed surface mapping but would also increase the transmission demands.

Development of the system could provide a low-cost method for magnetometers to be included on a variety of space missions, not just the Europa Clipper mission. The recent Dawn mission to Vesta and Ceres has already provided a wealth of information about the surface structure of Vesta, but the lack of a magnetometer (due to descoping of the instrument) has left many questions unanswered. One such question is regarding the possible role of an intrinsic magnetic field in producing the observed reduced space weathering of Vesta's surface [Pieters]. A method of using coupled spacecraft (a main discovery class spacecraft and a ride-along CubeSat with magnetometers) could provide a cost-effective option for obtaining a full suite of information about an object.

2.2.2 Mission concept and propulsion considerations

In order to maximize the science return from a CubeSat mission focusing on magnetometer measurements near Europa, the goals of the mission would be to make magnetic field measurements with fine enough spatial and temporal resolution to potentially map structure in the subsurface ocean. The important time scale for sensing changes in the induced magnetic field created by the conducting ocean is the time scale for changes in the background Jovian magnetic field. With a Jovian rotation rate of around 10 hours and the 85-hour orbital period of Europa, the ΔB observed by a satellite in orbit around Europa is on a much smaller time scale than the ~ 14-day period between each Clipper flyby of Europa

The issue of time and/or spatial scale measurements could be resolved by having the CubeSat provide supplemental data to the main spacecraft. Two possible scenarios include:

1. The CubeSat is in a trailing orbit, following the Clipper as it orbits Jupiter
2. The CubeSat in orbit around Europa, communicating with the Clipper only during flybys.

2.2.2.1 Trailing Orbit

Figure 2-3 shows a case for the CubeSat being released 2.5 days prior to flyby Europa17E1, with a 1 m/s ejection velocity. The CubeSat in this case lies between Europa and the Clipper and has a closest approach altitude of 455 km, while the Clipper closest approach is 753 km. This difference in altitudes between the CubeSat and the Clipper would enable 2-D mapping of features between the satellites and Europa. Due to the difference in altitudes between the two spacecraft, a relative ΔV of about 0.1 km/s results.

There are then two scenarios for the CubeSat at this point. If there is no propulsion on the

CubeSat, then once measurement data is transmitted to the Clipper, the mission is essentially over. The alternative is to carry some form of electric propulsion onboard that could make up the difference in speed over the next 14 days prior to the next encounter. High I_{SP} electric propulsion units could be used if multiple such encounters would be anticipated. If one assumes a 2kg CubeSat with 1kg of instrumentation and 1kg for propulsion and power, a total acceleration of 0.3 mN would be required for the CubeSat to catch up with the Clipper in a 14-day period. Using an electric propulsion unit with 25 mN/kW, this could be achieved with about 16 W of power. Thus, a trailing CubeSat could be a viable mission that yields multiple dual measurements during Europa Encounters.

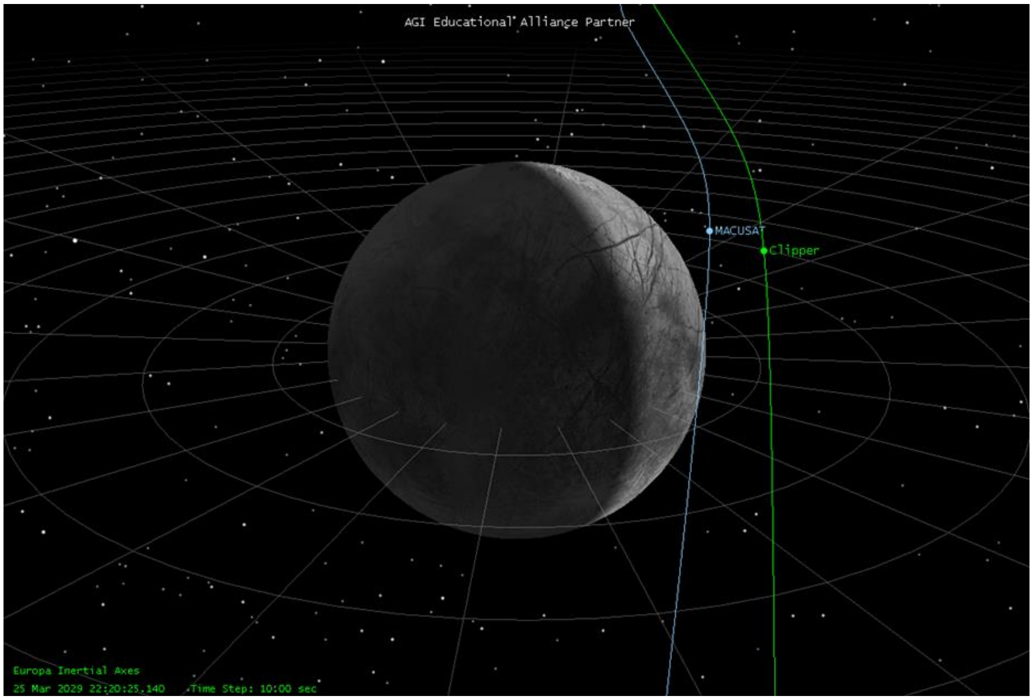

Figure 2-3. Example trajectory of the Europa CubeSat and Europa Clipper passing Europa with variation in closest approach allowing for measurements at different distances only shortly separated by time.

Further motivating the use of propulsion in the trailing orbit scenario is the communication requirements to link CubeSat data to the Clipper. A propulsion system that kept the CubeSat within a few hundred kilometers of the Clipper is needed to enable the data transmission.

The known communication information from the Clipper is: UHF band, and a 6dBi gain antenna. The worst-case scenario for the CubeSat antenna is a gain of 0dBi. A link budget can be estimated for a 2.4 GHz frequency signal with 6 dBi gain on the antennas and with losses for lines and implementation, a BPSK modulation, and the parameters from Table 2-1.

Table 2-1 Numbers for link budget calculation

Item	**Symbol**	**Units**	**Value**
Frequency	f	GHz	2.4
Transmitter Power	P_T	dBW	10log(P)
Transmitter Line Loss	L_I	dB	-1
Transmit Antenna Gain	G_t	dBi	6
Path Propagation Distance	D	m	D
Space Loss	L_s	dB	-40-20log(D)
Receive Antenna Gain	G_r	dBi	6
System Noise Temperature	T_s	K	150
Data Rate	R	bps	R
Energy/bit to noise-density ratio	E_b/N_0	dB	$178+10\log(P_T/(D^2R))$
Bit Error Rate	BER		10^{-7}
Required E_b/N_0	Req E_b/N_0	dB	11.3
Implementation Loss		dB	-2
Margin	M	dB	8

Assuming a link budget margin of 8 dB, the following relationship, with units as provided above, is extracted using methods described in [Wertz]:

$$\sim 2 * 10^{-16} = \frac{Power_{transmit}}{Distance^2 DataRate} \qquad Eqn\ 11$$

This relationship can define the energy per bit required for a given distance between the Clipper and the CubeSat. Figure 2-4 is a graphical representation.

Running solely on non-rechargeable batteries is feasible for the trailing orbit scenario where the CubeSat is released shortly before closest approach with Europa. The capability of communicating back to the Clipper can be analyzed by using equation Eqn 11. Figure 2-4 shows this calculation assuming a 0.5 kg battery of energy density 200 Whr/kg with a 10% efficiency from battery to RF power. This sets the upper bound on the total amount of data which can be transmitted for a given distance from the Clipper.

Running solely on batteries is a possibility but only for short duration missions. This would be the cheapest system for single flyby scenario (Case A). For extended missions, other sources of power would need to be investigated.

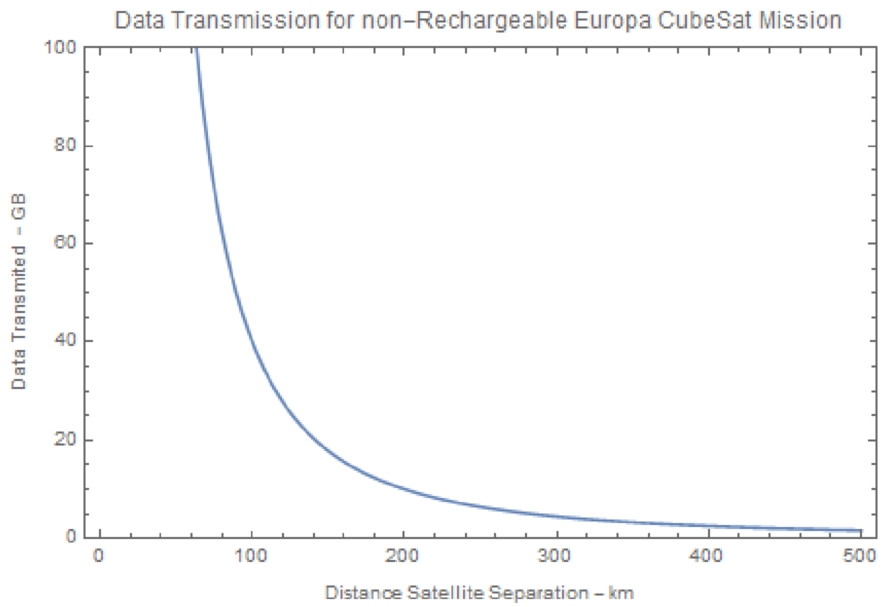

Figure 2-4 Possible total data transmitted in Gigabits from the Europa CubeSat to the Europa Clipper based off a maximum separation between the satellites and given a limited battery life.

2.2.2.2 Orbital insertion around Europa

Figure 2-5 shows a polar orbit around Europa. Other orbital insertion scenarios were also found, including equatorial orbits, but this figure represents the orbital insertion with the lowest ΔV required of those analyzed. This orbit requires 3.26 km/s ΔV for orbit insertion. In the example, the CubeSat is dropped off by the Clipper with a ΔV of 0.150 km/s. For this case, it is dropped off only 3 days before Clipper closest approach for that pass. To avoid the large ΔV requirement, it is possible to use a pre-injection flyby trajectory, until achieving a 6:5 resonant orbit with Europa.

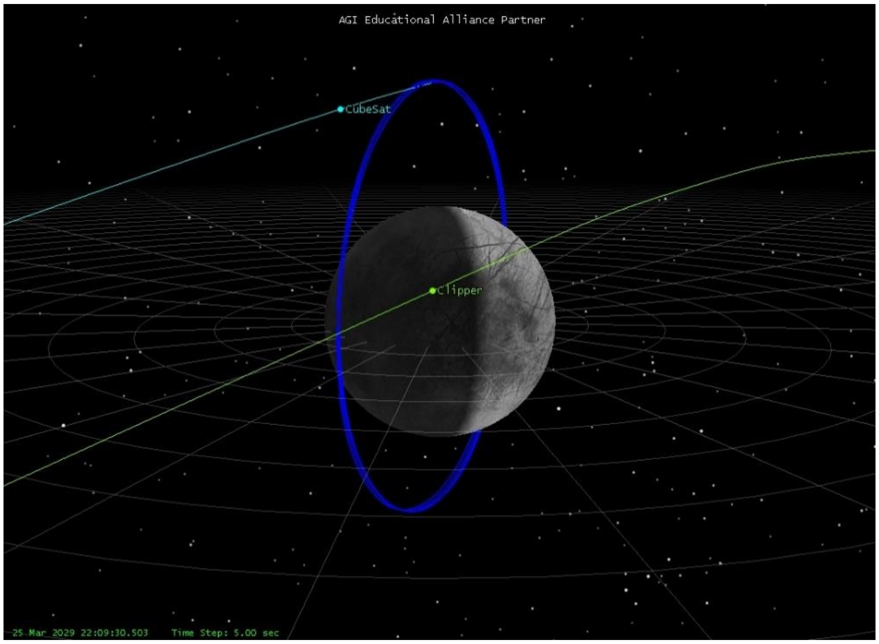

Figure 2-5 CubeSat Polar Orbit around Europa.

At this point, Δv for orbit insertion is less than 0.8 km/s [Johannesen].

It would be cost prohibitive for the entire Clipper to perform this maneuver. Instead, having only a small satellite perform this maneuver could be managed, as the total impulse required is much lower. For example, if solid rocket motors were utilized to perform this maneuver then the mass fraction from the rocket equation, assuming an I_{SP} of 200s for a solid propellant motor, would be about 20%. Thus, a 10 kg system for a 2kg CubeSat could place the CubeSat in orbit around Europa and not have a significant impact on the total mission costs.

If a slightly larger mass of between 15-20 kg was allocated, an onboard electric propulsion could be added to the CubeSat. This onboard propulsion would enable the spacecraft to alter the altitude of its orbit and enable full mapping of Europa, with data being transmitted to the Clipper during each encounter.

The scientific return from such a mission for the additional doubling of mass from the trailing orbit scenario makes orbital insertion the more interesting mission scenario, but only if the additional mass could be afforded. To minimize data transferred, some type of onboard data selection would have to occur with burst mode communications occurring either prior to or shortly after closest approach of the Clipper.

2.3 SUMMARY

The three CubeSat missions proposed could all be enabled or enhanced using CubeSat propulsion systems. The ability to refuel using in situ material at an asteroid makes even a 1-3km/s ΔV CubeSat mission to the main asteroid belt possible. Main asteroid belt missions are needed to further understand the formation of the solar system and constrain models using ground-based observations. Electric propulsion could enable the ~0.3mN thrust for a 2 kg CubeSat to maintain following distance from the Clipper as it conducts multiply flybys of Europa. An orbital insertion of a CubeSat around Europa would require ~ 3km/s ΔV from a direct Clipper orbit, but lower ΔV is possible using additional flybys and other Jovian moons. CubeSat propulsion could enable this lower ΔV insertion, or, given a larger CubeSat mass budget, also more closely map the magnetic field fluctuations and surface topology at different altitudes.

Chapter 3. Pulsed Plasma Thruster Increased Specific Thrust

This chapter discusses the choice of pulsed plasma thrusters (PPTs) as the target of improved CubeSat propulsion through increases in specific thrust. It includes background on the typical design and operation of PPTs with laboratory and flight heritage. It then details how increases in specific thrust were obtained, where it closely follows and expands upon the published work:

"Pulsed Plasma Thruster Gains in Specific Thrust for CubeSat Propulsion" [Northway]. Estimates for are then developed for the potential operation on a CubeSat and for possible science missions.

3.1 Introduction to Pulsed Plasma Thrusters

3.1.1 Pulsed Plasma Thruster background

3.1.1.1 Operation

The pulsed plasma thruster is characterized by a solid fuel between two electrodes, the anode and the cathode. A general schematic of a PPT is shown in Figure 3-1. The configuration of the electrodes and the fuel is typically either a coaxial configuration, as is true for this work, or a parallel or diverging plate configuration. The plate configuration was used in the PPT built by Aerojet Rocketdyne for the Earth Observer-1 mission and the SIMP-LEX PPT from the ISR at the University of Stuttgart, along with several others [Dykhuis and Nawaz]. The fuel can then be either "breach-fed," where it is fed in through the rear of the electrodes and the surface is perpendicular to the discharge, or "side-fed," where the fuel surface has a parallel component to the discharge. The geometry of the electrodes and/or envelope allocated for a propulsion system are driving factors in the actual fuel feed system design. A complex feed system requires moving parts, which would negate one of the advantages of this propulsion type. Instead, springs are used to feed the fuel for simplicity and robustness. Springs can be considered moving parts, but do not require actuation.

The discharge of energy stored between the anode and cathode across the surface of the solid fuel constitutes a pulse. The discharge super-heats the very top layer of the fuel, ablating and ionizing tens of micrograms of the propellant. That energy is stored on the main discharge capacitors. The magnitude of the energy, E, is given by $E = \frac{1}{2}CV^2$, where C is the capacitance on the main capacitor bank, and V is the voltage that capacitance is charged up to. Values of C and V range from 0.6 to 100 μF and 400 to 3000 V, giving E from 1.8 to 750 J. Varying both the capacitance and the voltage can change the output of the thruster, but energy is used as a characteristic to base comparisons on in the literature [Burton].

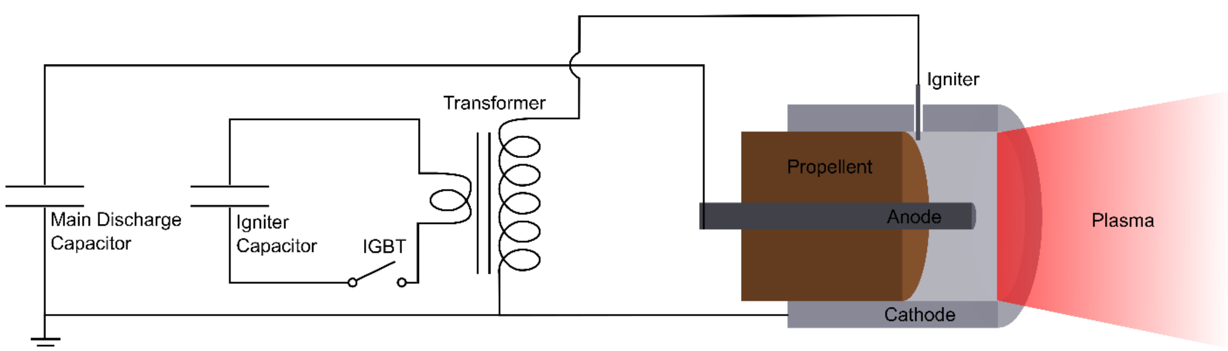

Figure 3-1 Example schematic of electrical and physical PPT layout

The discharge of the stored energy is initiated by an igniter. The electric field from the stored energy is insufficient in vacuum conditions to allow breakdown without the presence of seed electrons, so the igniter is needed to provide the seed electrons. Once the seed electrons are in the system and accelerated by the main electric field, the discharge is initiated. Igniters typically operate similar to sparkplugs in cars, which use a high potential difference over a short distance to create an electric field strong enough to ionize the air in the gap. In space propulsion systems, there is no air to ionize, so the electric field must be high enough to strip electrons from the metal, overcoming the work function of that metal.

3.1.1.2 Pulsed Plasma Thruster heritage and prior art

The simple, nontoxic, and robust nature of pulsed plasma thrusters have made them a popular choice for both study and flight operations. The flight heritage of PPTs goes back to the 1960 Russian Zond mission, where PPTs were used to assist in the attitude control [Kim]. More recently, the Earth Observer -1 (EO-1) mission utilized a PPT for precision attitude adjustments. The EO-1 PPT was built by Aerojet Rocketdyne and operated for over ten years [Zakrzwski]. Very recently, the Busek Micro Propulsion Attitude Control System successfully operated on FalconSat-3 [Busek]. FalconSat-3 is a 50kg microsatellite that was launched in 2007.

Pulsed plasma thrusters are also being designed for CubeSat form factors. A new and potentially noteworthy thruster is under development by CU Aerospace. The thruster includes a novel capacitor bank and a Teflon filament fuel feed, analogous to filament in 3D printer [CU Aerospace]. The filament is fed through the center of the coaxial anode, with the cathode at a larger diameter. Reportedly, a 1U design can provide 4900 N-s total impulse. Clyde Space, now AAC Clyde Space, briefly advertised at 0.33 U PPT system for CubeSat station keeping capable of 48 N-s total impulse [Ciaralli].

Examples of major academic studies on pulsed plasma thrusters include University of Stuttgart with the ADD-Simplex thruster, University of Washington with the Dawgstar thruster, and MIT Lincoln Laboratory with the Lincoln Experimental Satellite (LES) program. Other groups involved in PPT development and research include the University of Michigan, Ohio State University, University of Illinois Urbana-Champaign, and Beijing Institute of Technology.

While a wide variety of electrode and fuel geometries have been tested, solid fuels have been limited to plastics. Teflon is the heritage fuel of all the PPTs flown previously and most PPTs in development. Other commercial plastics, including Delrin, Kynar, and Viton have been tested, all with resulting surface charring or I_{sp} values similar to or lower than Teflon [Guman]. Polyethylene (C_2H_4) had the highest specific impulse, which is attributed to the low ion mass of exhaust products. However, Polyethylene has been found to char significantly, where carbon ions return to the propellant surface and begin to create a conductive layer across the surface. In extreme cases, this can short the electrodes, but in general it simply decreases the ablation rate. Teflon fuel sometimes has charring when firing at low energy densities, but high voltage pulses have been shown to “clean” the surface, reducing the charring buildup [Nawaz and Keidar].

Liquid and gas fueled pulsed plasma thrusters have also been investigated [Rezaeiha and Zeimer]. A recent study even proposed the replacement of solid fuel with a thin layer of HAN-based green electric monopropellant applied between pulses [Thrasher]. The use of liquid and gas in PPTs increases the flexibility of the system but also adds the complexity to the system in the form of valves and pressure vessels.

3.1.2 Motivations

Motivations for improving propulsion options for CubeSat are presented in Chapter 1. This section motivates the choice of PPT as a type of CubeSat propulsion and the focus on increasing the PPTs specific thrust.

3.1.2.1 Pulsed plasma thruster as CubeSat Propulsion

There are many advantages to a PPT system. The utilization of solid fuel is one of the main advantages, as it eliminates the need for fuel tanks, feed lines, and valves that need to be tested for leaks and operation over a broad range of temperature in a vacuum setting. PPTs are inert and cannot provide thrust without being powered, making them fail-safe. There is no need for standby power, and the PPT system can go from zero power-draw to producing thrust in just the amount of time it takes to charge the main capacitors. Other systems, including Hall thrusters, require a warm-up time before any operation or before operating at full thrust. In fact, PPTs have demonstrated operation across a wide range of external temperatures [Azuara]. Being nontoxic in general and having a long shelf life are other benefits to working with and flying pulsed plasma thrusters on satellites.

The principal deciding factor for choosing the pulsed plasma thruster for this work is the solid fuel utilization. Where CubeSats are generally launched as secondary payloads, active propulsion systems have historically not been permitted, and propulsion systems with pressure vessels and valves are not even considered. It is noteworthy that this general ban on propulsion systems is no longer firmly in place due to increasing testing and certification by professional facilities, but it continues to be a consideration for many deployments.

3.1.2.2 Focus on specific thrust

CubeSats are very constrained on several fronts. The obvious constraints are on power, mass, envelope, and total volume. Power is limited based on solar panel surface area, and CubeSats are typically not designed to operate for long duration. The lifetime constraint is driven by either deorbit time from a low altitude orbit, or cost constraints limiting radiation hardened hardware.

Radiation shielding is generally difficult given the mass and volume constraints. This requires an effective CubeSat main propulsion system to operate using limited power in a limited timeframe. The historical optimization of electric propulsion systems for fuel efficiency (I_{sp}) using high-power systems operating over extended time periods is less useful in this regime. Instead, specific thrust, or thrust out per power input, addresses the constraints on power and lifetime. It allows the low powered satellite to change its velocity over a shorter time frame, which is exactly what is needed for missions like the Europa Clipper CubeSat. Specific thrust is the target parameter in the following studies.

3.2 OBJECTIVES

Specific thrust is optimized in this study for practical applications on CubeSats, which often have limited power and limited lifespans. The specific thrust, T_{sp}, is determined using the measured impulse bit and the main discharge energy:

$$T_{sp} = \frac{I_{bit}}{E} \quad \text{in} \quad \left[\frac{\mu\text{N} * \text{s}}{\text{J}}\right] \qquad \textit{Eqn 12}$$

which is unit equivalent to milliNewtons per kilowatt giving thrust output over power input. With a goal of optimizing specific thrust, two key areas for optimization were investigated. The first is propellant type, where alternatives to the standard Teflon are tested and shown to yield different specific thrust. Second, the geometry was changed to allow for a large surface area with sufficiently large electric fields to break down in vacuum, and which altered the total thrust

3.2.1 Propellants

Nine propellants were tested in a 1-inch diameter smooth cylindrical PPT configuration. The choice of propellants included a range of metals, minerals, and plastics. The choices followed the constraint that the propellant had to remain as a solid under room temperature vacuum conditions. Propellants also needed to be nontoxic for safe testing purposes within the facility. The minerals have potential in-situ fuel utilization implications, while the metals have high molecular mass in the plasma exhaust.

The high molecular mass of exhaust particles is in direct opposition to the previous interest in polyethylene for its low mass of exhaust products. Low mass exhaust products enabled higher I_{sp}, or higher exhaust velocity. The kinetic energy and impulse of a particle in the exhaust plume is given by

$$\mathrm{KE} = \frac{1}{2}\mathrm{m} * v^2 \qquad \textit{Eqn 13}$$

and

$$I = mv \qquad \textit{Eqn 14}$$

For two particles with masses m and $(m + \delta)$ with equal kinetic energy, impulse from the second particle will be a factor of $\sqrt{1 + \frac{\delta}{\mathrm{m}}}$ larger. If the same portion of electrical energy stored on the main capacitors were transferred into kinetic energy in the exhaust, propellant composed of larger ions would have a higher impulse, leading to a higher specific thrust.

Thus, non-conducting materials such as sulfur with an atomic number of 16 have the potential to yield more thrust than Teflon $(C_2F_4)_n$ with atomic numbers of 6 and 9. For conducting propellants, lead, with an atomic mass number of 82, has the potential of yielding a higher impulse than gallium, with an atomic number of 31. However, conductive propellants require a modification in thruster configuration to avoid shorting the electrodes: a 1-2 mm gap was left between the propellant and the electrodes. The backing material to the gap was Teflon. For propellants that were not readily shaped, as in the case of bismuth, olivine, chalcopyrite, and bismuth-sulfide, a minimal amount of epoxy was mixed in with the granulated propellant to attain the desired shape. Epoxy was then tested independently.

Propellant types tested are listed in

Table 3-1. In addition to chemical formula, the atomic mass and first ionization energies are listed. Ionization energy and energy of sublimation have been found to play a role in the specific thrust output of a given propellent. Energy required for sublimation is not easily determined for the non-elemental fuels, so melting point is listed.

Table 3-1. List of propellants with chemical formulas and characteristics [Bentor]

Propellant	Formula	Atomic masses (amu)	1st Ionization energy (eV)	Melting point (K)
Teflon	C_2F_4	F - 18.99 C - 12.01	F - 17.4 C - 11.2	600
Epoxy	CH_2-CH-O	H - 1.01 C - 12.01 O - 15.99	H - 1.01 C - 11.2 O - 13.6	
Sulfur	S_8	S - 32.06	S - 10.4	392
Olivine (Forsterite)	Mg_2SiO_4	Mg - 24.3 Si - 28.09 O - 15.99	Mg – 7.6 Si - 8.2 O - 13.6	1900
Chalcopyrite	$CuFeS_2$	S - 32.06 Fe - 55.85 Cu - 63.55	S - 10.4 Fe - 7.9 Cu - 7.7	895
Bismuth Sulfide	Bi_2S_3	S - 32.06 Bi - 209.98	S - 10.4 Bi - 7.3	1123
Lead	Pb_2	Pb - 207.2	Pb - 7.4	600
Gallium	Ga_2	Ga - 69.7	Ga - 6.0	303
Bismuth	Bi_2	Bi - 209.98	Bi - 7.3	545

3.2.2 Electrode Geometry

Previous work has shown that a larger propellant surface area increases the ablated mass [Johnson]. In a coaxial geometry with a set center electrode diameter, larger propellant surface area corresponds to a larger separation distance between the electrodes. Without an increase in voltage, this decreases the electric field at the surface cathode and increases the chance that the main discharge will not be triggered by the ignitor breakdown. If the seed electrons from the ignitor and secondary electrons at the surface of the cathode are not accelerated by the main electric field, the ignitor will spark without initiating the arc breakdown.

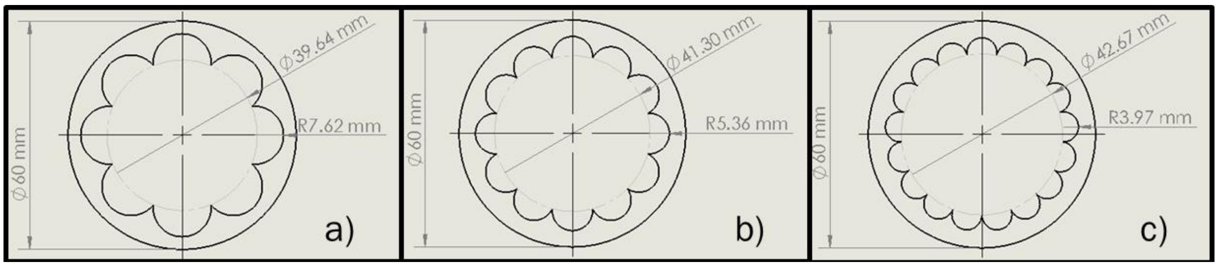

Figure 3-2. Demensions of the tested "daisy" or serrated cathode configurations with a) 8 points, b) 12 points, and c)17 points all with equal exposed surface area

To address the problem of low electric field at the cathode, a serrated, or “daisy,” configuration for the outer aluminum electrode is introduced in 8, 12, and 17-point configurations. The exposed propellant surface area is held constant, while the radius of the interior curves aligns with common drill sizes, to aid in the machining of the cathodes. The dimensions of each is detailed in Figure 3-2. At constant propellant surface area, a smaller number of points results in higher electric fields at the points but a smaller area between the tip of the points and the center electrode. The points create areas of high static electric field which allows for consistent discharge of the main circuit.

3.3 METHODS

3.3.1 Testing setup

All experimental work is conducted in a bell-jar vacuum chamber of 100cm height and 44cm diameter. Testing pressures are maintained between 5.5E-5 and 9.0E-6 Torr. Setup for the propellant testing is further described in Johnson, 2015.

3.3.2 Thrust stand

Thrust stand testing is conducted using a simple pendulum thrust stand. Small angle approximations are assumed for thrust calculation, and hold true in testing, with deflection angles below 5 degrees. Pendulums of different masses and pivot lengths were used throughout testing to ensure accurate measurement of thrust levels. Using a pendulum thrust stand approximated as a point mass at the end of a stiff string, I_{bit} can be calculated as

$$I_{bit} = \frac{\sqrt{2gm_pL_{cm}I_p(1 - \cos(\theta))}}{L_T} \qquad \textit{Eqn 15}$$

Where the pendulum physical characteristics m_p, L_{cm}, I_p, and L_T are the mass, length from center of mass to pivot point, moment of inertia, and length from the center of thrust to pivot point, respectively. g is acceleration due to gravity. θ is the maximum angle of deflection. For a given pendulum setup, it is useful to define a constant $\alpha_p = \frac{\sqrt{m_pL_{cm}I_p}}{L_T}$. This simplifies the I_{bit} to

$$I_{bit} = \alpha_p * \sqrt{2g(1 - \cos(\theta))} \qquad \textit{Eqn 16}$$

For testing, the PPT is secured to the stand and fired at the thrust plate, which is a thin non-conducting material covered in Kapton tape. In all cases the plate diameter is at least 1 cm larger than the thruster diameter, and the thruster is adjusted to be 1 cm from the plate.

In the propellant testing, video was taken through the glass of the bell jar and post-processed to determine the frame of greatest deflection. This single frame was then used to determine maximum deflection angle in the impulse bit equation. A Hough transform in the MatLab Image Processing Toolbox detects the line of the pendulum against a contrasting background and compares the frame before firing to the frame with greatest deflection to determine the change in the angle of the pendulum, θ.

Testing for the geometry study utilizes a more sophisticated method which tracks the full swing of the pendulum fitted to an underdamped pendulum motion (Haag, 1997). This method is enabled by a 180 frame per second slow-motion camera with 8 Megapixel resolution. It allows for a more precise determination of peak deflection angle and made it possible to account for damping on the initial peak. The angle of the pendulum calculation is the same, but it is calculated for the full video, and that data is fit using the MATLAB Curve-fitting tool, the fit is checked visually, and the calculated angular frequency is checked to be within the 95% confidence interval of the average angular frequency for that pendulum.

A comparison of the former “Frame” method against the new “Fit” method on the same 19 videos is shown in Figure 3-3. The average difference between the measurements is 15% of the frame method value, where the frame method is almost exclusively a lower number. This difference is attributed to the inclusion of a damping coefficient in the Fit method, which adjusts the angle of maximum deflection to account for damping on the outward swing. Damping is an expected term, as a thin aluminum plate is placed above the pivot point between two magnets to induce magnetic damping. The induced damping allows the pendulum to return to rest within ~10 seconds and minimizes any swing caused by external vibrations.

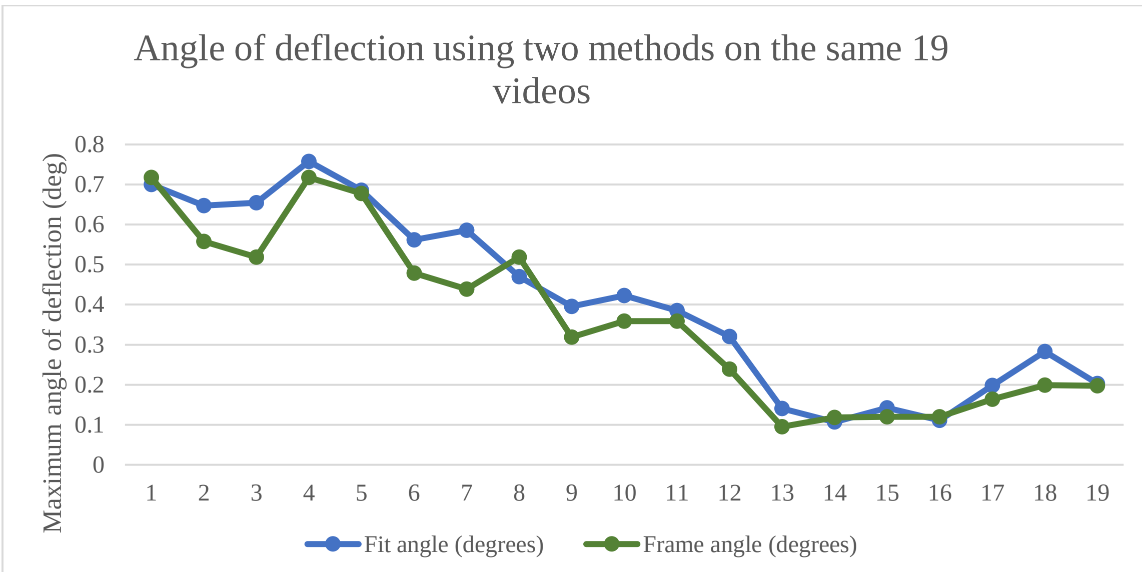

Figure 3-3 Comparison of angle calculated angle of deflection of the pendulum using two methods

The video method has several drawbacks, including blur and distortion caused by the bell jar in causing poor line detection. Camera misalignment can also alter the apparent slope of the line. The pendulum in these tests is composed of two thin rods separated by a centimeter running between the pivot point and the thrust plate. If there is misalignment in the system, the lines that are found by the Hough transform may be a combination of the two rods. In Chapter 4, a method using a magnetic inductive displacement sensor instead of the camera alleviates these drawbacks.

3.3.3 Time of Flight

Double Langmuir probes are used to collect data on bulk plasma velocity. Because the probes in the plume affect the plume, measurements are taken at 32 cm from the exit of the PPT and then separately at 27 cm from the exit of the PPT, giving a separation of 5 cm. Traces from the oscilloscope are saved and analyzed for the time of peak current output from the Langmuir probes. The current is measured through a Stangenes probe as described in Johnson, 2015. The thruster breakdown time, or start time, is also determined per trace. It is based off the main discharge voltage at the halfway point of the discharge. Due to slight variation in the timing of the discharge, external triggers are less accurate as a gauge of start time. The difference in average peak arrival time at 27 cm and 32 cm, divided by the separation distance, gives the bulk plasma velocity.

3.3.4 Mass ablation

Ablation rates for Teflon pulsed plasma thrusters have been previously reported, but no ablation rates for sulfur are available. To acquire the ablation rate for sulfur. A pulsed plasma thruster and a sulfur puck with similar surface area were simultaneously placed in the vacuum chamber. Prior to being in the chamber, they were both weighed using a Mettler AC 100 scale with g*10^{-4} mass precision. The PPT was fired several thousand times, after which both were immediately weighed upon returning to atmospheric pressure. The second sulfur mass allowed for control for vacuum pressure sulfur ablation. Each mass measurement was taken 3 times, closing the container and zeroing the scale between measurements, and the average of the three measurements was used in the calculation of mass bit in Table 3-5.

3.4 Results

3.4.1 Propellant Testing

While each propellant provided viable thrust over the short-term testing period, pure sulfur and the other sulfur containing propellant, bismuth sulfide, performed considerably better over a wide range of discharge energies. Individual particle mass was not found to be an important factor in overall specific thrust output, though the heavier sulfur had lower bulk velocities than Teflon in time-of-flight testing.

A low enthalpy of sublimation and low and ionization energy drove increased specific thrust as important factors. Low energy requirements to go from solid to gas allow for a larger amount of mass to ablated per pulse. With low ionization energy, a larger fraction of the ablated mass is

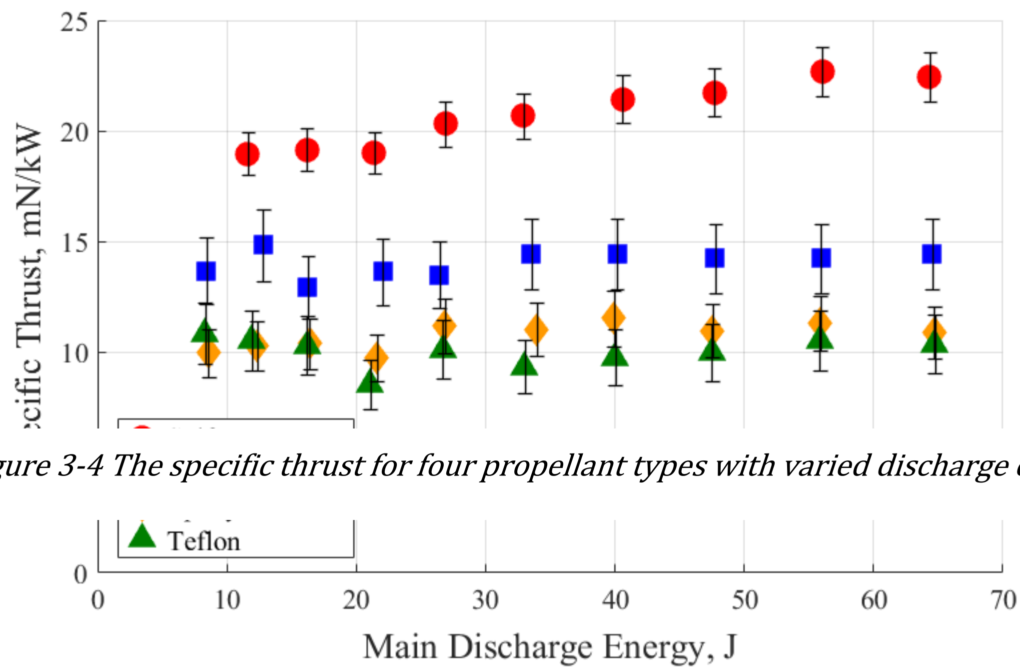

Figure 3-4 The specific thrust for four propellant types with varied discharge energies

ionized. The ionized particles are accelerated through the JxB force, where any neutral particles expand with lower velocity as a warm gas. A higher ionization fraction results in greater propellant mass utilization efficiency.

Figure 3-4 shows sulfur and bismuth sulfide specific thrust values outperforming the standard Teflon propellant, which was within error of the majority of other propellants across all energies. Table 3-2 Specific thrust for a variety of propellants in a 20J, 1" PPT gives the specific thrust for each of the nine propellants at 20J.

Table 3-2 Specific thrust for a variety of propellants in a 20J, 1" PPT

Propellant	Gallium	Teflon	Bismuth	Epoxy	Lead	Olivine	Chalcopyrite	Bi_2S_3	Sulfur
Specific Thrust (mN/kW) at 20J	7.9	8.5	9.0	9.7	9.8	10.5	11.0	13.6	19.0

The plasma velocity of sulfur propellant is typically between 68% and 81% of the Teflon plasma velocity across tested energies. However, reported ablation rates of Teflon propellant at 2.3 μg/J are only 62% of the 3.7 μg/J measured ablation rate of sulfur propellant [Keidar]. Finally, sulfur is not prone to charring at low energy densities in the manner Teflon has been shown to, making it a more reliable propellant.

3.4.2 Geometry Testing

At constant propellant surface area, a smaller number of points results in higher electric fields at the points but a smaller area between the tip of the points and the center electrode. The points create areas of high static electric field as shown Figure 3-5, which allows for consistent discharge of the main circuit.

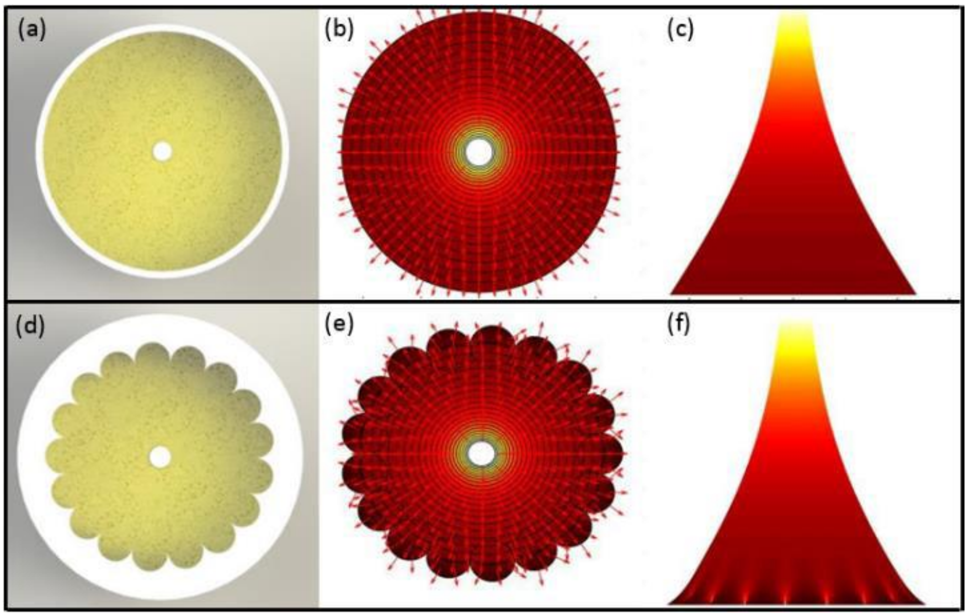

Figure 3-5 Geometry and electric field strength of smooth and 17 point serrated PPTs. Smooth (top) and serrated (bottom) geometry (a&d), electric field strength in color and direction by arrows (b&e), absolute electric field in color and potential in height (c&f)

For the 8, 12, and 17-point configurations with constant propellant surface area, the larger number of points resulted in higher specific thrust. Figure 3-7 depicts the comparative Tsp gains of the current geometry over that of the smaller Teflon PPT, the smooth geometry and the serrated geometry with fewer points at a discharge energy of 20 Joules. The increasing Tsp with an increasing number of points lends to the conclusion that the greater surface area between the points and the center electrode results in increased ablation. Though the image of the 8-point configuration in Figure 3-6 shows discharge from all points, examination of the propellant surface after 1,000 shots shows asymmetric ablation. On the 12- and 17-point configurations, uneven ablation is not seen.

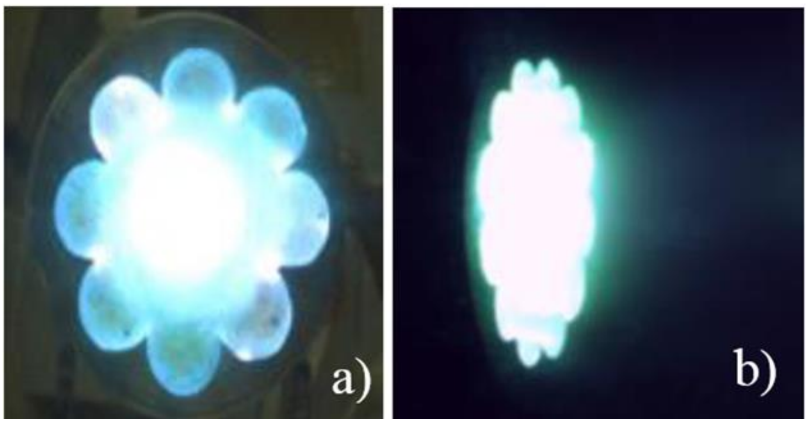

Figure 3-6 Plasma discharge from serated cathode geometries with a) 8 and b) 12 points

The large improvement over the smooth geometry is mainly attributed to poor breakdown performance at the low electric fields. In some cases, the main capacitors did not fully discharge during the pulse, decreasing the effective energy of the discharge. Misfires with this geometry, where the ignitor did not initiate a discharge of the main capacitor bank, happened with greater frequency than other electrode configurations. A final possible factor in the increase seen over the smooth geometer is number of pulses. The smooth geometry thruster had been used in previous testing. Though the electrodes were cleaned by sanding followed by isopropanol wipes, visible alteration of the cathode remained, and the sulfur had previously been fired on. Lifetime testing in Section 4.3.4 indicates that misfire rates when using sulfur with Al 6061 cathodes leads to increased misfire rates over time.

Table 3-3 Thrust stand results for 17-point serrated cathode

	Test Number	w (rad/s)	Impulse (N-s)	Specific Thrust (mN/Kw)	
17- point Serrated cathode, 19.1 J	14001	0.01326	8.85E-04	46.35	**Average**
	14002	0.01328	9.05E-04	47.38	45.63
	14003	0.01329	9.06E-04	47.42	**Standard Dev.**
	14004	0.01328	8.73E-04	45.70	1.31
	14005	0.01329	8.74E-04	45.77	
	14006	0.01327	8.83E-04	46.24	
	14007	0.01328	8.39E-04	43.91	
	14008	0.01327	8.83E-04	46.21	
	14009	0.01328	9.08E-04	47.52	
	14010	0.01329	8.32E-04	43.55	
	14011	0.0133	8.43E-04	44.13	
	14012	0.01328	8.64E-04	45.23	
	14013	0.01329	8.37E-04	43.8	
	14014	0.01329	8.72E-04	45.63	

Fit results to 17-point serrated cathode thrust stand data are shown in Table 3-3. The angular frequency of the fit, w, is checked for consistency. The angular frequency is a characteristic of the pendulum, so fits that do not converge to the correct angular frequency are considered invalid. The calculated specific thrust is considerably higher than previous testing. This is attributed to a combination of the increased surface area and a change in the setup. For the geometry comparison thrust stand setup, the capacitors were moved from the outside of the bell jar to the inside. The movement of the capacitors reduced the length of the lines and number of solder connections between the capacitors and electrodes, decreasing the resistance and thus impedance of the circuit. The type of capacitor was also changed to a thin film.

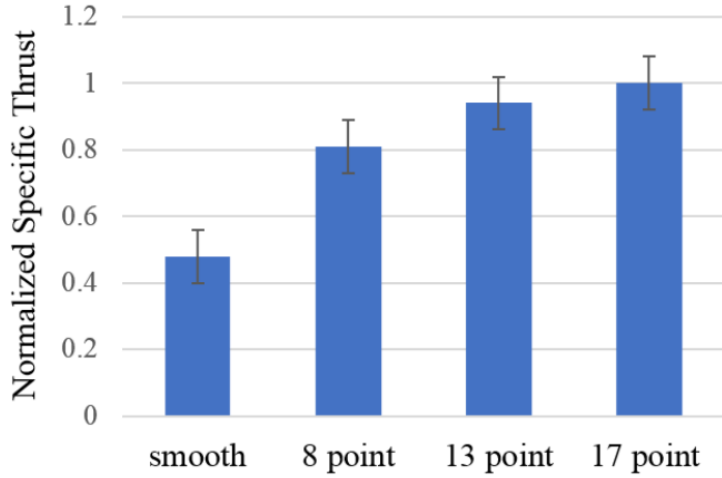

Figure 3-7. Normalized specific thrust for a 20J PPT discharge using sulfur fuel and serrated cathode geometries

3.4.3 Mass ablation and Time of Flight Results

The methods for calculating mass bit and time of flight were used only on the sulfur fuel 17-point geometry at ~20 J.

Initial attempts at a mass bit calculation were negated by small amounts of crumbling of the sulfur pucks during handling. To overcome this issue, the PETG plastic backing from the molding process described in Section 4.2.5 was left on the sulfur. This backing is not exposed to the plasma and is believed to not affect the ablation results. Given the small change in mass due to ablation, any additional loss of sulfur entirely negates the results. Every effort was taken to avoid mass loss during handling, and visual inspections were used to verify that there was no damage to the fuel.

For the mass bit calculation, results are given in Table 3-4. The top half of the table is the collected data. The bottom of the table are calculated values based off the data, with errors. The standard deviations of the mass measurements were less than the significance of the scale, so error on average masses is assumed to be 0.5 mg. The uncertainty is then propagated, with the number of pulses treated as a known integer and uncertainty on the energy based off capacitance and voltage measurements.

Table 3-4 Mass bit calculation data

Mass type	Initial mass (g)	Average initial mass (g)	Final mass (mg)	Average final mass (g)
Test mass	41.4062	41.4059	41.2235	41.2234
	41.4059		41.2233	
	41.4057		41.2234	
Control mass	40.3772	40.3775	40.3337	40.3337
	40.3780		40.3337	
	40.3774		40.3336	
	Units		**Value**	**Uncertainty (±)**
Test mass loss	mg		182.5	1.0
Vacuum mass loss	mg		43.8	1.0
Number of pulses	#		2073	
Mass bit	µg/pulse		66.9	1.0
Energy	J		19.2	0.3
Ablation rate	µg/J		3.48	0.07

Mass loss due to crumbling during handling is not accounted for in this uncertainty. It would give a significantly elevated mass bit and was avoided. The change in mass due to vacuum conditions and return to ambient conditions was controlled through the control mass with equal surface area. Sulfur ablated as a result of late time ablation on the heated surface of the test mass is also not accounted for. It could result in an artificially increased mass bit calculation.

Time of flight data is given in Figure 3-8. Over 30 measurements were taken at each probe height. Measurements averaged to 16.14 μsec and 20.71 μsec for 27 cm and 32 cm distances, respectively. Standard deviations were 1.06 and 1.22 μsec. This gives a plasma velocity of 10.9 km/s with an uncertainty of ± 3.9 km/s. Despite the large number of measurements, uncertainty is high due to the wide variance in peak arrival time.

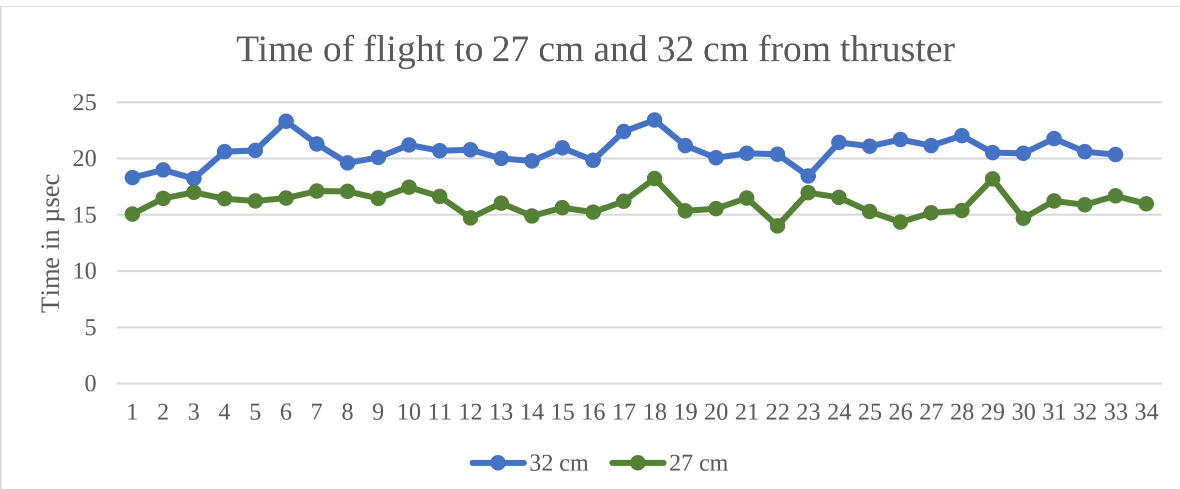

Figure 3-8 Time to peak current on langmuir probe at 27 cm and 32 cm from thruster. Measurements at the two distances were taken independently.

3.5 Discussion of resulting thruster

3.5.1 Thruster characteristics

The pulsed plasma thruster characteristics for a sulfur fuel, 17-point serrated cathode thruster operating with approximately 20 Joules are given in Table 3-6 in comparison to other published thrusters. The specific thrust for the UW thruster, as designed and tested in a benchtop set-up, is two to four times higher than other systems.

The numbers from Table 3-6 are calculated using the following constant and observed values. The ablation rate was determined by measuring mass loss over a several thousand pulses.

Table 3-5 Summary of thruster characteristics, their calculations, and values for a 20J sulfur thruster utilizing the 17 point serrated geometry.

Metric	**Symbol and equation**	**Value with units**
Voltage	V	976 *Volts*
Capacitance	C	38 μF
Energy	$E = 0.5CV^2$	18.10 *J*
Impulse bit	I_{bit}	820 $\mu N0*s$
Specific Thrust	$Tsp = I_{bit}/E$	45.3 *mN/kW*
Mass bit	$M_{bit} = \frac{[(total\ mass\ loss)-(vacuum\ mass\ loss)]}{(number\ of\ pulses)}$	67.0 μg
Ablation rate	$abr = M_{bit}/E$	3.5 $\mu g/J$
Specific Impulse	$Isp = \frac{I_{bit}}{g * m_{bit}}$	1200 *s*
Effective Exhaust Velocity	$v_e = Isp * g$	11760 *m/s*
Efficiency	$\eta_T = \frac{I_{bit}^2}{2m_{bit}E} = 0.25$	25%

It is important to note that the efficiency here is thruster efficiency. It does not consider the efficiency of the electronics supplying the energy to the capacitors. In Table 3-6, charging of the main capacitors is given as 70%. On optimized electronics for a CubeSat, the charging efficiency could be increased to as much 90% with a slight increase in charge time. This would lead to an overall efficiency of up to 22.5% when taking both thruster and charging efficiency into account.

Table 3-6 Comparison of reported characteristics of pulsed plasma thrusters

Pulsed plasma thruster	Specific Thrust [mN/kW]	Isp [s]	Ibit [μN*s]	Total impulse [N*s]	Thrust [mN]	Efficiency [%]
UW	46	1 200	820	1150	0.46	22.5
Clyde Space	16	590	35	30	-	5
Busek uPPT	-	700	490	220	0.5	-
Aerojet	12.4	1350	100-750	3000	1.24	9.8
Dawgstar	11.2	483	56.1	200	0.112	1.8
LES 8/9	23.5	1000	297	7300	0.6	7
NOVA	12.5	850	378	2224	0.375	7.8
ADD-Simplex	20	2620	1200	1200	1.37	14

3.5.2 Thruster applications

3.5.2.1 Satellite mass, fuel mass, and Δv

With the thruster characteristics given in Table 3-5, the mass of fuel, m_{fuel}, needed for a particular mission Δv can be calculated using the starting mass of the full satellite, $m_{initial}$, and the specific impulse, Isp, as

$$m_{fuel} = m_{final} * (1 - e^{-\frac{\Delta v}{I_{sp} * g}}) \quad \textit{Eqn 17}$$

For example, starting with and unfueled, or dry, mass of 4 kg, 34 grams of fuel is needed to achieve a theoretical Δv of 100 m/s. Rearranging this equation with $m_{fuel} = m_{initial} - m_{final}$ gives:

$$\Delta v = Isp * g * \ln\left(\frac{m_{initial}}{m_{initial} - m_{fuel}}\right) \quad \textit{Eqn 18}$$

Figure 3-9 shows this calculation for several initial satellite masses from 3 to 24 kg. The satellite "wet-mass" includes the propulsion system, fuel and the rest of the satellite as $m_{initial}$ in the equation above. The plot on the right shows a smaller range of the plot on the left, in order to zoom in on the lower range of m_{fuel}. It is worth noting that the lines are not linear. They are approximately linear for small ΔV but become nonlinear for ΔV's above 1 km/s.

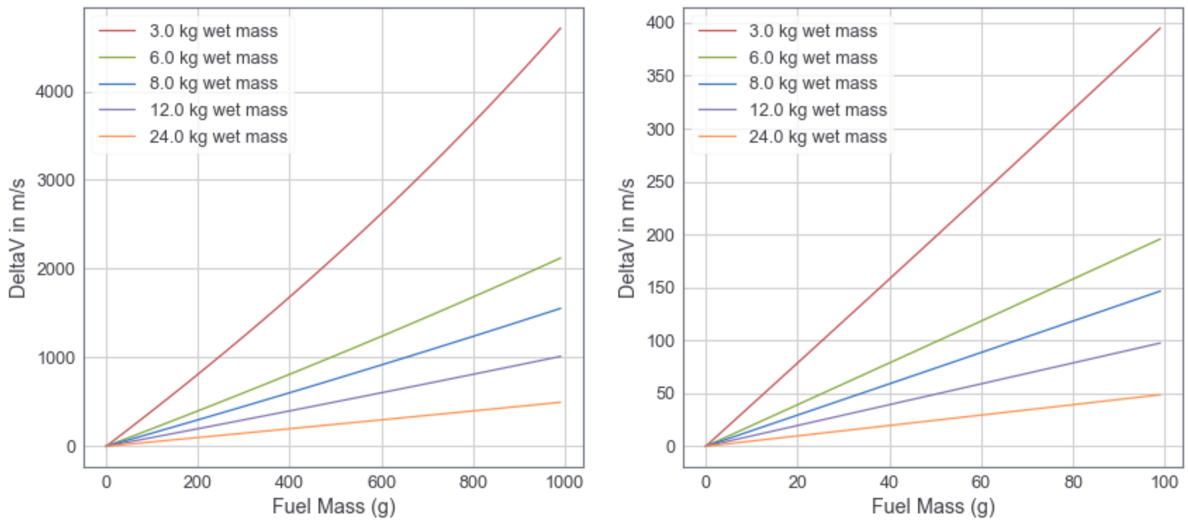

Figure 3-9 ΔV using the 20J PPT system based off onboard fuel mass for satellies of different wet mass. Higher (left) and lower (right) fuel ranges are for clarity

Using the same equation as above to calculate the relationship between fuel mass and Δv, Figure 3-10 overlays a second layer of dashed lines read out on the right axes. These lines give the fraction of the total satellite mass that is available for other systems. This calculation was made assuming a base mass of the propulsion system of 750g. This number is estimated using the capacitor mass, the assumption of a small propellant feed system, and the mass of the system assembled in Chapter 4. The mass of the propulsion system in total is the base mass plus the required fuel, and the mass left for the remaining system is the total propulsion system subtracted from the given initial mass, or wet mass. This is represented as:

$$Non - propulsion\ fraction = \frac{(m_{initial} - m_{baseprop} - m_{fuel})}{m_{initial}} \qquad Eqn\ 19$$

On a 3kg satellite, the base mass of the propulsion system means the other systems are allocated only ~ 75% of the mass, or 2250 g. 2250 g is on the low end of what is possible to outfit the satellite with necessary power, communications, and attitude control and determination for the propulsion to be effective. As the fuel mass increases past two hundred grams, the propulsion system as proposed becomes inviable as part of a complete 3kg satellite. On the other hand. For the larger satellites, even 1 kg of fuel leaves each system with more than 70% of the mass to be used for non-propulsion systems and an ability to exceed 1 km/s Δv.

For the larger amounts of fuel, it is reasonable to expect that the base mass would increase slightly for a more complex feed system. This makes the non-propulsion fraction and mass an overestimate at the higher fuel levels. The full calculation of Δv possible given a fuel mass is an upper bound, as a thruster may degrade over its lifetime or have other inefficiencies.

Because the fuel is a solid, the stored fuel requires a particular envelope, as opposed to tanks which hold gasses or liquids. Multiple systems or considerably more complex feed systems become more useful when using more than 1 kg of fuel. The solution for the asteroid mission in Section 2.1.3 included two independent PPTs in order to fit the required fuel in the 24U envelope without undue interference with other systems. When multiple systems are present, it is possible to design a satellite in such a way that they can also aid in the attitude control system by firing one with greater frequency than another. This is potentially useful for the desaturation of reaction wheels.

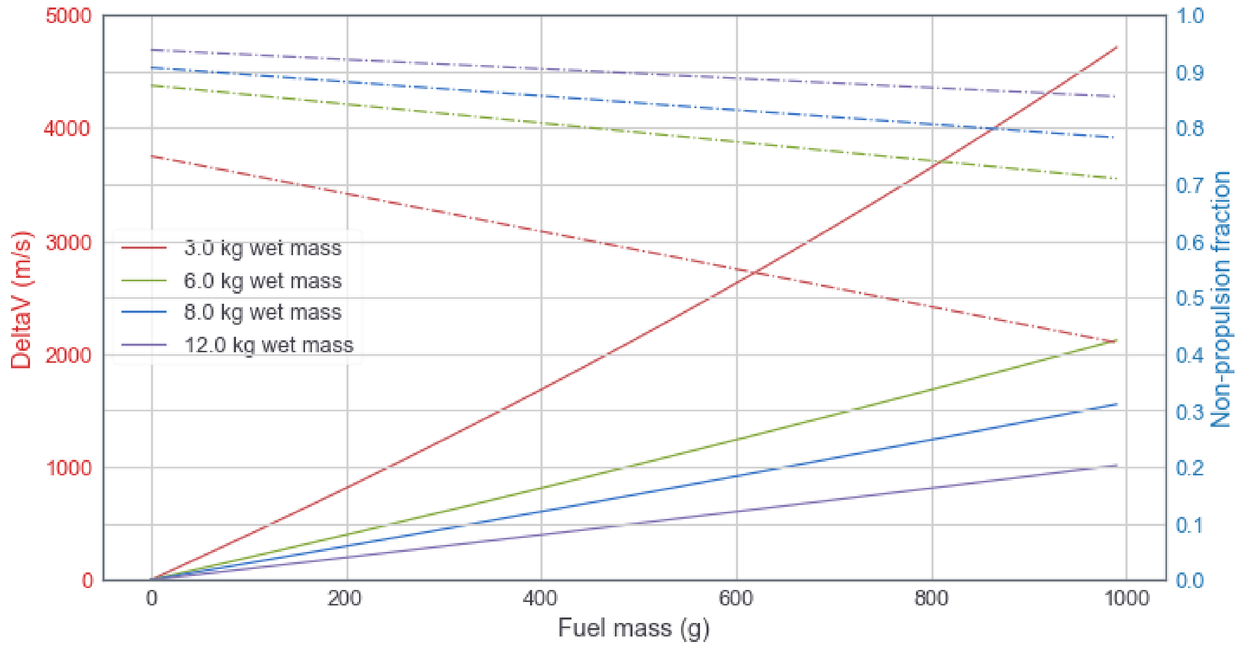

Figure 3-10. ΔV given fuel mass (solid lines) with and added overlay of the fraction of the satellite mass not used for the propulsion systems (dashed lines)

The methods used above are useful when given a fixed mass budget for a science mission and describe expected Δv from the mass-budgeted fuel. A different approach examines the fuel need to reach a required Δv given a satellite system where the non-propulsion mass is fixed, and the propulsion system is extra. While propulsion should be considered in tandem with a satellite development, it is possible for a science team with ideas on instrumentation requirements to "shop" for a propulsion system. In that case, the interest is in the ability of a propulsion system to meet the required Δv of the science satellite, with less concern for total mass. Figure 3-11 shows the fuel needed for a given Δv where the satellite mass does not include the propulsion system or fuel. The equations then become:

$$m_{fuel} = (m_{sat} + m_{baseprop)} * (e^{\frac{\Delta v}{I_{sp}*g}} - 1) \qquad Eqn\ 20$$

and

$$Non - propulsion\ fraction = \frac{m_{sat}}{(m_{sat} + m_{baseprop} + m_{fuel})} \qquad Eqn\ 21$$

where m_{sat} is the mass of all non-propulsion satellite components.

With Δv now on the x-axes, it is more apparent how increased satellite mass requires increased fuel to reach the same change in velocity. It is also notable that starting with a satellite mass of 3 kg and adding propulsion to meet the Δv goals makes more sense than trying to fit a propulsion unit with a 3 kg limit.

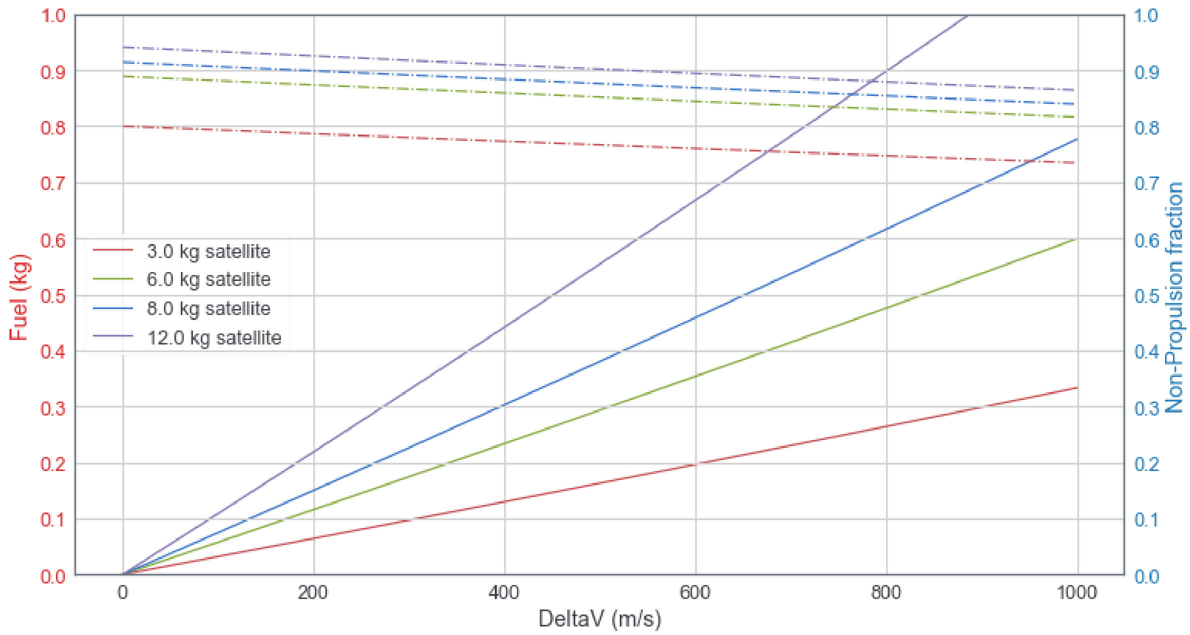

Figure 3-11 Fuel needed to reach given Δv (solid) and mass fraction of the non-propulsion system (dashed) for CubeSats where the mass excludes the propulsion

3.5.2.2 Timing constraints

The speed at which the Δv is achieved, or acceleration, is an important factor for some mission deigns. In pulsed systems, this can be as low as desired by pulsing at lower frequency. Upper limits for this system are based off the power available up to a limit, and then followed by heat generation concerns.

When considering a system with discrete impulse bits, pulse frequency is a defining factor. The mass flow rate, $\dot{m}$, is then

$$\dot{m} = m_{bit} * freq \qquad \text{Eqn 22}$$

The thrust output, T, is

$$T = I_{bit} * freq \qquad \textit{Eqn 23}$$

and the average power required, P_{ave}, is

$$\mathrm{P_{ave}} = \frac{\mathrm{E}}{\eta_{\mathrm{E}}} * freq \qquad \textit{Eqn 24}$$

where η_E is the decimal charging efficiency, here estimated to be around 0.75, and later tested to be 0.77 or 77% in Section Main charging system miniaturization characteristics4.3.5.

Firing at $freq = 1\ Hz$ simplifies these calculations. The power is then 18.1 over 0.75, for an average power of around 24.1 Watts. The satellite power system then needs to be capable of supplying 24.1 Watts of power while firing a 1 Hz. Further, the power draw for charging capacitors is variable, so the system must be designed to handle short bursts of much higher power. This includes low resistance pathways for high current flow. Firing at a lower frequency reduces the average power requirement and can also be designed to lower the peak power draw.

If power concerns are not a limiting factor in firing frequency, thermal concerns are. Assuming an overall efficiency, including thruster and charging efficiencies, of around 20%, and an energy of 24.1 J from the 24.1 Watts and 1 Hz, 19.5 J of energy are not being converted into kinetic energy. Instead, the energy not transferred into kinetic energy of the exhaust remains in the system as added heat. For long duration operation at this power level, thermal modeling and control is required to avoid reaching temperatures hot enough to boil off the sulfur fuel.

Finally, the thruster charging and firing are high current events that radiate electromagnetic noise which can interfere with communications or science observations. Windows of non-operation are needed for the operation of other systems. This further limits the acceleration of the satellite. Figure 3-12 shows an example of time for satellites of different masses to reach various velocities assuming a 1 Hz firing frequency operating one third of the time on average. Table 3-7 gives values for Δv after 30 days operation and time to reach 100 m/s Δv, both using the one third average operational time. The equations for this were based off the work from the previous section fuel consumption for Δv, and the 67.0 μg mass bit:

$$days = \frac{m_{fuel}}{m_{bit}} * \frac{1day}{86400s}$$

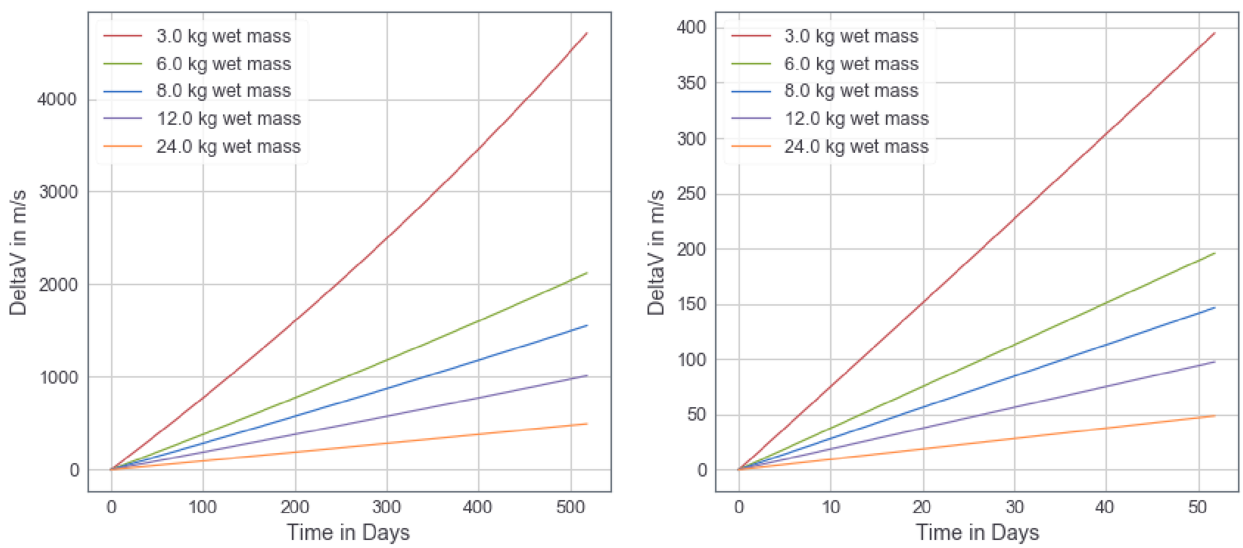

Figure 3-12 Change in velocity over time for satellite of different starting mass assuming the thruster operating one third of the time and firing at 1 Hz when operating.

These numbers inform the options for missions utilizing a PPT. Small spacecraft in the 4-7 kg range can reach Δv of 100 m/s in under a month. This is ideal for a small CubeSat trailing the Europa Clipper. Δv of km/s require closer to a year for this mass range, though a small, powerful system firing at a high duty cycle could achieve 1 km/s in only a few months. PPTs on spacecraft in the 12 to 24 kg range are more suited to longer term missions. 1 km/s Δv for the single thrusters on the larger satellites require ~1 kg of fuel and one to two years. This regime is in line with plans for an asteroid exploration mission.

Table 3-7 Timing of Δv delivered to CubeSats assuming a one third duty cycle at 1 Hz.

Spacecraft wet mass (kg)	**dV after 30 days (m/s)**	**Days to reach 100 m/s dV**
3	230	13
6	114	26
8	86	35
12	57	55
24	28	106

3.6 Conclusions

Pulsed plasma thrusters are of interest for CubeSat propulsion due to their simple design and solid, inert fuel. Many universities have done research on benchtop PPT systems, and PPTs have provided attitude control on larger missions. The typical limits of CubeSat operation, including those on power and lifetime, motivate increasing the specific thrust. The number of ways in which changes to materials, geometries, and operational energy can be made is unbounded, so this work found optimizations in fuel type and geometry to increase the specific thrust and utility in CubeSat propulsion. Fuel type and propellant surface area proved to have major contributions to the increase in specific thrust for pulsed plasma thrusters.

The capabilities of the resulting laboratory set-up are sufficient to deliver up to km/s Δv to CubeSats ranging from 3kg to 12kg. Multiple units would be needed for high Δv on larger satellites. A 3kg satellite is the lower limit for this propulsion system to be useful, given the relative mass of the base propulsion system.

For the thruster to enable CubeSat science missions, it must be demonstrated to work in a CubeSat formfactor. The next step is to explore and complete the design of hardware capable of CubeSat flight.

Chapter 4. Pulsed Plasma Thruster for in-space testing

4.1 Introduction

Chapter 4 addresses the transition of the PPT from a benchtop experiment to a CubeSat capable thruster. The three areas of innovation are components able to withstand the harsh discharge and space environment over the life of the thruster, miniaturization of components to fit in a CubeSat formfactor, and designing an operations plan that demonstrates the abilities of the thruster on a CubeSat. The culmination of this section is a thruster designed and tested to operate as a main propulsion system on nanosat class satellites. This brings the system to TRL 6 as a necessary step in enabling the PPT as a flight system.

Examples of Pulsed plasma thruster testing to reach flight models for nanosatellite propulsion include the Dawgstar and PROITERES pulsed plasma thrusters [Rayburn, Naka]. Main concerns with electric thrusters, including Hall and Ion thrusters as well as PPTs, are the degradation of material exposed to plasma over the lo ng operational timescales [Manzella, Ira]. This work discusses the methods used in testing, results in looking for solutions to issues encountered during the transition, and integration into a CubeSat design capable of operating with other subsystems.

4.2 Methods

4.2.1 Vacuum chamber testing

All vacuum testing was conducted in a bell-jar vacuum chamber of 100cm height and 44cm diameter. Testing pressures are maintained between 5.5E-5 and 9.0E-6 Torr. Electrical high voltage and signal feedthroughs as well as physical feedthroughs for changing the position of the

Langmuir probe are utilized for testing. Labview is used for precision timing and data acquisition from a Tektronix TDS3034B oscilloscope and a U12 LabJack.

When counting successful shots vs misfires during bell-jar testing, a photoresistor running on an Aruino Uno was used. When the thruster was triggered, a logic pulse was sent to the Arduino. The Arduino then checked the output of the photoresistor. If the output went above a calibrated value, the pulse was successful.

4.2.2 Imaging of electrode wear

Magnified images for comparing electrode wear were taken using a Dino-Lite handheld digital microscope.

4.2.3 Thrust stand apparatus and calculations

A Micro-Epsilon MDS-45-M18-SA magnetic inductive displacement sensor was utilized for measuring displacement of a hanging pendulum thrust s tand. The characteristics of the pendulum, including moment of inertia, were modeled using Onshape, as shown in Figure 4-1, and checked

Figure 4-1 Pendulum modeled using Onshape (90 degree rotation)

against measured values of mass and center of mass.

Mass was measured a single time by placing the entire pendulum on a scale accurate to 0.1g. Mass of individual components used in the Onshape model were also determined this way. Center of mass was measured by balancing the pendulum on a razor blade, then measuring from the balance point to the pivot point to the nearest mm with a straight edge. Two measurements were taken with the same result. Angular frequency was taken from the average frequency calculated in initial curve fits to the 20 traces. A comparison of modeled and measured values is provided in Table 4-1.

Differences in mass are due to rounding and the addition of tape to secure the magnet. The mass of the magnet was updated to reflect the additional mass. For this adjustment, the modeled angular frequency increases to 5.5 rad s^{-1}, which is a 2% difference from the empirical solution taken from the average of the damped sine fit of the 20 traces. The modeled angular frequency is within the standard deviation on the fitted angular frequency of 0.15 rad s^{-1}.

Table 4-1 Pedulum charateristics from Onshape model and observed values

	Modeled Value	**Measured Value**
Mass (kg)	0.041	0.043
CM to pivot (m)	0.266	.267
Moment of inertia (kg m^2)	3.675 *10^{-3}	** 3.514 *10^{-3}
Angular frequency (rad s^{-1})	** 5.41	5.66
** in either case, moment of inertia or angular frequency was calculated based off the other quantities, ** is the calculated variable using $\sqrt{\frac{mgL_{cm}}{I_p}} = \omega$		

Angle of deflection is calculated by fitting an underdamped sine wave to the output voltages,V, of the magnetic sensor with amplitude, A, damping force, c, angular frequency, ω, and s as the phase.

$$\mathrm{V(t) = offset + Ae^{-ct} * \sin(\omega t + s)} \qquad \textit{Eqn 25}$$

The amplitude, A, of the output voltage is then the maximum voltage that would be reached without damping once the offset is subtracted. Combining A with the sensitivity gives the displacement of the pendulum at the location of the sensor. The inverse sine of that displacement divided by the distance of the magnet to the pivot point gives the corresponding maximum angle of deflection, θ_o. θ_o is used to solve for impulsive torque, or impulse bit multiplied by the distance of the thruster to the pivot point, in

$$I_{bit} * L_x = \mathrm{I_p}\dot{\theta} \qquad \textit{Eqn 26}$$

Where L_x is the distance from the applied impulse to the pivot point, $\mathrm{I_p}$ is the moment of inertia of the pendulum around the pivot point, and $\dot{\theta}$ is the angular velocity at $\theta = 0$:

$$\dot{\theta} = \theta_o \sqrt{\frac{mgL_{cm}}{I_p}} = \theta_o \omega \qquad \textit{Eqn 27}$$

With θ_o as the maximum angle of deflection and L_{cm} as the distance between the pivot point and the center of mass of the pendulum. We can then solve for the impulse bit with known quantities

$$I_{bit} = \frac{\theta_o}{L_x} I_p mgL_{cm} \qquad \textit{Eqn 28}$$

This treatment varies from that described in the previous chapter because the moment of inertia is modeled and confirmed with empirical data. The previous chapter uses a moment of inertia calculated assuming the pendulum is a point mass on the end of a stiff masses rod.

The sensitivity of the sensor in mV/mm is calibrated in the setup by taking static traces of the magnetic sensor output while plastic shims of 4, 6, 8, and 10 mm thickness (0.2 mm measurement uncertainty) are between the sensor and the pendulum. The average across a full oscilloscope trace is used as the value for that trace. With three traces per distance, the twelve points are then used to fit a sensitivity slope. The sensitivity with a 6.6V input to the sensor is calculated to be 152 mV/mm with an uncertainty of 11 mV/mm, or 7 %.

4.2.4 Accelerated lifetime testing

Lifetime testing on electrical components is accelerated through use of an in-air "thunder-box" setup. Lifetime testing any components to one million repetitions is a slow process. This is especially true if hours are needed between tests to make changes in the vacuum chamber. For thruster firing in the vacuum chamber, seconds between pulses are required to stay within designated temperature and pressure ranges. Electrode and thrust testing cannot be conducted outside of the vacuum chamber, but the thunder-box setup allows for electronics testing.

The thunder-box can operate at over 20 Hz. When operating continuously at high frequency, temperature and electrical characteristics are checked every 30 min. Firing at 20 Hz reduces the active time for one million shots to ~15 hours down from over 20 days if firing at ½ Hz. When problems arise in the setup, they can be quickly addressed without waiting on vacuum systems.

Figure 4-2 depicts the thunder-box. In the square on the right, tungsten rods insulated in ceramic are used for the anode and cathode coming in from the sides, while the ignitor comes in from the top to form and inverted T. The small 1 mm gaps between the main electrodes and the ignitor allow for the main discharge in air. The capacitors and ignitor coil are also in the box and are cooled with circulation from the fan. Two in-house built benchtop power supplies are used to supply the power needed to charge the capacitors at high frequency.

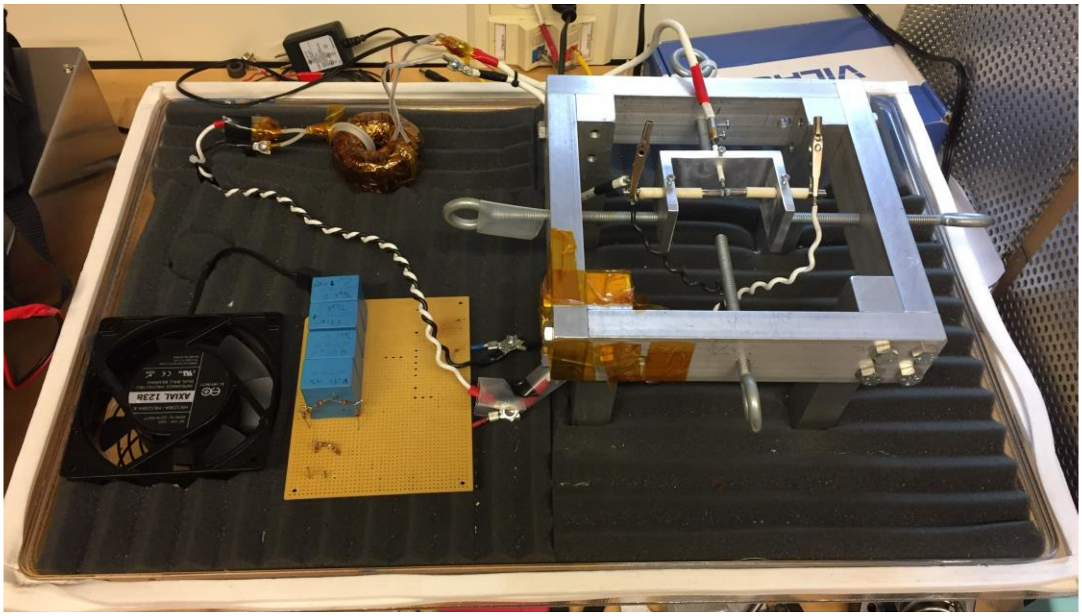

Figure 4-2 Thunder-box setup for accelerated component testing

The box is made of plastic and insulated with sound absorbing foam. The foam reduces visibility of the flashing in addition to the volume of the staccato discharge. When the lid is on the box, exhaust is vented through a snorkel to the exterior of the building to avoid a buildup of ozone from the arcing. The lid also distances the high voltage from the user or other outside interference. An Arduino Uno with an adapted pushbutton code and potentiometer for setting the pulse frequency controls the thunder-box charging and firing electronics.

4.2.5 Sulfur propellant fabrication

A standard operating procedure is needed to create consistent sulfur fuel pucks. Early attempts lead to inconsistencies and brittle sulfur pucks. In order to form the fuel, 99.9% pure sulfur powder is used as the starting point.

The fuel needs a consistent shape, so 3D printed molds from PETG filament are used, as seen in Figure 4-3. For ease in removing the formed pucks, the molds are lined with Kapton tape. The sidewalls of the molds are thin enough to peeled off from the outside. Tungsten rod identical to that of the anode is used for the center of the mold. A layer of Kapton tape around it ensures that there is tolerance for the anode to slide into a finished sulfur puck.

Figure 4-3 Sulfur puck formation with 3D printed PETG molds, tungsten center rod with aluminum heat sink, hot plate heating, and final pucks shown

The remainder of the process takes place within a fume hood. The powdered sulfur is heated slowly in a crucible using a hot plate just until it reaches the melting point of around 115 C. At this time, it forms an amber liquid similar to the color of the Kapton tape. It is important not to burn the sulfur or heat it to a point that the S8 structure breaks down, which may start to happen at temperatures over 119 C [Greenwood].

The heat sulfur is poured into the mold. The central area cools more slowly than the exposed surfaces, and brittle crystals with air pockets may form in that area. A heat gun is used to re-melt the surface to remove the crystalline areas. The sulfur is left in the fume hood or other ventilation to completely cool and then the mold is peeled off. Gentle sanding can be used to adjust the shape.

An industrial CT scan of the sulfur puck in the thruster is used to analyze the success of the method.

4.3 RESULTS

4.3.1 Electrode material selection

Initial fatigue testing compared Al 6061, Al 7075, and stainless steel as cathode materials. Al 6061 had been used up to this point as an inexpensive and easily machinable material. Longer term testing resulted in buildup on the surface of the material, which reduced performance and motivated this test. Smooth cylinder cathodes were used for ease of assembly for this test.

The Al 6061 had 7397 total attempts with 417 misfires, for a 94.3% success rate. The test was ended due to failing capacitors. The Al 7075 cathode was tested to 66000 total attempts with 34 misfires, for a 99.9% success rate. The test was ended when the thin layer of fuel was reduced to its backing. The stainless-steel test went on for 26000 total attempts with 1275 misfires, for a 95.1% success rate. Figure 4-4 shows the buildup on the various cathode types.

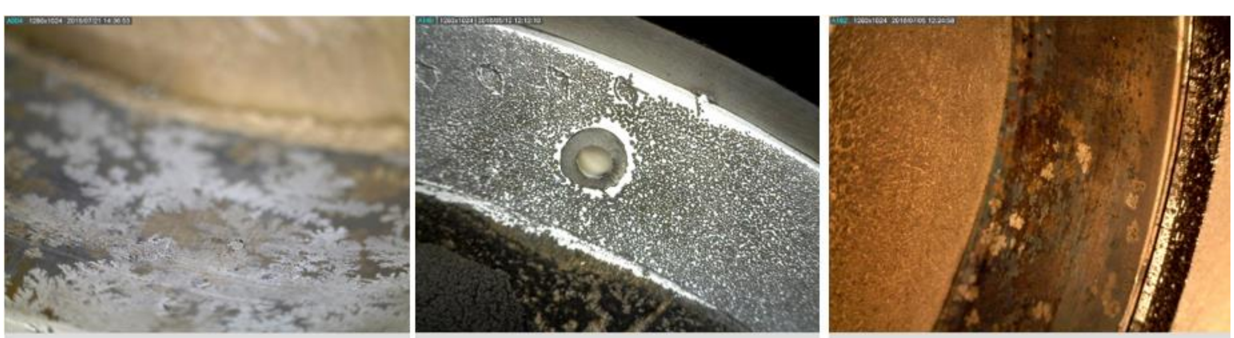

Figure 4-4 Buildup on cathode using AL 6061 (left), AL 7075 (center), and stainless-steel (right).

Al 7075 had the highest firing rate of the materials tested. This remained true even when the sulfur fuel had burned through, and the thruster was ablating the PETG plastic backing. The PETG has carbon elements which often result in charring and reduced performance in PTFE fueled thrusters. Al 7075 is an aluminum alloy with zinc as the main element. It exhibits high strength, good corrosion resistance and is commonly used in aerospace applications (Hodgson, 1990). Testing going forward is conducted with Al7075 cathodes.

Tungsten was used as anode material for its high melting temperature. The wear from 25000 and 100000 pulses is shown in Figure 4-5. It is apparent that repeated firing does wear the anode, and that the most wear occurs on the leading end. The amount of wear on the hundred thousand pulse anode was less than 1/20th of the diameter, and thus considered acceptable for a 1 million pulse system.

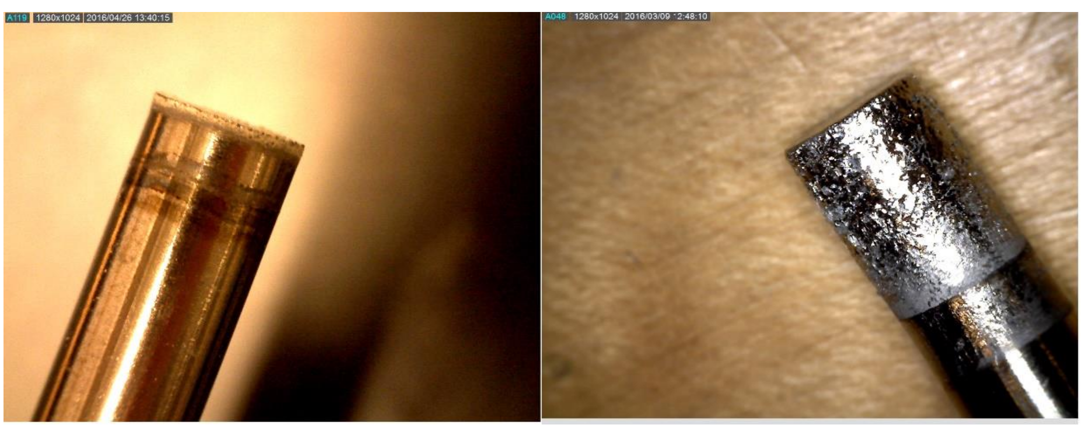

Figure 4-5 Tungsten anode after 25000 pulses (left) and 100000 pulses (right)

4.3.2 Capacitor selection for miniaturization and lifetime wear

To increase the energy of the discharge without needing to increase the voltage rating on the electrical components, a high capacitance is desirable. However, there is limited volume for the capacitors and the discharge of the main capacitors is an abrupt event. Not many capacitors are rated for shorting at high voltage. Figure 4-6 is an example of the time derivative of a voltage trace during the main discharge. It reaches a maximum amplitude of $\frac{dV}{dt}$ of 279 volts per microsecond. Later tests using more representative setups had a maximum of closer to 200 volts per microsecond. Figure 4-6 also shows the long-term effect of the discharge on thin film capacitors not rated for the high discharge. Over time, capacitance is lost as holes form in the thin film layers. The two 20 uF capacitors in the Al 7075 study were previously unused.

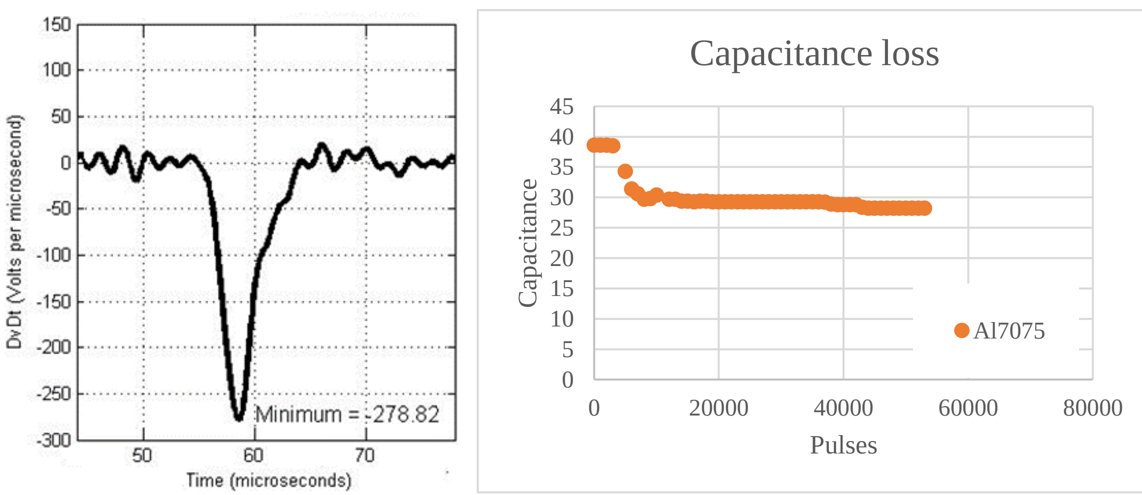

Figure 4-6 Example of the change in voltage on the capacitors over change in time during the main discharge (left) and the effect of multiple main discharge events on capacitance.

Table 4-2 contains several characteristics of the capacitors in the trade study of possible capacitors. It has a color-coded emphasis on the energy density, where green is above 5E-5

J/mm^3, yellow is between 2E-5 and 5E-5 J/mm^3, and red is below 2E-5 J/mm^3. A specific envelope was not required, but the number of capacitors needed to reach 20J or higher energy were required to fit into a CubeSat package. Those in red were deemed unfeasible, while yellow energy density levels were below expectations but feasible. Green energy density levels were considered good. Voltage ratings were required to be at least 1.2 kV. The 1.2 kV rating allows for de-rating the capacitor by at least 200 V while maintaining 1kV for the high electric field. Temperature ratings from -40 C to 75 C were also a requirement. Electrolytic capacitors were not considered as the electrolyte within them can escape if they are damaged. While not on the chart, equivalent series resistance was desired to be low to allow for the fast and efficient discharge.

Table 4-2 Capacitor selection study

Manufacturer	**Capacitance (uF)**	**Voltage Rating (V)**	**dV/dt (V/us)**	**Volume (mm^3)**	**Energy Density (J/mm^3)**	**Temp Range (C)**
EPCOS TDK	5	1300	100	25,294	@1000V, 9.88E-05	-55 to 105
Cornell Dubilier	4.7	1500	72	51,639	@1000V, 4.55E-05	-55 to 105
Vishay	5	1250	221	101,500	@1000V, 2.46E-05	-55 to 105
Illinois Capacitors	0.22	2000	2600	44,030	@1500V, 0.56E-05	-55 to 105

Kemet	1	2000	400	56,025	@1500V, 1.75E-05	-55 to 105
Cornell Dubilier	1	2000	754	71,258	@1500V, 1.58E-05	-55 to 105

No commercial-off-the-shelf capacitors were fully rated for both the needed dV/dt and energy density. The implemented solution was to take the only option with sufficient energy density, the TDK Electronics B32774D1505J000 1300V 5uF capacitors, and test them over the million-pulse desired lifetime. This test was conducted using the thunder-box setup and was done to determine if the failure to meet the dV/dt rating would result in failure of the capacitor. Eight capacitors were tested to 1 million pulses individually. No more than 2.2% loss in capacitance was observed for each. This was considered acceptable, and the project was able to move forward using the TDK 5 uF capacitors in parallel for added total capacitance.

4.3.3 Sulfur fuel puck formation analysis

4.3.3.1 CT evaluation of sulfur formation methods for density and uniformity

An industrial CT scan of the thruster was conducted at Delphi Precision Imaging. An entire assembled model of the thruster with flight hardware and engineering model PCB boards was used for the scan, but the sulfur puck was the main item of interest. Using the CT scan, it is possible to evaluate the method of sulfur propellant fabrication. For uniform thrust, uniformity in the sulfur is ideal. The amount of void space within the sulfur propellant is also of interest. Void spaces decrease the fuel mass of a given volume and have implications for outgassing or pressure buildup from bubbles of atmospheric gas within the fuel mass.

Figure 4-7 show analysis of the sulfur puck using VGEasyPore from VGStudio Max. The area around the tungsten anode is exempt due to artifacts from the high-density material.

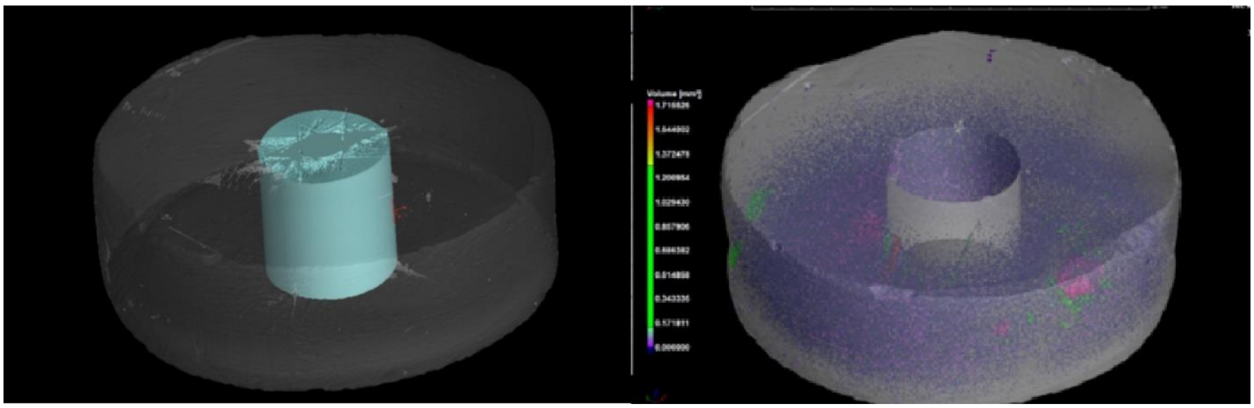

Figure 4-7 CT scan data showing the area affected by artifacts of the dense tungsten (left) and voids found within the sulfur puck (right)

Using the VGEasyPore analysis, eleven voids in the sulfur were found to be larger than 1 mm^3. Only one void space was larger than 3 mm^3, and only one additional void was larger than 2 mm^3. The material volume of the analysis is 24754.77 mm^3 and the void volume totals 247.77 mm^3. This results in a void ratio of 0.99% of the volume.

An alternative analysis of the data was conducted in MATLAB, where only slices in the Z direction were used. In the Z direction, there are minimal artifacts from the high-density Tungsten anode, and the full sulfur puck could be analyzed. Figure 4-8 is an example of a Z direction slice. Pixels are 0.039 mm per side, which is the same as the slice depth, and pixels with a greyscale value less than 12 are counted as void space. Void space pixels are highlighted in white for visibility.

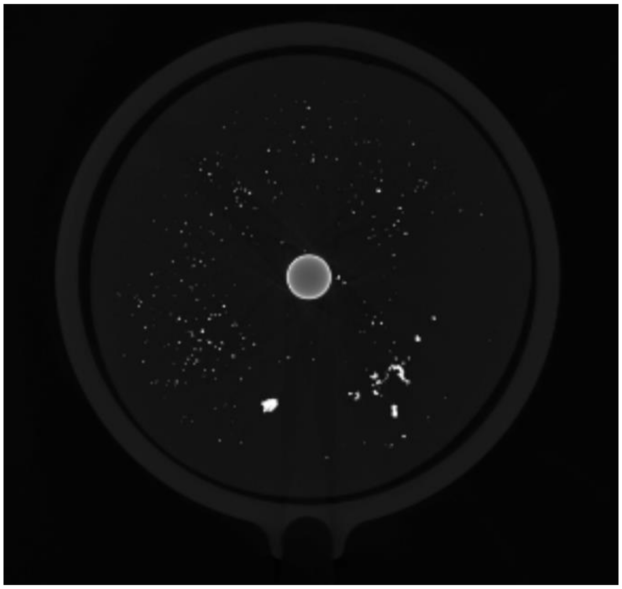

Figure 4-8 Sulfur CT scan slice in Z direction. Void spaces are defined as having a greyscale value of less than 12 and are highlighted here as white

The inclusion of the area around the anode confirms that the voids form predominantly in the slower cooling regions during the formation process. This indicates that the 0.99% void space by volume calculated without the area near the tungsten is an upper bound. A layered pour or a slower pour of the sulfur into the mold could further mitigate the formation of voids within the sulfur puck.

4.3.3.2 Outgassing results

Outgassing from void spaces within and sublimation of the sulfur pucks was a concern for the lifetime application of the thruster. To this extent it was believed that a thin coating of a different material could mitigate this effect, and then be ablated off during the first several hundred pulses. The coating was required to be non-conductive and non-reactive with sulfur, aluminum or air. The coating of choice was SiO_2. Which was added to two sulfur pucks using an evaporated coating method.

These three sulfur pucks were placed in the bell jar chamber at vacuum for a period of just over 24 hours. The turbo pump did not run overnight which allowed the pressure in the chamber to come up to around 1 millitorr from the usual testing pressure of 0.05 millitorr. Mass measurements were collected before vacuum testing, after, and again after over 24 hours in a sealed bag, represented by the third column of Table 4-3. A fourth column gives data collected over a week later.

As expected, the largest change in mass occurs between the initial measurement and the measurement immediately upon removal from the vacuum chamber. Additionally, there appears a minimal difference in the outgassing properties of the pucks that were SiO2 coated, and those that were not. The percent mass loss from 24 hours of vacuum at room temperature was no greater than 0.09%. The percent mass regained after being in atmosphere for a week was, at most, less that a hundredth of a percent.

Table 4-3 Mass loss of coated and uncoated sulfur pucks

Test:	**Description**	**Mass Before (g)**	**Mass Directly After (g)**	**Mass Percent Loss from original (%)**	**Mass After 24hrs+ (g)**	**Mass After 1 week + (g)**
Puck1	Full sized puck, uncoated	55.9612	55.9391	0.03949	55.9389	55.9368
Puck 2	Medium sized, SiO2 coated	34.2514	34.2208	0.08933	34.2194	34.2177

Puck 3	Full sized, SiO2 coated	58.2651	58.2268	0.065734	58.2263	58.2221

4.3.4 Testing of components for lifetime wear results

Utilizing the chosen capacitors, the sulfur puck formed with standard procedures, and the tungsten anode with Al7075 17-point scalloped cathode, a lifetime test was conducted. The goal of this test was to validate that the hardware exposed to the discharge was able to withstand the harsh environment without failures over many pulses.

The photoresistor setup was used with the bell-jar vacuum system and benchtop power supply to pulse the thruster in 1000 pulse groupings with 3.5 seconds between pulses. The results were 100195 successful pulses from 101000 attempts for a 99.2% success rate. The initial 12 sets of 1000, when the majority of misfires occurred, had insufficient time for charging the main capacitors. Not allowing the main capacitors to reach full charge lowered the success rate, which increases to 99.4% if the initial 1200 pulses are excluded. Firing at 90% or higher was considered successful. Over the 101 thousand pulse sets, there was no decrease in success rate.

Table 4-4 Success rate of successive groupings of 1000 pulses

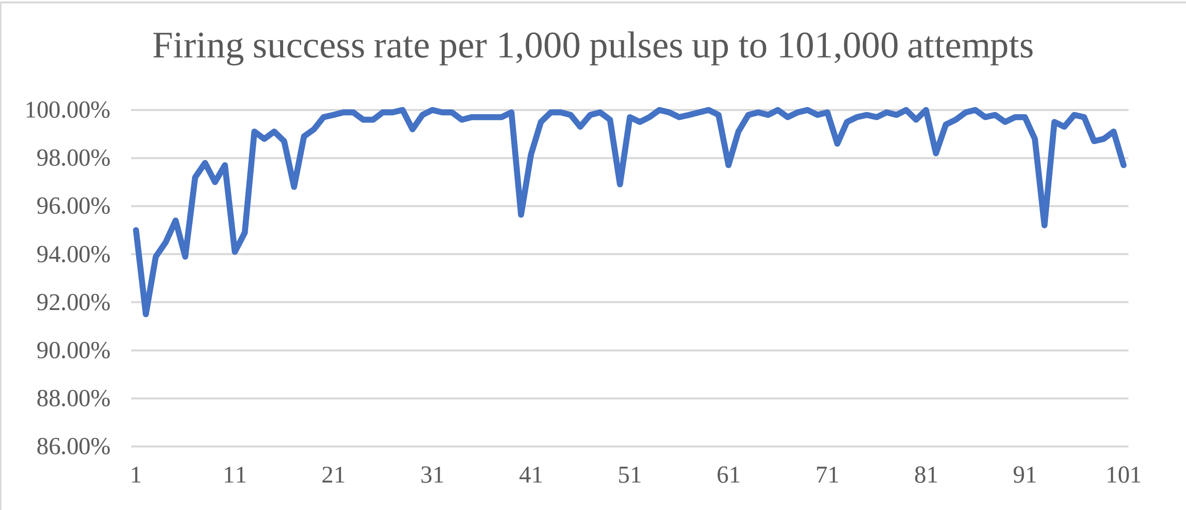

4.3.5 Main charging system miniaturization characteristics

A fly-back configuration charging system was chosen and tested to replace the large benchtop power supplies. The system is designed to take in the CubeSat battery voltage of 6.5 to 7 V and charge the main capacitors up to high voltage. An LT3750 controller (LT3750 Datasheet) with an IDP320N0N MOSFET sending a sawtooth current charging wave through a CoilCraft DA2034-AL transformer and 12 1.2 kV 1 A rated diodes in a 5-parallel 2-series configuration are the main components in the main charge system. An example of the sawtooth charging wave is shown in Figure 4-9 next to the charging board, where the miniaturized main charge system takes up approximately half of the available space on a 10 cm by 10 cm board.

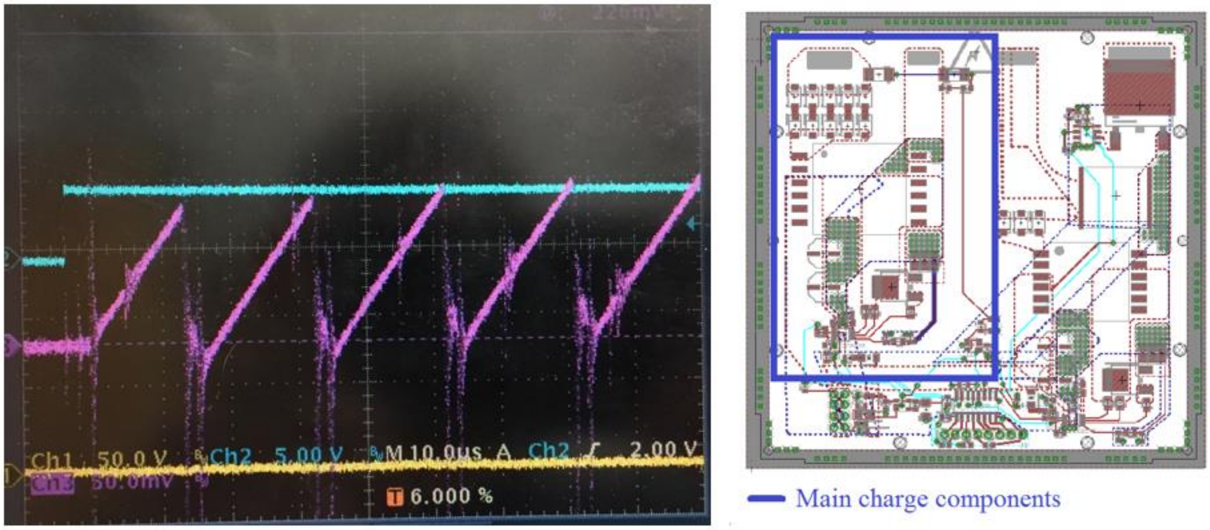

Figure 4-9 Sawtooth current waveform from LT3750 controlled MOSFET and charge board layout with highlighted main charge components

Table 4-5 shows power efficiency for when charging the main capacitors to different voltages. The input to the system is 6.6V. 1000 Volts was selected for reasonable charging power efficiency of ~77% while maintaining high voltage. The peak current is controlled by a selected resistor value as $I_{pk} = 78mV/R_{sense}$. Higher peak currents reduce the charge time.

Table 4-5 Power efficiencies of charging capacitors to 100-1030V using a 6.6V input

VO (V)	***Vin (V)***	***Ipk (A)***	***Iavg (A)***	***time (s)***	***Pin (W)***	***Pout (W)***	***efficiency***
100	6.6	9.3	4.65	0.0048	15.345	11.458	74.67%
200	6.6	9.3	4.65	0.0158	15.345	13.924	90.74%
300	6.6	9.3	4.65	0.0332	15.345	14.910	97.16%
400	6.6	9.3	4.65	0.058	15.345	15.172	98.88%
500	6.6	9.3	4.65	0.091	15.345	15.110	98.47%
600	6.6	9.3	4.65	0.134	15.345	14.776	96.29%
700	6.6	9.3	4.65	0.188	15.345	14.335	93.42%

800	6.6	9.3	4.65	0.262	15.345	13.435	87.55%
900	6.6	9.3	4.65	0.354	15.345	12.585	82.01%
1000	6.6	9.3	4.65	0.466	15.345	11.803	76.91%
1030	6.6	9.3	4.65	0.504	15.345	11.577	75.45%

In testing, the low resistance R_{sense} resistors proved the most problematic, and had to be replaced with a larger surface mount package to ensure they did not fail in an open circuit. The opto-isolator also created problems when powered from the main charge board but not from the microcontroller side. In some cases, the outputs on the charge board side of the isolator would float high. This was solved with 100 kΩ pull-down resistors on the output. When failures elsewhere caused operations outside of nominal bounds, the LT3750 was the component most likely to fail subsequently. The main charge system was tested to 100,000 pulses using the thunder-box setup with 20 Joules by using 4 of the 5 uF capacitors previously tested to work under the discharge conditions.

4.4 Designed Operations Plan

The propulsion system is designed with the goal of raising the orbit of a 3U CubeSat. Main requirements of such a CubeSat include batteries capable of sourcing high current around 9 Amps, solar panel charging on the order of 8W, and attitude determination and control (ADC) to allow for velocity vector pointing. In conjunction with HuskySat development, the PPT controls are based on information passed over a distributed controller area network (CAN) bus. The PPT microcontroller uses information from the ADC system and the power system.

4.4.1 CubeSat formfactor

Through utilization of a trade study for high energy density capacitors, minimization of charging electronics and the tuna-can extension permissible on some 3U CubeSats, the final design of the thruster was able to be structured in a CubeSat formfactor. Figure 4-10 shows the internal packaging and external dimensions of the thruster subsystem, which is 5.5 cm long, or approximately 0.55U. To fit within the volume budget of the HuskySat-1 CubeSat, the number of capacitors had to be reduced from 8 to 4. This reduced the energy from 20 J to 10 J and had implications on thruster performance discussed in section 4.4.2. The tuna can extension of 3.6 cm fits the electrodes and full 60g sulfur puck with room to spare.

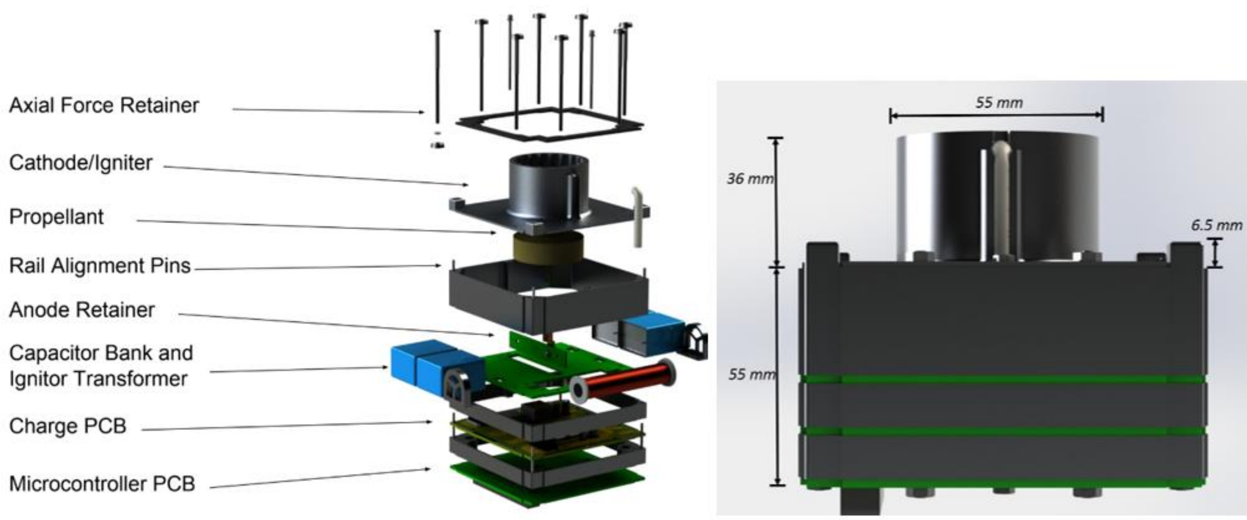

Figure 4-10 Exploded view and dimensions of CubeSat thruster

4.4.2 Final thrust results of CubeSat propulsion system

The specific thrust output of the final thruster was taken using the assembled PPT module with the computer board next to the assembly instead of flush, in order to access pins on -Z side. The aluminum structure, charge board, ignitor, capacitors, and electrodes were all assembled as if for flight. Differences between the thruster in flight and the tested setup included room temperature, an external power supply, and pressures in the 2E-5 Torr range, otherwise, the test setup reflected flight operation. In low earth orbit, the power is supplied by the adjacent battery pack, the temperatures on the satellite can fluctuate ~ -20 to 50 C, and pressures are below 10^{-8} Torr.

The specific thrust obtained from the curve fit of the data was found to be 25.0 mN/kW with a standard deviation of 2.25 mN/kW and a maximum difference from the mean of 22%. The measurement was taken over twenty pulses after an initialization of 20 pulses. An example trace from this test is shown in Figure 4-11. The fit from this trace, as described in Section 4.2.3, has an amplitude of 142.6 mV with a 95% confidence interval of the fit between 139.9 and 145.4 mV and an R^2 value of 0.81. R^2 values of each of the fits are above 0.77.

There is a ~20% shot to shot variability in PPT performance that has been observed but not quantified. However, the leading cause in uncertainty in the calculation of the value of specific thrust each pulse comes from the uncertainty of the magnetic inductive sensor calibration, which is 7%. Further work on this calibration could decrease uncertainty in the reported values.

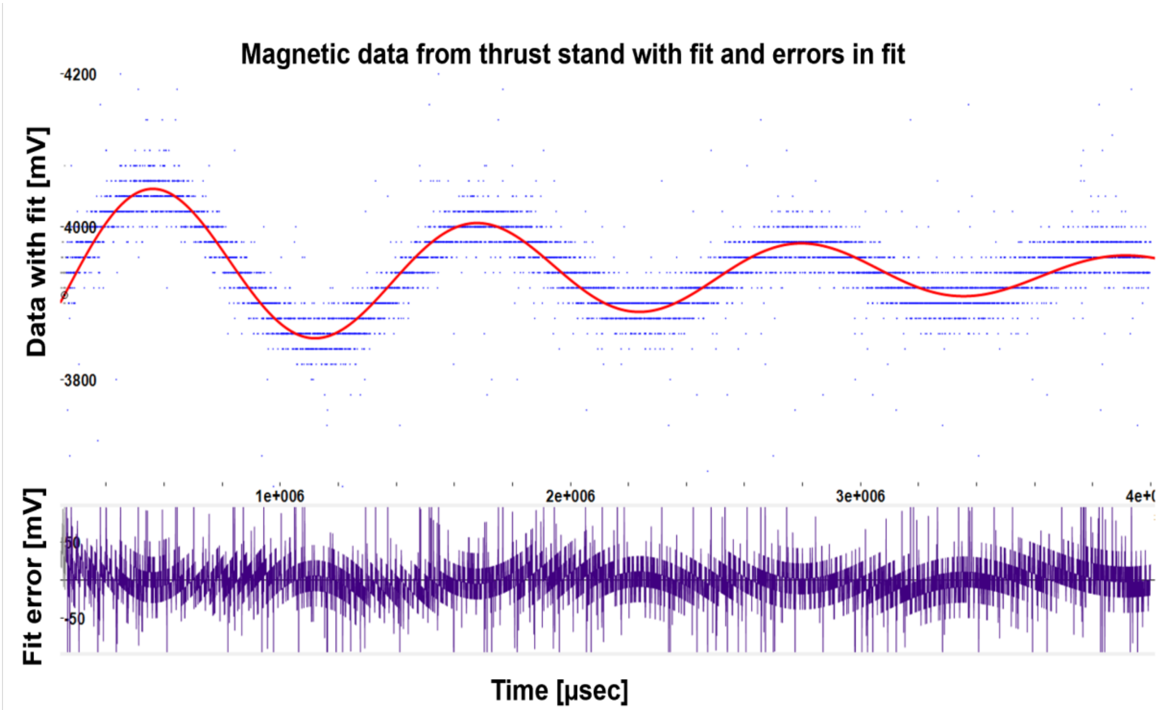

Figure 4-11 Example trace in blue from magnetic inductor during thrust stand testing with red line showing damped sine fit from Eqn 25 (top pannel). Purple data show the difference between the fit and individual data points (bottom pannel).

The lower specific thrust when compared to previous testing of the same geometry is a surprising result. Previously, minimizing wire lengths and numbers of connections, especially between the capacitors and electrodes, increased the specific thrust by decreasing impedance. Therefore, it was thought that the compact design would lead to an increase in performance. Using only 10 J of energy instead of 20 J brings the thruster into the lower slope of specific thrust energies tested in section 3.4.1 and is not the energy optimized for in the geometry testing of section 3.4.2. Instead, it is a tradeoff needed to manifest the thruster with the other subsystems that make up the HuskySat CubeSat. This difference in energy could account for about half of the change seen. This is estimated by the ~20% drop from 20J to 10J sulfur specific thrust testing in section 3.4.1

compared to the ~45% drop from 45.6 mN/kW at 20J for previous testing of the 17-point serrated cathode to the 10J flight model. Other possible factors are the change in brand of thin film capacitors or a suboptimal electrical connection in the limited space of the flight model causing increases in impedance to the circuit. The remainder of the difference would then need to be made up for in the alteration of the thrust measurement method.

Assuming an initial mass of 4 kg, the 60 grams of fuel could enable an absolute maximum Δv of 108 m/s for the CubeSat mission given these results.

4.4.3 Interaction with CubeSat

Figure 4-12 shows how the PPT microprocessor programming works within the bounds of satellite operation. When initiated, the system first performs several checks that would be required on a CubeSat aiming for a change in velocity:

- that the pointing is correct, so that thrust will result in orbit raising/lowering
- that the batteries are sufficiently charged for the planned operation
- that the satellite is not over the ground station, when communications take precedence
- that the faults experience by the system have not surpassed a preset limit, which requires manual override to avoid damaging the system by continuously misfiring.

Once all checks have cleared, the system follows a predetermined pulse frequency, which is no greater than ½ Hz and then fires the thruster at that frequency for a user defined duration. When faults occur, the fault counter is updated and compared to a user defined threshold. In this way, a single misfire will not immediately end the firing, but the thruster will not continuously attempt to fire when it is not operating properly.

Examples of faults are the main capacitors not reaching full charge in the time allotted, which could be attributed to increased temperatures on the satellite. Alternatively, the main may not discharge, indicating an issue with the ignitor system. The system is not capable of detecting faults such as those mentioned in Valdes and Khorasani, 2010, which accounts for differences in thrust. It can detect partial charging through the use of a Schmitt trigger on a voltage divider off the main charge line. The Schmitt trigger goes high at 700 V on the main and low at 300 V on the main, allowing for some diagnostic of the charging system without processing full charging and discharge data.

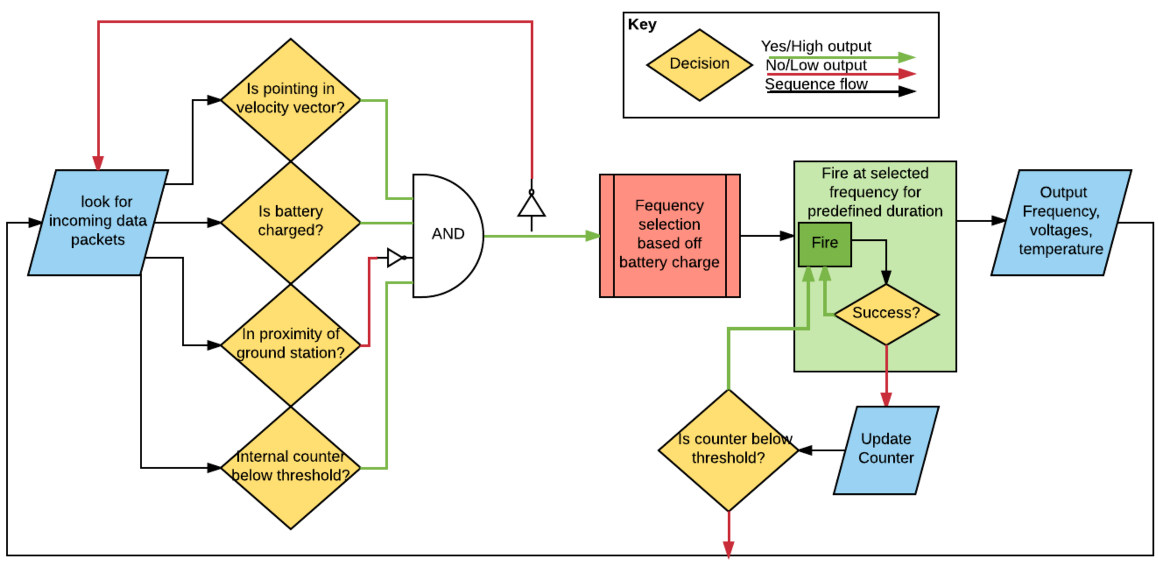

Figure 4-12 Functional diagram of PPT programming

At the conclusion of a firing sequence, the firing frequency, temperature range, and faults are reported and the process restarts. In this way, the thruster fires as frequently as possible in order to reach 500,000 pulses over a three-month time span. The firing occurs in a way that enables other systems, like communication and attitude control, to maintain operations without ground command.

In order to allow other systems to operate while the PPT is in a firing mode, the timing of the charge and firing is set as shown in Figure 4-13. The 'sync' with the other systems alerts them to the firing state of the PPT and gives a minimum 0.8 second window for sensitive systems or measurements to be made. Systems less sensitive to electromagnetic interference caused by the high current charging the main capacitors continue to operate during the PPT charge phase. Any highly sensitive systems shut down for the actual pulse of the thruster, as this is the time when both induced and radiated electromagnetic interference are highest.

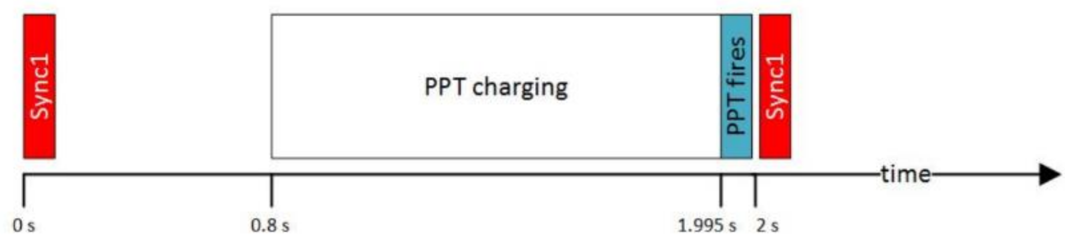

Figure 4-13 PPT Charging timing in relation to synchronization with other CubeSat systems

To reduce the electromagnetic interference to the remainder of the satellite, all high voltage and high current components of the pulsed plasma thruster are single point grounded to the batteries. This schematic for this is shown in Figure 4-14. Besides the CAN bus connection and the single point battery ground, the entire propulsion subsystem is electrically isolated from the remainder of the satellite. Within the PPT, ground loops are minimized, and the charge board is separated from the microprocessor board using an ADuM163N opto-isolator.

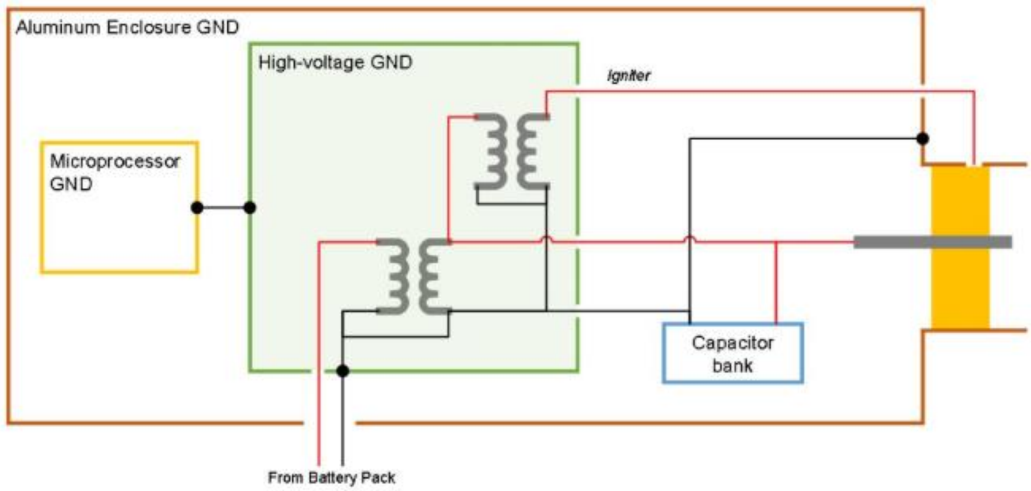

Figure 4-14 Grounding scheme for PPT subsystem

4.5 Conclusions

Taking the pulsed plasma thruster from a benchtop system tested for several hundred pulses to a complete package capable of hundreds of thousands of pulses without loss in performance required advancements in material selection, thorough testing of the lifetime of electrical components, and flight plans for the way in which the thruster operates in relation to the remainder of a satellite.

Main issues arising from the transition that had to be addressed included loss in performance from buildup on the cathode and a lack of rated capacitors with low volume. A change in cathode material overcame the issue of buildup. Testing allowed for the certification of underrated capacitors, but the realities of satellite volume budget tradeoffs resulted in a drop in the energy of the thruster subsystem through a reduction in the number of capacitors.

The constructed thruster package is component tested to a minimum of 100,000 pulses. Wear on electrodes is documented and a Tungsten anode and Al7075 cathode are selected. Analysis of the sulfur fuel puck indicates that the fuel forming process is acceptable with limited void space and outgassing properties. The thruster construction and operation are designed within the larger CubeSat operation to autonomously and safely provide thrust to a satellite. Finally, thrust measurements of the completed system give a maximum total Δv of over 100 m/s assuming 60g of fuel on a 4kg CubeSat.

Chapter 5. Pulsed Plasma Thruster Flight on HuskySat-1

The HuskySat-1 mission serves as technology demonstration of the flight pulsed plasma thruster. This chapter describes the implementation and performance of the pulsed plasma thruster on the HuskySat-1 satellite and its integration with the remainder of the satellite in preparation for the provided launch opportunity. This chapter also describes flight hardware acceptance testing and analysis needed to meet the launch provider's requirements. In-space thruster testing on board the satellite concludes the characterization of the pulsed plasma thruster for CubeSat missions. The propulsion unit on HuskySat-1 is a subsystem of the satellite. The full satellite design and build is a compilation of the work done by over 60 undergraduate and 5 graduate students over 4 years, in addition to partnerships with the Amateur Satellite Corporation (AMSAT) and Raisbeck Aviation High School. Further information on board layout and software can be found at https://github.com/UWCubeSat.

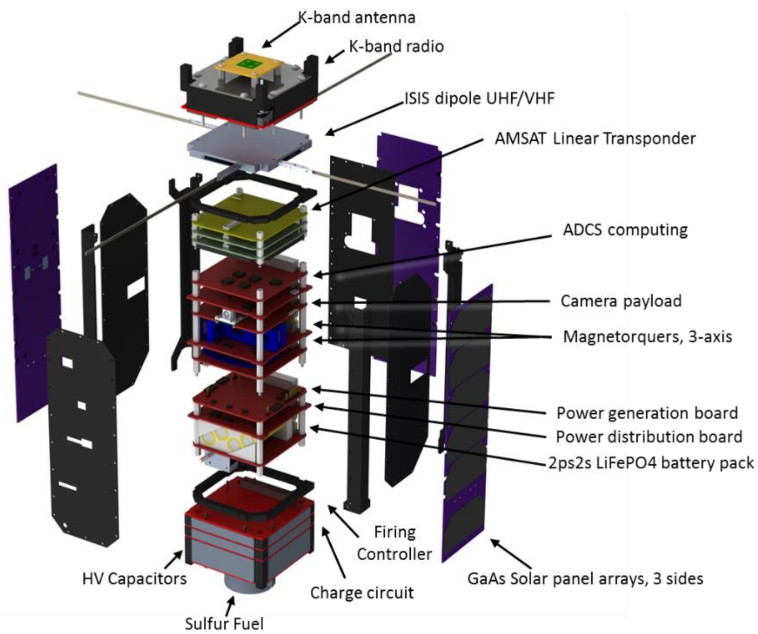

Figure 5-1 Exploded view of HuskySat-1

5.1 HuskySat-1 Introduction

5.1.1 High level mission description

The overall goals of the University of Washington HuskySat-1 mission are to demonstrate an experimental K-band downlink and a pulsed plasma propulsion system, which constitute important advances for CubeSat systems and a necessary step to implement the missions described in Chapter 2. A secondary goal is to receive transmissions of images taken by the onboard camera payload. The camera payload was developed in cooperation with local Raisbeck Aviation High School with assistance from non-profit Quick2Space. An additional aspect of the HuskySat program is that it was student-built, and therefore provided workforce development for students involved with the project.

The satellite was launched as an external secondary payload aboard the Northrup Grumman, or NG, -12 launch of the Cygnus ISS Resupply Capsule, from the Mid-Atlantic Regional Spaceport, on Nov 2nd, 2019. The Cygnus capsule remained at the ISS for approximately three months. When the Cygnus capsule departed from the ISS, it boosted to a circular orbit of 465 km, on an inclination from the equator of 51.6 degrees. HuskySat-1, along with SwampSat II from the University of Florida and Orbital Factory 2 from the University of Texas, El Paso were deployed from the Nanoracks external deployer. Deployment occurred at 22:30 UTC on January 31st, 2020.

UW operation of the satellite was planned to cease ~3 months after first transmission. At this time ownership of the satellite will be transferred to AMSAT to repurpose it for Amateur operation. At the time of transfer, the propulsion system, the K-band communication system, and the camera payload will be disabled.

Upon successful transfer and verification of control, AMSAT will activate the amateur satellite service two-way linear transponder communications for amateur radio operator access worldwide. The amateur radio is a 30 kHz wide transponder with uplink in the two-meter amateur satellite band and downlink in the 70cm amateur satellite band. Transponder health and operation data as well as satellite health data that is necessary for proper operation of the amateur radio package will be downlinked in the transponder beacon in order to facilitate proper operation by AMSAT. AMSAT expects the transponder to be active for the lifetime of the satellite orbit.

Atmospheric friction is expected to slow the satellite and reduce the altitude of the orbit, until de-orbiting occurs about 3.2 years after deployment. The spacecraft is a single unit with the dimensions of 3 stacked ~10 x 10 x10 cm CubeSat modules with a “tuna can” extension on one end, giving an overall dimension of 10 cm X 10 cm X 34 cm with an extension reaching 37 cm.

The total mass is about 3.14 kg. Dimensioned drawings of the final model done in Solidworks are shown for the ±y and ±z faces in Figure 5-2.

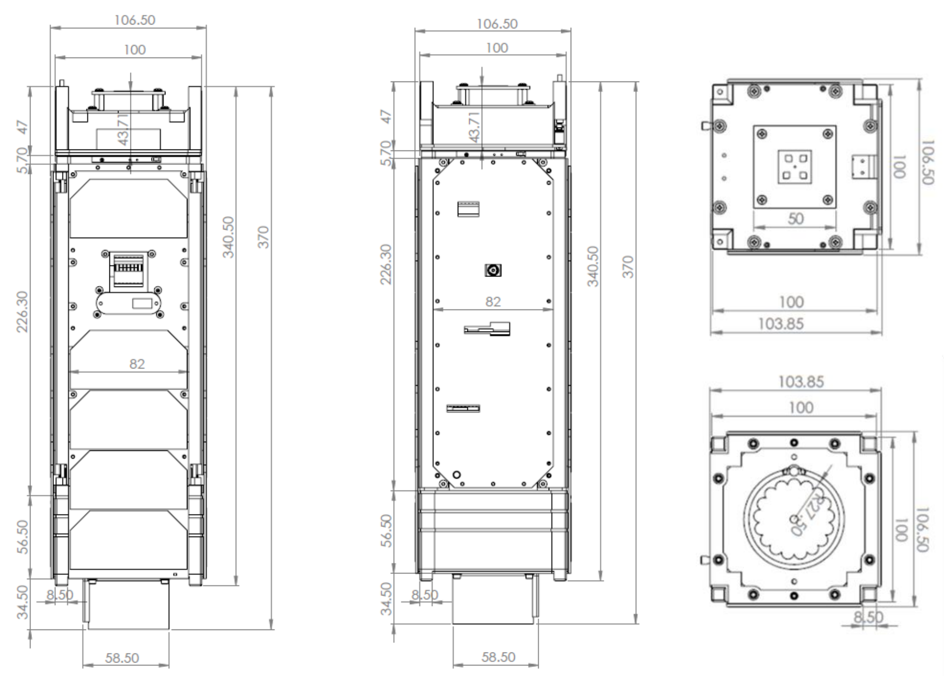

Figure 5-2 Dimensions and external view of HuskySat-1

5.1.2 HuskySat Systems Overview

The subsystems that make up HuskySat are described below. The physical location of each subsystem on the satellite is shown in Figure 5-3.

Attitude and Determination and Control Subsystem (ADCS): The ADCS system determines tumble rate and orientation using an IMU (ST LSM6DSM), three magnetometers (Honeywell HMC 5983), and a sun sensor (nanoSSOC D60). The orientation can be altered through the use of in-house designed and built 3-axis magnetorquers.

Command and Data Handling (CDH) Subsystem: Command and data handling on the HuskySat is distributed across multiple MSP430 microprocessors and utilizes a CAN bus to pass information between each subsystem.

Electrical Power Subsystem (EPS): The EPS is comprised of 3 side panels with Azur Space GmbH 3G30A photovoltaic cells going to a power generation board which controls charging, balancing, and heating the 6.6V 2.2 A-hr battery system. The batteries are COTS A123 APR18650m1B cells in a 2s2p configuration. From the battery pack, a power distribution board with over-current protection switches power to individual subsystems.

UHF/VHF Communication Subsystem (COM1): The comms transceiver will support a VHF uplink, and UHF downlink, using an ISIS 2-dipole antenna. It communicates with the ground station on the UW campus.

Structure Subsystem: The structure is fabricated from 7000 aluminum with stainless steel fasteners.

Propulsion Subsystem Payload (PROP): The propulsion system is a pulsed plasma thruster (PPT) utilizing a solid sulfur fuel. Each pulse has an energy of 10 J, and it can fire at maximum frequency of once per 4 seconds. The system will only engage by direct command from the ground station and fire a single pulse in response to each command. Each pulse provides an approximate impulse on the order of 500 μNsec, providing a delta V of about <0.00016

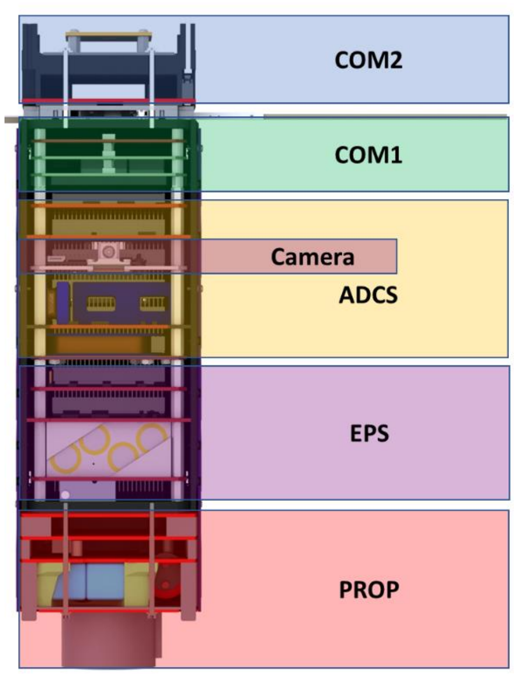

Figure 5-3 HuskySat subsystems overview

m/s, per pulse. The maximum possible total number of pulses over a 3-month period would be less than 1000, likely much less. The total delta V imparted, if all 1000 pulses had the maximum cumulative effect, would be less than 0.2 m/s.

K-band Communication System Payload (COM2): The experimental communication system operates at 24 GHz for downlink only with a patch array antenna. It transmits to the receive only ground station at the UW campus.

Camera Payload: Raisbeck Aviation High School student interns designed and built a camera payload that is flying on HuskySat-1. The camera is a Raspberry Pi Camera Module v2. On-board processing will capture an image and compress it to a 92x64 pixel greyscale image, with a ~550km swath width, which is then downlinked on the COM1 system.

5.1.3 HuskySat-1 capabilities

This section is a breakdown of proposed and realized capabilities of HuskySat-1. Failures in environmental testing of the reaction wheels and planned deployment of the solar panels drove mission redesign.

5.1.3.1 Changes to Mission Objective

The objectives of the mission were changed from the original to the revised as denoted below. This change exhibits the extent of the descope outlined in the following section, and considerably lowers the extent to which the PPT will be tested. However, the PPT was still delivered as a flight unit capable of 100 m/s Δv.

Proposed Primary Objectives:

- Delivery of system by August 2017

- 3 months of operation
- Operational PPT with measurable ΔV
- Downlink of 100Kb using high frequency K-band antenna

With proposed Secondary Objectives:

- 3-6 months of operation
- Measure 100 m/s ΔV
- 100Mb downlink from a reflectarray antenna
- Flight of electronics payload from local High School
- Establish ground station with high frequency capabilities

Revised HuskySat-1 Mission Objectives:

- Downlink predetermined sequence from K-band antenna
- Demonstrate successful discharge of PPT on orbit
- Downlink image from local high school camera payload

5.1.3.2 Changes to Satellite Design

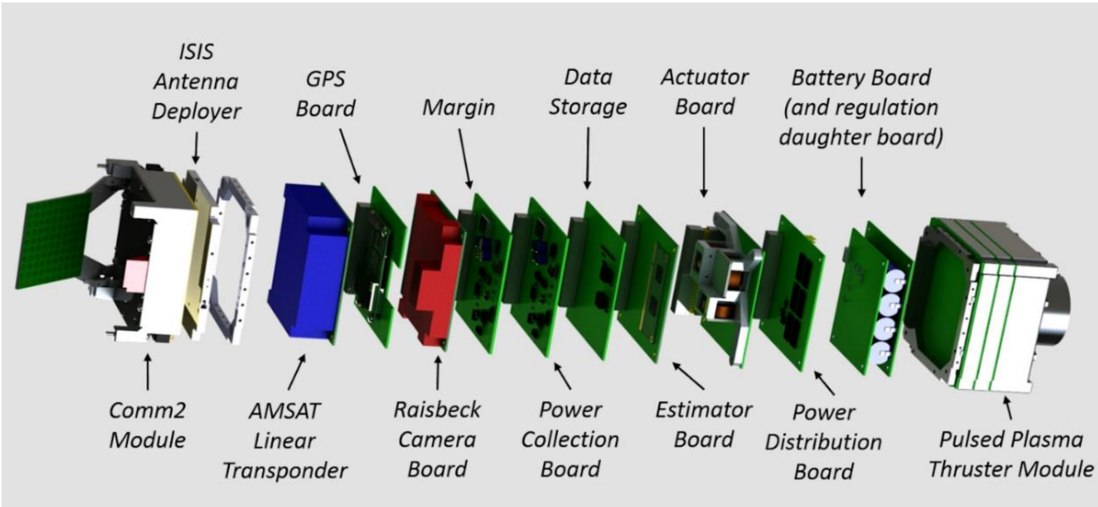

The changes to the physical design are driven mainly by failures encountered during environmental testing. Specifically, the hinges on the deployable solar panels seized during initial vibration testing and failed to deploy at the conclusion of the test. Further, after vibration and thermal testing, only one of three identical reaction wheels operated properly. Given the schedule, these two features failed to make the cut instead of going through a re-design.

The combined loss of the deployable solar panels and reaction wheel pointing resulted in a cascade of changes to the physical design and operational plans for the satellite.

Figure 5-4 Original HuskySat systems breakdown, including reflectarray antenna and 3-axis reaction wheels

The original design in Figure 5-4 also included a GPS board using a Novatel OEM719 unlocked for operation in space. The interface of the Novatel package with the HuskySat bus proved to be more difficult than expected. The difficulty of integration and the reduced need for GPS due to the planned descope of the propulsion goals to negligible ΔV led to the decision to cut the GPS from the mission.

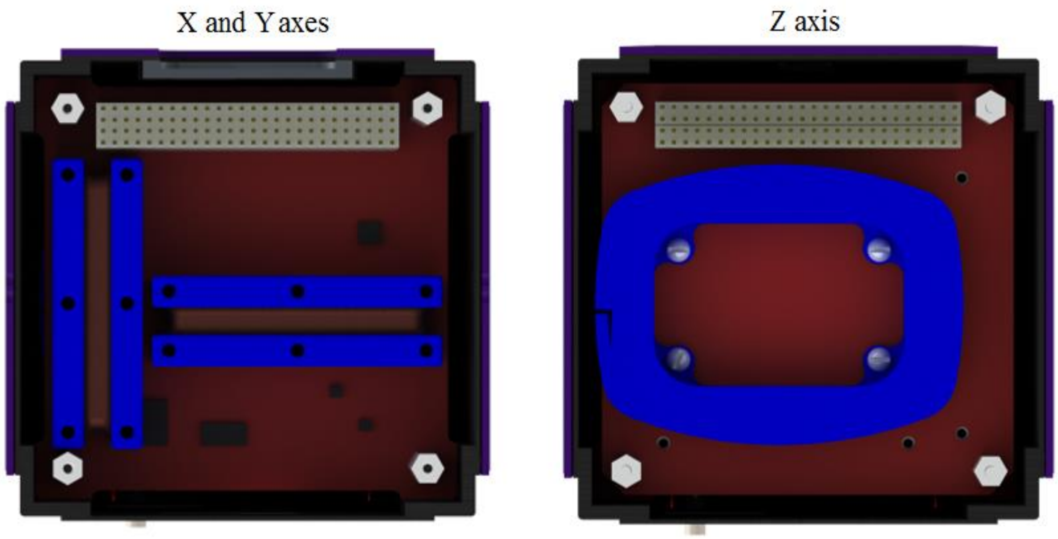

Figure 5-5 Magnetorquer windings on blue bobbins for applying magnetic moments in the X, Y and Z axes on the CubeSat

5.1.3.3 Attitude control capability

Without the reaction wheels, the satellite has a reduced ability to point with precision and speed. The magnetorquers are aligned with the x, y, and z axes as pictured in Figure 5-5 and are air core electromagnets with ~300 windings of 26 gauge wire per axis with a magnetic dipole moment, $\mu = I * A$ where I is current and A is area enclosed in the loop, of 0.03Am^2. They can be used to detumble the satellite or to provide spin by torquing against the Earth's magnetic field. High tumble rates decrease the satellite's ability to decode commands from ground and blurr any images taken. Very low tumble rates could put the satellite in a position where the solar panels on

3 sides receive very little sunlight on an average orbit. Thus, the ability to detumble and add spin are both important. The on-board B-dot algorithm driving the current to the magnetorquers can change the spin rate of the satellite on the order of 2 degrees per second in 1 minute.

With a desire to have some spin on the satellite, the propulsion system will not impart thrust only in the ram direction. The net thrust, if fired at random times, should be zero. In the Huskysat flight configuration, no Δv is expected, even when fired at the maximum amount described in section 5.3.3.2.

5.1.3.4 Available power

The proposed concept of the satellite operations had the satellite pointing towards the velocity vector with the secondary vector pointing the single solar panel plane towards the sun. This provided an orbit-average power to meet a 12 W requirement. With solar panels on three sides, as opposed to a single plane with three sides worth of solar panels, the orbit-average panel power is around 3.25W. The COM1 system set to a -16dB gain pulls an average .28 amps at 6.6 V, for a power draw of ~2W. This system is on continuously during normal operations, so the on orbit average power is down to 1.2 W to avoid depleting the batteries.

The pulsed plasma thruster, when enabled, pulls a steady state 0.45W. This leaves around 0.75W of orbit average power. When firing, the PPT pulls a peak 45 W with an approximate average of 15W for 1.2 seconds. With a 95 min orbit, this averages to ~4mW per orbit per pulse. Thus, even with other systems enabled, the pulsed plasma thruster can fire while over the ground station knowing the batteries will reach full charge within an orbit.

It is also acceptable to run a deficit of orbit average power for a given orbit, provided the deficit is not large and not continued for multiple orbits. If the battery voltage falls below 6.5V, undervoltage protection on the satellite will revert the satellite into a low current mode.

5.2 FLIGHT QUALIFICATIONS

5.2.1 Thermal testing

The thermal environment in space is stressful to electronic components because of the frequent large changes in temperature as the satellite moves between direct sunlight and eclipse. In a low-Earth orbit, this occurs around every 90 minutes. The low thermal mass and minimal thermal control of HuskySat when compared to larger traditional satellites increases the possible temperature swings on individual components.

5.2.1.1 Setup

The setup for thermal testing comprises a thermal chamber at atmospheric pressure with thermal control. Foam insulated feedthroughs for wires allow for monitoring performance while the thermal test is ongoing. The plasma thruster electronics, shown in Figure 5-6, are distributed

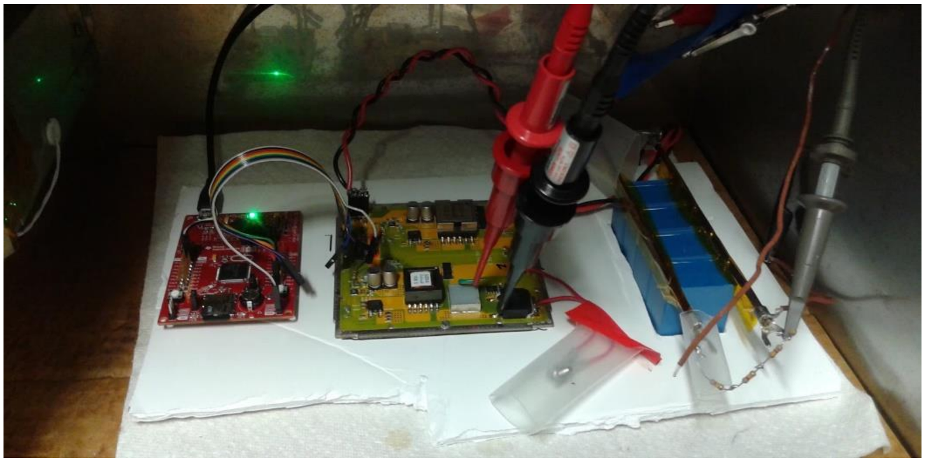

Figure 5-6 Thermal testing setup with probes in place

separately, as the temperature test relies on convection to heat and cool the components. The MSP430 microcontroller on the programable test board stands in for the PPT computer board, which uses the same microprocessor. A high voltage probe is used to measure the ignition charge and discharge, where the discharge is shorted without going through a step-up transformer to avoid sparking. A 10x voltage probe measures the voltage on the main capacitor bank through a 1:5 voltage divider.

Questions being addressed for this test:

1. Does the board continue functioning over the +75C to -20C temperature range?

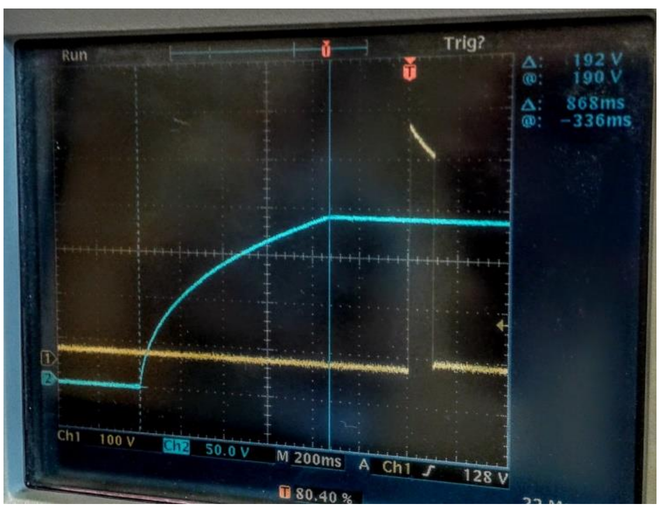

2. How does charging time change with temperature?

3. Is the timing changed by temperature cycling +75C to -40C, indicating deterioration?

Figure 5-7 shows and example scope trace used for confirmation of the ignitor discharge and the shape of the main charge curve. Main charge times were recorded from the output of the microprocessor.

5.2.1.2 Results

Results from the testing lead to the following answers

1. The charge board does function within the entire +75C to -20C temperature range
2. The charging time of the main capacitors increases with temperature up to 1.20 seconds within the operating temperature range. Default timing is 1 second.
3. The timing of the charging is consistent before and after a thermal cycle of -40 to 75 C.

Table 5-1 Thermal testing results

Figure 5-7 Example probe output from the main capacitor charge (blue) and the igniter charge and discharge (yellow)

Temperature (^{o}C)	**Time to fully charge main (ms)**	**Full charge reached on main**	**Full charge reached on ignitor**	**Ignitor discharge**
23	878	Yes	Yes	Yes

75	1200	Yes	Yes	Yes
-20	778	Yes	Yes	Yes
-40	NA	NA	NA	NA
23	880	Yes	Yes	Yes

The charge time can be set manually from the ground. If the main does not reach full charge, the "main charge time" will not update, and the timing can be extended.

5.2.2 Vibration testing

To ensure survival of the satellite through the vibration conditions on launch, flight hardware must pass vibration testing. The level of testing is dependent on the launch vehicle and provider. The NASA General Environmental Verification Standard (GSFC-STD-7000 [Standard]) is a common baseline for vibration requirements [Weston]. Qualification testing of non-flight hardware is usually required or recommended to a higher level than the flight model acceptance testing by 3dB for random vibration tests. Exact profiles required for specific launch and deployment configurations vary widely and fall under Export Administration Regulations.

Several tests are needed for the propulsion system to reach qualification and acceptance. With failure in the first two tests, the third test was a low-cost trial to assess the changes made, the fourth test qualified the PPT, and the fifth and final test was conducted for acceptance of the flight model.

Each of the tests were conducted at a different facility with a different setup and are described in the sections below.

5.2.2.1 Initial vibration testing of Satellite components

The initial two vibration tests occurred on the satellite components in a deployer housing. These tests used early models of the propulsion system, which contained only main components that were not all properly affixed. The PPT assembly did not survive this vibration testing, with several modes of failure observed.

Table 5-2 and Table 5-3 outline the failures seen during the first two vibration tests.

Table 5-2 Vibration test results 1

Failure	Modification	Image
The bolts holding the PPT to the HuskySat chassis were loosened. Originally torqued to 80 in-oz, all eight 4-40x2.5" screws were found to be between 50-60 in-oz after vibe. The two 4-40x2" bolts internally fastening the PPT together successfully maintained their torque levels, however. The two 2-56 screws fastening the anode retainer to the cathode plate were loosened completely and one of the nuts was missing entirely.	Future designs may replace the flathead 4-40s with panheads for better surface friction. Additionally, the 2-56 screws require locking washers. All screws may be epoxied after integration in the final configuration.	
The sulfur puck exhibited some disintegration, particularly around the circumference where it was joined with the 3D-printed mold. Sulfur powder was found deposited on many of the boards and chassis components. The disintegration was likely the result of the flexible mold undergoing oscillatory deformation during vibe.	The PETG mold will not be included in future iterations	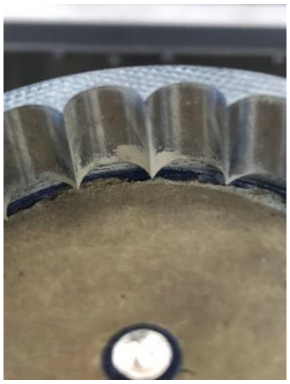 *Figure 5-8 Sulfur failure*
The main capacitors did not stay fully affixed to the capacitor PCB. One of the capacitors came loose entirely while two more became partially detached from the epoxy.	The capacitors will be sanded to improve epoxy adhesion. The PCB itself will not have the truss structure under the capacitors, as they provide higher opportunity for board flexing that breaks the epoxy bond.	

Various other small components experienced failures as a result of vibe testing.	These vibration sensitive components will be affixed with 3M epoxy	

Table 5-3 Vibration test results 2

Failure	**Modification**	**Image**
Sulfur mass loss of 1.65 g due to obvious erosion around edges of both surfaces	The sulfur puck will be epoxied to inside wall of cathode housing to prevent shaking and rotation.	 *Figure 5-9 Second sulfur failure*
High-profile capacitors broke at connection point to surface mount pads	Pot the base with epoxy to relieve stress on weak connection point	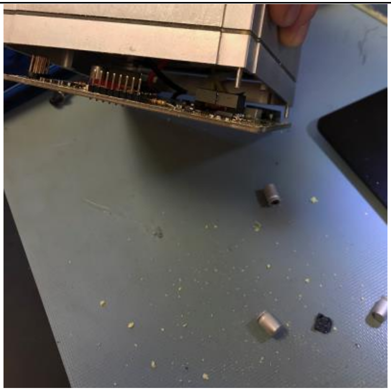 *Figure 5-10 Capacitor failure*

The second test was a fully function system. It included wired charging electronics. Pre- and post-vibration test results using the electronics were consistent (after replacement of the high-profile capacitors) indicating that only the two reported failures need to be addressed. Slight wear was observed on the end of the rails but was determined to be acceptable.

5.2.2.2 Plasma thruster qualification vibration

Having failed original testing, a final qualification test on the propulsion system was tested at the Sigma Design facility in Camas, WA. In this configuration, the propulsion unit was affixed to the connector that holds it the main satellite, which was affixed to the mounting plate, held on to the vibration table with 6 bolts. Two test stacks of batteries underwent testing at the same time, and the random vibration profile encompassed the requirements for both. The plasma thruster was inspected visually with no observed degradation of the sulfur, as show in Figure 5-11.

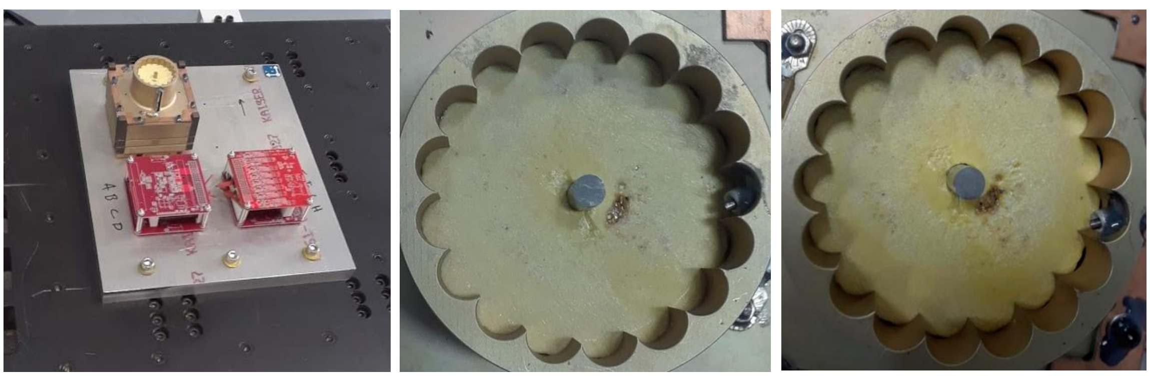

Figure 5-11 Flight qualification test of pulsed plasma thruster: mounting (left), pre-vibration (center), and post-vibration (right)

The acceleration across the frequencies pre and post sine sweeps were compared for each axis in Figure 5-12. While the magnitude of peaks shifted slightly, the location of the peaks remained the same with a maximum shift of 0.01%.

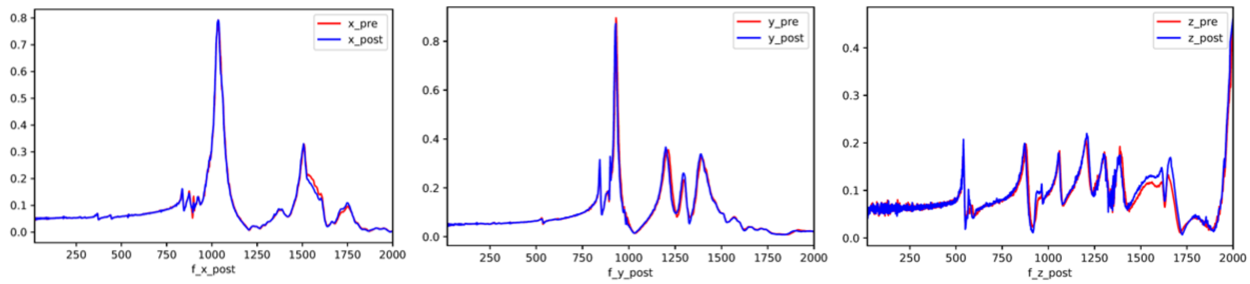

Figure 5-12 Vibration sine sweep comparisons of peak frequency locations for each axis

5.2.2.3 Flight acceptance vibration

The flight acceptance vibration test was conducted at Cascade Engineering with the fully assembled flight satellite in a flight model deployer supplied by Nanoracks pictured in Figure 5-14. The X, Y and Z axis were each tested to the same random vibration profile requiring and overall acceleration of 8.45 G_{rms} for 60 seconds with an acceleration spectral density of 0.05 $\frac{g^2}{Hz}$. This profile is shown in Figure 5-13 along with the output of the y-axis test. The blue trace is the output of the control accelerometer mounted to the vibration plate (seen in the yellow circle in Figure 5-14), while the pink line is the y-axis output of the accelerometer mounted to the top corner of the Nanoracks test fixture. The test fixture experienced rms acceleration up to 18.7 G_{rms}.

Between each axis, the deployer was tilted in all directions to test for any obvious rattling from parts that may have come lose. At the conclusion of the vibration, the satellite was inspected for visible wear and loosening of screws and was again tilted in all directions to ensure there were no loose internal components, as required by the launch provider. Prior to and after the vibration test, subsystem check-out tests were run to ensure that the vibration test caused no functional damage to the satellite. The plasma thruster was turned on and charged successfully, with charge time within normal bounds. It was not fired, as the testing was not conducted in vacuum.

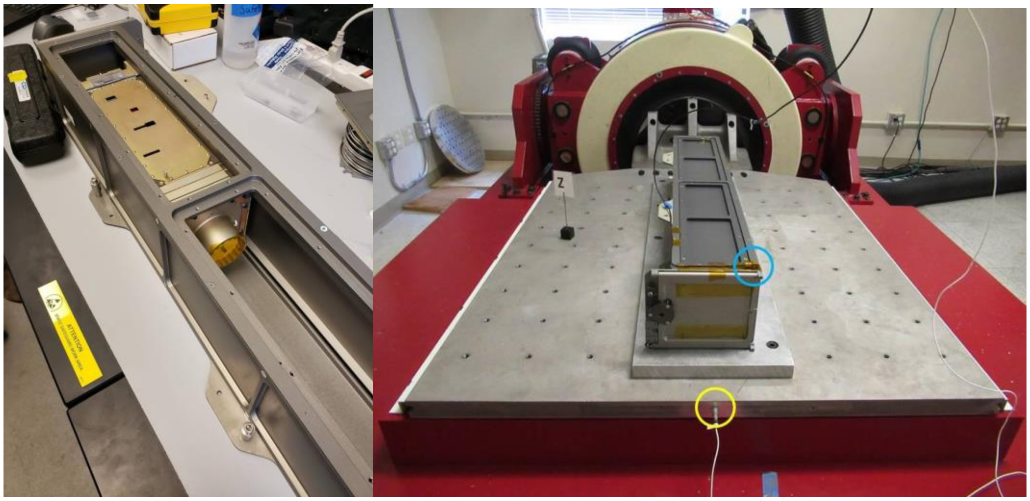

Figure 5-14 CubeSat in Nanoracks test fixture (left) and test fixture mounted for z axis vibration, with control and test accelerometers circled in yellow and blue, respectively (right)

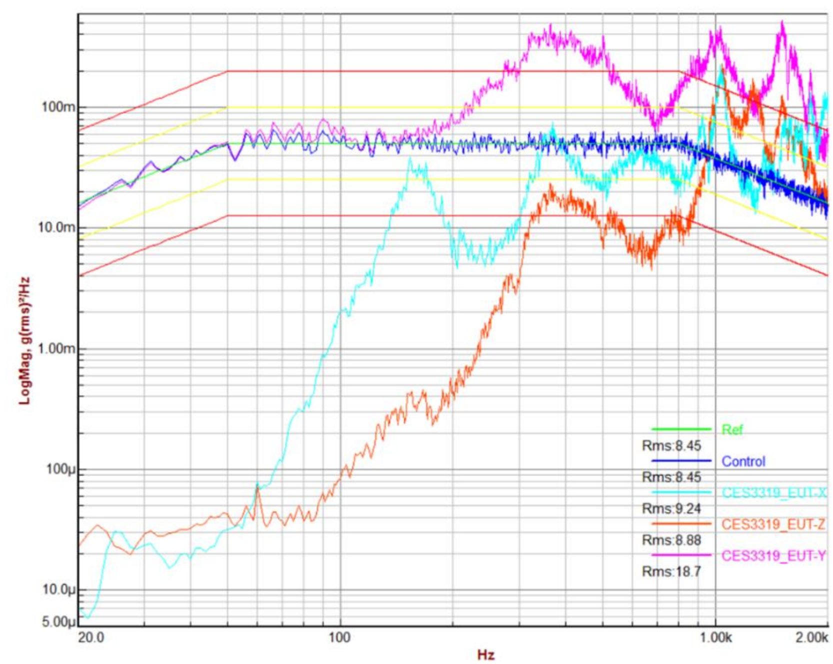

Figure 5-13 Output from y-axis vibration test

5.3 Propulsion Safety Analysis

Any propulsive satellite is subject to increased scrutiny to ensure that it will do no harm. This includes possible faults leading to issues on the way to space or in space, possible difficulty tracking the satellite when doing conjunction assessments with other satellites, and the possibility of a satellite being taken over from the licensed operator and used to do harm. Communication encryption, multiple inhibit safety features, and an analysis of worst-case scenarios are needed for approval of a propulsive satellite.

5.3.1 Communication Uplink Security

The communication uplink must be protected to ensure only the licensed operation of the propulsion system occurs. The physical security of room, passwords required to access commands, and the security of the satellite commands all play a role in uplink security.

The command center access limitations are the first line of security. It occupies a room in Johnson Hall on the University of Washington Campus on a floor that has controlled access after 6:30pm and on weekends. The door to the room itself is locked or supervised at all times.

The ability to generate commands from the command center is another form of security. The AMSAT provided FOXCOM package requires a password protected encrypted authentication file for each user that enables that user access to certain commands for a given length of time. Only the authentication files for lead operators will have propulsion commands enabled.

Finally, it is necessary that the satellite is not vulnerable to commands from other ground stations. Information arriving at the satellite must go through the reverse process from the ground: received data is de-interleaved, de-whitened, error corrected as necessary. If the decrypted signature matches and the command arrives within the time window specified in the command string, the command portion is acted on by the satellite. Otherwise the command is discarded.

5.3.2 Inhibits

Several inhibits are in place which limit the possibility of failures causing the thruster to fire. Many are built-in to the thruster hardware and are discussed in Chapter 4. However, the descope of the mission has led to the following addition inhibits.

Commands from ground are received by the COM1 unit which relays the commands to the satellite CAN Bus, as in Figure 5-15. The power distribution board must receive a CAN message to power-on individual subsystems, at which point those subsystems can receive messages from the CAN Bus. Any messages for a subsystem that arrive while the subsystem is off go unheeded. In this way, two correct commands from ground must be received, first to the distribution board to power-on the propulsion system, then to the propulsion system to fire. If the propulsion system is already on, only one additional command is needed to pulse the thruster one additional time. The initial design for the thruster was to run in a state machine that allowed for multiple pulses per ground command, but that feature is not enabled for the HuskySat flight.

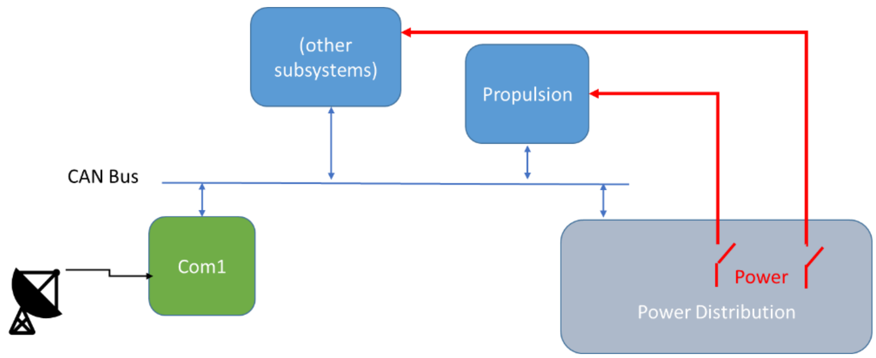

Figure 5-15 Schematic of power distribution board as a propulsion inhibit

5.3.3 Operational scenario analysis

An analysis of maximum possible changes in velocity from planned operation and a worst-case scenario are considered for safety of ISS and crew as well as for conjunction assessments made by Space Track.

5.3.3.1 Worst Case Failure for maximum change in velocity

The wort case scenario for a failure resulting in a large acceleration is a continuous firing of the PPT and is limited by the available power on the satellite. The following analysis assumes a failure of the undervoltage protection and a failure of the PPT microprocessor into a continuous firing state.

Power Budget Analysis Results

The batteries have a capacity of 14.5 Whr when fully charged. Using estimates which err on the side of a high ΔV, the PPT capacitors store 10J and have a charging efficiency of ~80%, requiring 12.5J just to charge the main capacitors, and ignoring the smaller draws from the microprocessor and the ignitor system.

$14.5[\text{Whr}] * 3600\left[\frac{\text{Whr}}{\text{J}}\right] \;/\; 12.5\left[\frac{\text{J}}{\text{pulse}}\right] = 4176$ pulses of the PPT given the energy in the batteries.

If the system timing was functioning properly, pulsing at ½ Hz, this would take at least 2.3 hours operating at an average of 6.25W, if not, it could take as little as half that time.

Taking the ~$500 * 10^{-6}$ $[Ns]$ impulse bit and the ~ 3kg mass of the satellite, we have a maximum ΔV of 0.7m/s.

Worst Case Failure Scenario Assumptions

1) No power draw from other systems: Com1 and battery distribution are required to be on for the propulsion system. The draws of these required systems are ~0.09W
2) No power draw from Prop microprocessor, voltage regulators, or ignitor system: these power draws are around an average 100 mW
3) No solar cell charging: charging rates average 2.4W over an orbit, which could increase the number of pulses, and thus the ΔV, by a factor of ~1.6.
4) Perfect pointing: the lack of pointing could completely negate any chance of delta-V in the event of even firings over a full tumble. Even with some pointing control, or intentional firing when within a desired orientation (not something the satellite is designed to do), the possible change in velocity reasonably drops by 30% or more.

Even in a worst-case failure scenario where the satellite has not drained any of its battery after a ~4 month quiescent waiting state, the satellite could produce a maximum of 0.7m/s ΔV.

5.3.3.2 Maximum changes in velocity from planned operation

The propulsion system on HuskySat-1 requires a ground command to pulse. As such, it can only be pulsed once every 4 seconds while in contact with the HuskySat ground station in Seattle. The NASA General Mission Analysis Tool software was used with ground station and orbit parameter inputs to determine that the satellite has contact with the ground station ~5 out of every 14 orbits for ~ 6 minutes each pass. The satellite is in line of sight for closer to 11 min, but communication at low elevation angles is uncertain.

Assumptions:

The thruster has a window of about 10 weeks of operation, over which a maximum of 1000 pulses total may be tested. In one day, no more than 20 pulses will be fired, with a maximum of 100 pulses per week. The initial planned testing is less than 20 pulses per week.

To maximize possible calculated effect on the orbit, it is assumed that all thrust will be in the RAM direction. This will not be the case on-orbit.

Summary of Calculated Values:

- The maximum total delta-V from the thruster over 10 weeks is 0.15 m/s.
- The maximum total delta-V from one day of operation is .0031 m/s.
    - This could occur in a single orbit, for which the drag contribution is ~0.00033 m/s
    - The drag contribution in a single day is ~0.0051 m/s
- The upper end of planned operations delta-V over 10 weeks is 0.091 m/s.
- The delta-V from drag over the 10 weeks is approximately -0.36 m/s.

A very conservative estimate of drag was used considering low solar activity to give an estimate on the drag force of 1.88E-7 Newtons over this time, the total delta-V over 10 weeks including the drag force is given below for each situation, and at no time do we overcome the average drag force for that 10 week period.

The satellite has an estimated lifetime of about 3.5 years (about 180 weeks) when discounting propulsion effects. The total effect of the propulsion over 10 weeks is less than half of the ΔV from drag for those same 10 weeks. Thus, the effect of propulsion on the demise date is within the uncertainty range of the lifetime estimate.

The expected case, as compared to the worst case, is that the delta-V from the propulsion will be in random directions, and to a great extent cancel itself out.

Notes on calculation:

Circular Orbit at 500 km:

- v = 7.6126 km/s
- Force of drag = 0.188 μN
- Period: 5677 sec = 96.133 min $\approx$1.6 hours
- 24 hr / 1.6 hr $\approx$ 15 orbits/day
- 15 orbits/day * 7 days/week = 105 Orbits/Week
- 105*(5/14) = 37 Seattle Passes per week
- 100/37=2.7 maximum average pulses per pass, used for calculation below

Table 5-4 Scenarios with possible changes in velocity from planned operations

Estimate: 2.7 pulses on every 3rd orbit		
v_Final (No Drag) = 7.61283 km/s	dv = 0.15 m/s increase	961 Pulses
v_Final (w/Drag) = 7.61247 km/s	dv = 0.21 m/s decrease	
Firing One Initial Burst of 20 Pulses		
v_Final (No Drag) = 7.6126829 km/s	dv = 0.0031 m/s increase	20 Pulses
v_Final (W/Drag) = 7.6123274 km/s	dv = 0.35 m/s decrease	
Firing 20 Pulses per week (modeled as a 20-pulse pass once every 37 orbits)		
v_Final (No Drag) = 7.6127709 km/s	dv = 0.091 m/s increase	580 Pulses
v_Final (w/Drag) = 7.61241489 km/s	dv = 0.26 m/s decrease	
Not Firing		
v_Final (w/ Drag) = 7.61232427 km/s	dv = 0.36 m/s decrease	0 pulses

5.4 Radiation Hazard Assessment

For the safety of the ISS, the ISS crew, and the Cygnus capsule, it is important to ascertain that a failure of the propulsion system could not result in dangerous ionizing radiation. The HuskySat satellite includes a pulsed plasma thruster which operates by a 10J discharge between electrodes initially at a 1kV potential difference. This discharge across the solid sulfur surface ablates and ionizes tens of µgs of sulfur per pulse, with the ejected plasma providing thrust to the satellite.

This is a possible source of both electrons and photons as ionizing radiation, though the energies of these particles are on the low end of possible ionizing radiation and are insufficient to penetrate the thinnest layer of the deployer box, which is 1.5mm. Thus, they cause no potential threat to the Cygnus capsule, even in the event of the failure of all inhibits which prevent the operation of the thruster prior to deployment.

5.4.1 Ionizing radiation: electrons

The source of high energy electrons is the initial breakdown in which electrons are accelerated through the full 1kV potential, giving them an energy of 1000eV. These electrons remain within the thruster, but were they to be directed outward, the inelastic mean free path of 1keV electrons through aluminum is ~2nm [Tanuma]. The neutral plasma that exits the thruster is of much lower energy.

5.4.2 Ionizing radiation: photons

Photons over 10 or 33eV are considered ionizing. The recombination of electrons with sulfur ions could possibly result in photons in the low end of what is considered ionizing, but photons in this energy range have an attenuation length of less than 1 microns in aluminum [Henke]

Some concern has been raised about high voltage electrodes in vacuum emitting x-rays, but this has only been demonstrated at voltages of 20 kV and above [West].

5.5 INTEGRATION, LAUNCH, AND DEPLOYMENT

HuskySat was integrated into the Nanoracks external Cygnus deployer in Houston, TX on Sept 16th, 2019, which was then shipped to Wallops Flight Facility in Virginia and integrated onto the outside of the Cygnus capsule. Figure 5-16 shows the stages of integration and the Nanoracks deployer.

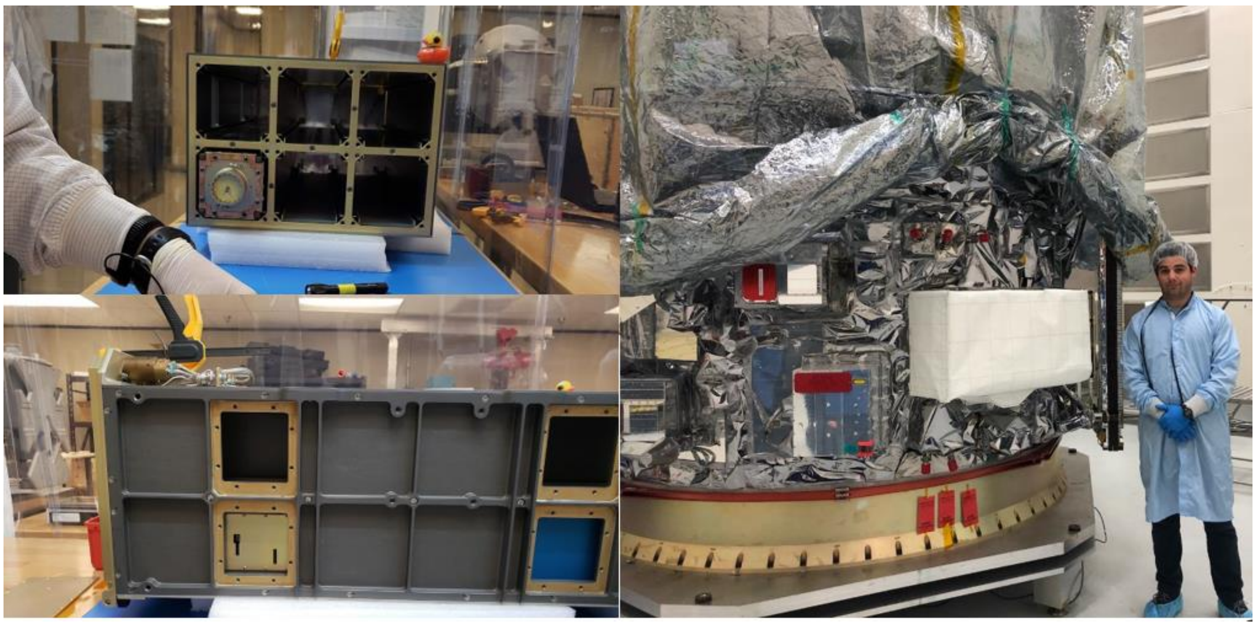

Figure 5-16 HuskySat integration: HuskySat in silo (upper left), HuskySat secured at front of silo of door 2 (lower left), Nanoracks deployer from left installed on Cygnus capsule and wrapped in thermal blanket

HuskySat passed all final checks conducted immediately prior to integration:

1. Depress switch on rail and hold: no noise should result check
2. Remove RBF pin: no noise should result check
3. Allow switch on rail to spring back check
    a. Beeping should result
    b. A red light should be visible on the right of the lower opening

4. Return RBF pin in less than 30 min to reset timer ~10 sec
5. Inspect sulfur dust on Kapton check, Figure 5-17
6. Remove Kapton from PPT and inspect for sulfur check, Figure 5-17
7. Inspect for cracks on solar panels, make note check, Figure 5-17
8. Remove Kapton from sun sensor check

Figure 5-17 Sulfur fuel post-transport inspection

Launch of the Cygnus NG-12 mission on an Antares 230+ occurred at 13:59:47 UTC November 2nd, 2019 from the Mid Atlantic Regional Spaceport. The spacecraft docked with the ISS Nov 4th, 2019 and departed on Jan 31st, 2020, for a total of 88 days on station. The orbit was then raised to 465 km, still with an inclination of 51.6 degrees, and HuskySat was confirmed to have deployed at 22:30:03 UTC on January 31st, 2020. The departure of the Cygnus capsule and deployment of HuskySat with a 0.5 m/s Δv imparted by the deployment spring are depicted in Figure 5-18.

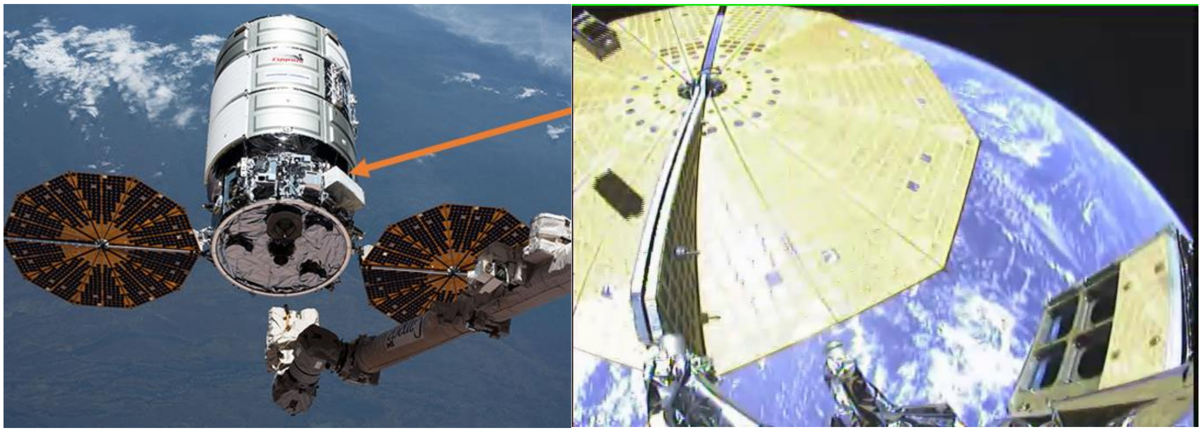

Figure 5-18 Cygnus capsule departing the space station with Nanoracks deployer (left) and the opening of deployer door two with HuskySat in top left (right) [Garcia and Nanoracks]

5.6 Flight Results

5.6.1 General operation

First contact was made with the satellite on the first active pass over Seattle at approximately 16:27 PST on January 31st. The command switched the satellite from its original “safe-mode” into “health-mode”. The important distinction between the two modes is that the satellite is continuously transmitting when in health mode. When attempting to locate a satellite for the first few passes while it is still very close to other satellites in the same deployment, it is much easier if the signal is consistent. In safe mode, the satellite only transmits every two minutes for 30 seconds.

The partnership with AMSAT and operation on amateur frequencies allows stations all over the world to downlink data from HuskySat. The data is then stored on a telemetry server. Because of this, health data from the satellite is available with a large global coverage. This Whole Orbit Data, or WOD, is a fine scale record of several key health parameters on the satellite.

Figure 5-19 is an example of WOD data for the battery charge, as measured by a coulomb counter, and battery voltage. It is quickly obvious that the satellite is going through eclipse cycles. At the minimum of the battery charge or batter voltage curves, the satellite is just coming out of eclipse and starts to charge. Depending on the orbit, the battery reaches full charge and peak voltage before going into a lower top-off charging state. In eclipse, the charging ceases and the battery loses charge until it is again in the sun. The regularity of the curves and the fact that the satellite has extra time in the fully charged state are both positive signs for the health of the satellite and the batteries.

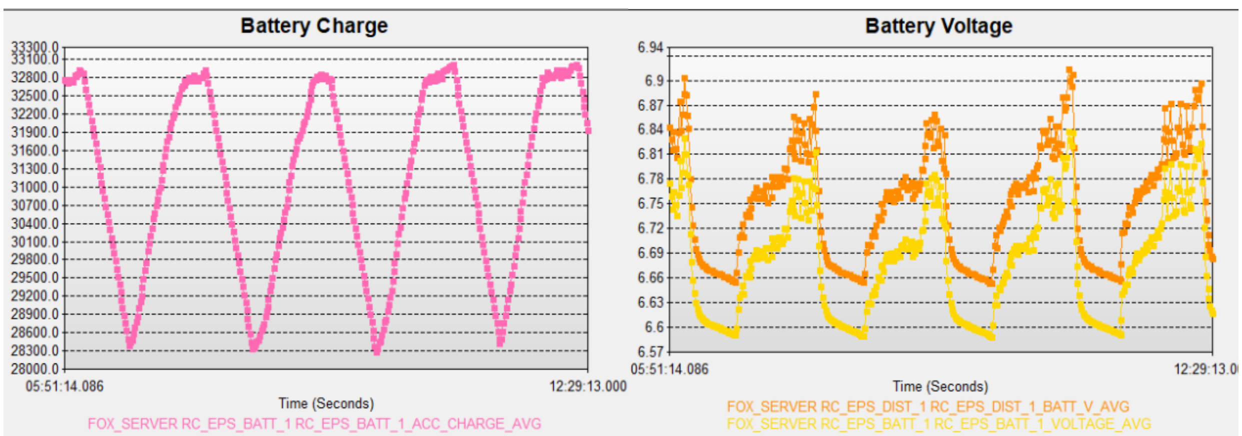

Figure 5-19 Whole Orbit Data for battery charge and voltage

The B-dot algorithm on the ADCS system is designed to help the satellite slow any tumble that it has. The board has not yet been turned on, as health data has indicated a span of 0-6 degrees per second rotation rate on all three of the axes. The rotation is also observed in the solar panel power data in Figure 5-20, where the amount of power to each panel is constantly varying as the satellite rotates and different panels are faced towards the sun.

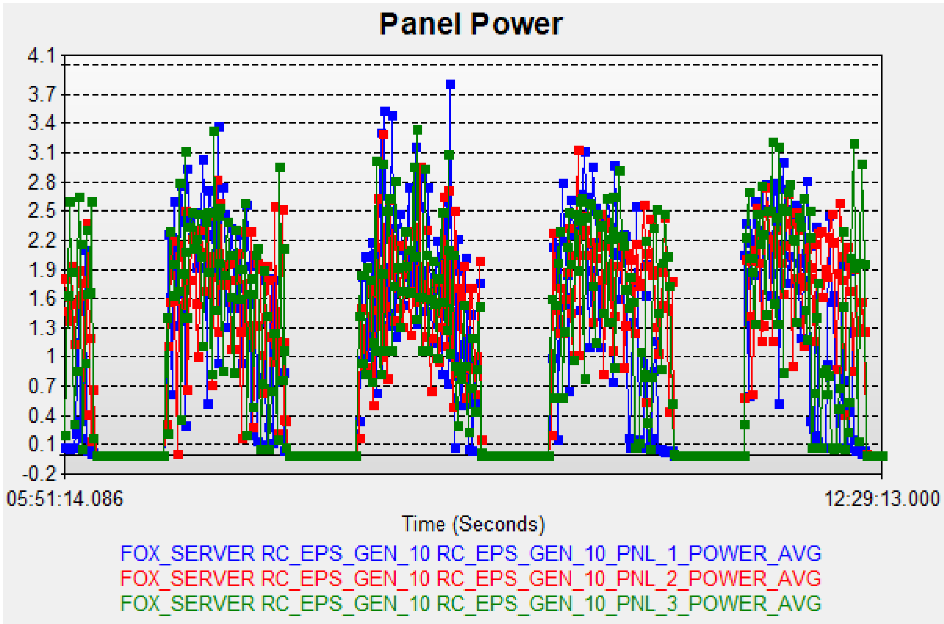

Figure 5-20 Whole Orbit Data for panel power

5.6.2 Pulsed Plasma Thruster In-Space Testing

Pulsed plasma thruster work has been done in increments. Testing progressed in a conservative fashion to limit the potential of damaging the satellite in the event of a failure. The initial overcurrent protection (OCP) limit on the distribution board was set at 4 Amps. The OCP is the only setting related to the PPT that can be changed while the system is off.

1) The first test was to turn on the system at the distribution board level. This test indicated that the system was drawing a steady current of 0.068 to 0.072 Amps, with an average current draw of 0.071 Amps. This is consistent with ground testing. It indicates that the system is both connected and not shorted or otherwise damaged in a way that would enable higher current draw.

2) The second test was to test the OCP shutoff, to confirm that the distribution board would turn off power to the PPT system in the event the current draw was higher that the set OCP limit. The test was done by charging the main capacitors with the OCP set to 3 Amps, which was known from ground testing to be insufficient. The OCP was tripped and the PPT turned off.
3) The third test was to assess the success, timing, and current draw of main capacitor charging. The OCP was set to 10 Amps, the maximum current indication was reset, and the main capacitors charged. The results were the following

Table 5-5 Main charge time and current

Main charged? (Y/N)	Main charge time (ms)	Max current draw (Amps)
Yes	643.7	6.609
Yes	678.5	6.719

4) The fourth test checked the discharge time of the capacitors indirectly by charging the main twice in quick succession. A bleed resistor discharges the capacitors as an inhibit. The command to fire was sent twice 10 seconds apart. The last main charge time was 315.6 ms.
5) The fifth test fired the ignitor without the main charge. This is a final checkout to adjust OCP as needed and test the ignitor before a full discharge. The timing of the main charge was set to 20 ms, which does not give it enough time to achieve appreciable charge. The Schmitt trigger was set to override. Without override, the Schmitt trigger will throw a fault if not high before ignitor fire, so the override is needed to fire the ignitor without charging

the main. The result of this test was OCP shutoff, so the OCP limit was raised to 9 Amps and tested again, with a maximum current draw of 7.9 Amps. Testing moved forward with an adjusted OCP limit of 8.5 Amps.

In summary, before firing, the following checkout tests were conducted:

Table 5-6 Propulsion check-out results

Test	**Result**
General operation	Nominal, 71.3 mA average current
Over current protection working	Nominal, OCP shutoff observed
Main capacitor charging characteristics	Nominal, ~660 ms charge time, 6.7A max current
Capacitor discharge	315 ms charge time after a 10s delay
Ignitor current draw	Max current 7.9 Amps

The final test was to fire the thruster. OCP set to 8.5 Amps, timing set to 793ms for main charge, 1ms delay, and 20 ms ignitor fire time. The result was a NO_MAIN_DISCHARGE fault, which means the main had charged fully but not discharged when the ignitor fired, leading to the belief that the ignitor fire time needed to be increased.

The igniter time was increased to 30 ms and the system fired again. The result was the same, which indicated that the ignition time may need to be further increased. Three further attempts with ignitor timing at 35 ms, 40 ms, and 50 ms were tested, again with the

NO_MAIN_DISCHARGE fault. The maximum current for these three tests was 7.8A, 8.1A and 7.9A. Benchtop testing in the Thunderbox setup only pulled peak currents ~ 6A. This is significant but could also be explained by a combination of longer current paths from a different power source at room temperature with greater inductance.

It is not possible to determine exactly what has failed in the ignition, but a lack of main discharge while the ignitor is pulling more current than seen in testing indicates that the problem is within the ignitor itself. The higher current is potentially attributable to the factors mentioned previously, in which case a faulty connection or insulation of the ignition output could result in arcing outside the thruster electrodes. If the combination of power source, wiring, and temperature do not account for the change in peak current, the most likely explanation is fault within the off-the-shelf high voltage generator internal electronics.

AMSAT became the officially licensed operators of HuskySat-1 on May 1st, 2020. At that time, all commanding from the UW ground station was halted and the satellite was repurposed as an amateur linear transponder.

5.7 SUMMARY

The propulsion system was designed to provide up to 100 m/s Δv for the HuskySat-1 3U+ CubeSat. Given the constraints of a student-built satellite, the flight thruster was only to be tested to under 1000 pulses. The reduced function did not reduce the testing and safety requirements for launch, and the HuskySat pulsed plasma thruster went through iterations to pass NASA hardware acceptance reviews. In-space testing of the thruster failed in the ignition system, but, with an upgrade to the ignition hardware, the pulsed plasma thruster on HuskySat-1 is a novel addition to

CubeSat propulsion with higher thrust output than other CubeSat PPTs. The flight heritage of the HuskySat thruster, simply as a thruster, also paves the way for future university programs to fly propulsion units. It also increases the TRL of the high specific thrust pulsed plasma thruster, setting it up to be a propulsion option for future missions.

References

Abe, Shinsuke, et al. “Mass and Local Topography Measurements of Itokawa by Hayabusa.” *Science*, vol. 312, no. 5778 (2006): 1344–1347

Accion Systems “TILE Next-Generation Ion Propulsion” https://static1.squarespace.com/static/5446faa2e4b025843cfc6731/t/59ce4f211f318d6cc856ca0d/1506692898494/TILE+Product+Family+Data+Sheet.pdf, Accessed 05 Jan 2020.

Anderson, Gina, and Courtney Beasley. “NASA TV to Air Departure of Cygnus Cargo Spacecraft from Space Station.” *NASA*, NASA, 24 Jan. 2020, www.nasa.gov/press-release/nasa-tv-to-air-departure-of-cygnus-cargo-spacecraft-from-space-station, Accessed 15Mar 2020.

Azuara Rosales, Manuel, Robert Winglee, and Paige Northway. "Air-Breathing Pulsed Plasma Thruster with a Variable Spacing Cathode for Atmospheric Satellite Applications." *53rd AIAA/SAE/ASEE Joint Propulsion Conference* (2017).

Behrens, Jonathan R., and Bhavya Lal. "Exploring Trends in the Global Small Satellite Ecosystem." *New Space* 7.3 (2019): 126-136.

Biele, Jens, et al. "The landing (s) of Philae and inferences about comet surface mechanical properties." *Science* 349.6247 (2015): aaa9816.

Bentor, Yinon. “Chemical Elements.com - An Interactive Periodic Table of the Elements.” *Chemical Elements.com*, chemicalelements.com. Accessed 04 Feb 2020

Beshore, Edward, et al. "The OSIRIS-REx asteroid sample return mission." *2015 IEEE Aerospace Conference*. IEEE, 2015.

Bradford. “1 N HPGP Thruster.” *Bradford ECAPS - Products - 1N HPGP Thruster*, www.ecaps.space/products-1n.php, Accessed 25 Jan 2020.

Burton, R, and P Turchi. “Pulsed Plasma Thruster.” *Journal of Propulsion and Power*, 14. 5, (1998): 716–735.

Busek Products, Busek Co. , www.busek.com/technologies__main.htm, Accessed 25 Jan 2020.

Cassen, P., R. T. Reynolds, and S. J. Peale. "Is there liquid water on Europa?."*Geophysical Research Letters* 6, no. 9 (1979): 731-734

Ciaralli, S., M. Coletti, and S. B. Gabriel. "Results of the qualification test campaign of a Pulsed Plasma Thruster for Cubesat Propulsion (PPTCUP)." *Acta Astronautica* 121 (2016): 314-322.

Clark, Beth E., et al. "Space weathering on Eros: Constraints from albedo and spectral measurements of Psyche crater." *Meteoritics & Planetary Science* 36.12 (2001): 1617-1637.

Clark, Pamela E., et al. "Lunar Ice Cube: first generation deep space CubeSat with compact broadband IR spectrometer development story." *CubeSats and SmallSats for Remote Sensing III*. Vol. 11131. International Society for Optics and Photonics, 2019.

Cooley, Sarah W., et al. "Tracking dynamic northern surface water changes with high-frequency planet CubeSat imagery." *Remote Sensing* 9.12 (2017): 1306.

(CU Aerospace) "Small-Satellite Propulsion Unit for CubeSats (PUC)." *CU Aerospace*, www.cuaerospace.com/technology-products/compact-small-satellite-propulsion-unit-cubesats.

(Decadal) Vision and Voyages for Planetary Science in the Decade 2013-2022, Committee on the Planetary Science Decadal Survey Space Studies Board, National Research Council, The National Academies Press, Washington, DC, 2011; NASA 2014 Science Plan, https://smd-prod.s3.amazonaws.com/science-blue/s3fs-public/atoms/files/2014_Science_Plan_PDF_Update_508_TAGGED.pdf

Dunbar, Brian. "Technology Readiness Level." *NASA*, NASA, 28 Oct. 2012, www.nasa.gov/directorates/heo/scan/engineering/technology/txt_accordion1.html, Accessed 14 Jan 2020.

Dykhuis, Melissa J., et al. "Defining the Flora Family: Orbital properties, reflectance properties and age." *Icarus* 243 (2014): 111-128.

Enpulsion Technology, Enpulsion, www.enpulsion.com/technology/, Accessed 25 Jan 2020

Fesq, Lorraine, et al. "Extended Mission Technology Demonstrations Using the ASTERIA Spacecraft." *2019 IEEE Aerospace Conference*, vol. 2019 (2019): 1–11.

Foust, Jeff. "Europa Clipper Instrument Change Could Affect Mission Science." *SpaceNews.com*, 26 Apr. 2019, spacenews.com/europa-clipper-instrument-change-could-affect-mission-science/.

Gaffey, Michael J. "Rotational spectral variations of asteroid (8) Flora: Implications for the nature of the S-type asteroids and for the parent bodies of the ordinary chondrites." *Icarus* 60.1 (1984): 83-114.

Gaidos, Eric J., and Francis Nimmo. "Planetary science: tectonics and water on Europa." *Nature* 405, no. 6787 (2000): 637-637.

Garcia, Mark. "NASA TV Broadcasts Cygnus Cargo Craft Departure." *NASA Space Station*, NASA, 30 Jan. 2020, blogs.nasa.gov/spacestation/2020/01/30/nasa-tv-broadcasts-cygnus-cargo-craft-departure/.

Ghorbanzadeh, Omid, et al. "Evaluation of different machine learning methods and deep-learning convolutional neural networks for landslide detection." *Remote Sensing* 11.2 (2019): 196.

Glassmeier, Karl-Heinz, et al. "The Rosetta mission: flying towards the origin of the solar system." *Space Science Reviews* 128.1-4 (2007): 1-21.

Greenwood, N. N., and Earnshaw, A. Chemistry of the Elements. 2nd ed., Butterworth-Heinemann, 1998. pp. 655

Guman, William J., and David M. Nathanson. "Pulsed plasma microthruster propulsion system for synchronous orbit satellite." *Journal of Spacecraft and Rockets* 7.4 (1970): 409-415.

Haag, Thomas W. "Thrust stand for pulsed plasma thrusters." *Review of Scientific Instruments* 68.5 (1997): 2060-2067.

Henke, Burton L., Eric M. Gullikson, and John C. Davis. "X-ray interactions: photoabsorption, scattering, transmission and reflection E= 50-30,000 eV, Z= 1-92." *Atomic data and nuclear data tables* 54.2 (1993).

Hernando-Ayuso, Javier, et al. "OMOTENASHI trajectory analysis and design: Landing phase." *Acta Astronautica* 156 (2019): 113-124.

Hiroi, Takahiro, et al. "Developing space weathering on the asteroid 25143 Itokawa." *Nature* 443.7107 (2006): 56-58.

Hodgson, Darel E., Ming H. Wu, and Robert J. Biermann. "ASM Handbook, Volume 2, Properties and Selection, Nonferrous Alloys and Special-Purpose Materials." (1990).

Ira, Katz, et al. "Numerical simulations of ion thruster accelerator grid erosion." *38th AIAA/ASME/SAE/ASEE Joint Propulsion Conference & Exhibit*. (2002).

Jaumann, Ralf, et al. "Images from the surface of asteroid Ryugu show rocks similar to carbonaceous chondrite meteorites." *Science* 365.6455 (2019): 817-820.

Johannesen, J., and L. D'Amario. "Europa orbiter mission trajectory design." (1999).

Johnson, Ian Kronheim. *The Development of a Pulsed Plasma Thruster as a Solid Fuel Plasma Source for a High Power Helicon*. Diss. University of Washington, 2011.

Keidar, Michael, Iain D. Boyd, and Isak I. Beilis. "On the model of Teflon ablation in an ablation-controlled discharge." *Journal of Physics D: Applied Physics* 34.11 (2001): 1675.

Kim, Vladimir, et al. "Electric propulsion activity in Russia." *IEPC Paper* 5 (2001): 2001.

Kivelson, Margaret G., et al. "Galileo magnetometer measurements: A stronger case for a subsurface ocean at Europa." *Science* 289.5483 (2000): 1340-1343.

Klesh, Andrew T., John Baker, and Joel Krajewski. "MarCO: Flight review and lessons learned." *33rd Annual AIAA/USU Conference on Small Satellites* (2019).

Kulu, Erik “Nanosatellite and CubeSat Database” *Nanosats Database*, 03Jan 2020, www.nanosats.eu/database. Acceessed 12 Apr 2020.

“LightSail.” *The Planetary Society Blog*, www.planetary.org/explore/projects/lightsail-solar-sailing/#the-lightsail-2-mission. Accessed 15 Jan 2020.

Lewis, John S. "Satellites of the outer planets: Their physical and chemical nature." *Icarus* 15, no. 2 (1971): 174-185.

(LT3750 Datasheet) https://www.analog.com/media/en/technical-documentation/data-sheets/3750fa.pdf, Accessed 10 Mar 2020.

Manzella, David, Jihn Yim, and Iain Boyd. "Predicting Hall thruster operational lifetime." *40th*

AIAA/ASME/SAE/ASEE Joint Propulsion Conference and Exhibit (2004).

Mcnamara, Karen M. “NASA Technology Readiness Level Definitions.” *Perfonnance Metrics for Intelligent Systems*, 2012, Perfonnance Metrics for Intelligent Systems; 20–22 Mar. 2012; Hyattsville, MD; United States.

Moore, Christopher S., et al. "The Instruments and Capabilities of the Miniature X-Ray Solar Spectrometer (MinXSS) CubeSats." *Solar physics* 293.2 (2018): 21.

Naka, Masamichi, et al. "Development of electrothermal pulsed plasma thruster system flight-model for the PROITERES satellite." *32nd International Electric Propulsion Conference*. 2011.

NanoAvionics “A Successful In-Orbit Test of the First Ever Chemical Propulsion System Running On-Board a CubeSat Was Performed.” *NanoAvionics*, 31 July 2018, nanoavionics.com/news/successful-orbit-test-first-ever-chemical-propulsion-system-running-board-cubesat-performed/, Accessed 29 Feb 2020.

Nanoracks, personal communication, 19 Feb 2020.

Nawaz, Anuscheh, Riccardo Albertoni, and Monika Auweter-Kurtz. "Thrust efficiency optimization of the pulsed plasma thruster SIMP-LEX." *Acta Astronautica* 67.3-4 (2010): 440-448.

Northway, Paige, et al. "Pulsed Plasma Thruster Gains in Specific Thrust for CubeSat Propulsion." *53rd AIAA/SAE/ASEE Joint Propulsion Conference*. 2017.

Orphee, Juan, et al. “Near Earth Asteroid (NEA) Scout Solar Sail Implementation.” Annual AIAA/USU Conference on Small Satellites (2016).

(Orbion) *Orbion Space Technology*, www.orbionspace.com, Accessed 15 Feb 2020.

“12. Passive Deorbit Systems.” *State of the Art of Small Spacecraft Technology*, NASA, 12 Mar. 2019, https://sst-soa.arc.nasa.gov/12-passive-deorbit-systems, Accessed 12 Feb 2020.

Periasamy, Lavanya & Gasiewski, Al. (2018). Prelaunch Performance of the 118.75 GHZ Polarcube 3U Cubesat Temperature Sounding Radiometer. 10.1109/IGARSS.2018.8519535.

Pieters, C. M, et al., (2012) Distinctive space weathering on Vesta from regolith mixing processes, *Nature*, 491, doi:10.1038/nature11534

Pezent, James, Rohan Sood, and Andrew Heaton. "High-fidelity contingency trajectory design and analysis for NASA's near-earth asteroid (NEA) Scout solar sail Mission." *Acta Astronautica* 159 (2019): 385-396.

“Process for Limiting Orbital Debris,” “NASA-STD-8719.14, Rev. A,” 2011, https://standards.nasa.gov/standard/nasa/nasa-std-871914. Accessed 30 Mar 2020

“04 Propulsion.” *State of the Art of Small Spacecraft Technology*, NASA, 19 Mar. 2020, https://sst-soa.arc.nasa.gov/12-passive-deorbit-systems, Accessed 13 Feb 2020.

“PSLV-C37 Successfully Launches 104 Satellites in a Single Flight.” *ISRO Update*, ISRO, 15 Feb. 2017, www.isro.gov.in/update/15-feb-2017/pslv-c37-successfully-launches-104-satellites-single-flight.

Rayburn, Christopher, et al. "Development of a micro pulsed plasma thruster for the Dawgstar nanosatellite." *36th AIAA/ASME/SAE/ASEE Joint Propulsion Conference and Exhibit*. 2000.

RBC Signals. “Customers.” *RBC Signals*, RBC Signals, www.rbcsignals.com/customers/, Accessed 14 Feb 2020.

Rezaeiha, Abdolrahim, and Tony Schönherr. "Review of worldwide activities in liquid-fed pulsed plasma thruster." *Journal of Propulsion and Power* 30.2 (2014): 253-264.

Roth, N., et al. "Flight results from the CanX-4 and CanX-5 formation flying mission." *Proceedings of the Small Satellites, Systems & Services Symposium (4S), Valletta, Malta*. Vol. 30, (2016).

Sarda, Karan, et al. "Canadian advanced nanospace experiment 2 orbit operations: two years of pushing the nanosatellite performance envelope." *ESA small satellites, services and systems symposium*. Vol. 20, (2010).

“Schedule and Pricing.” *Spaceflight*, www.spaceflight.com/schedule-pricing/, Accessed 17 Jan 2020.

Standard, General Environmental Verification. *for GSFC Flight Programs and Projects*. GSFC-STD-7000, http://msc-docsrv.gsfc.nasa.gov/cmdata/170/STD/GEVS-STD-7000.pdf, 2013.

Tanuma, Shigeo, Cedric J. Powell, and David R. Penn. "Calculations of electron inelastic mean free paths. III. Data for 15 inorganic compounds over the 50–2000 eV range." *Surface and Interface analysis* 17.13 (1991): 927-939.

Tethers Unlimited “Hydros” *Tethers Unlimited*, http://www.tethers.com/wp-content/uploads/2019/09/2019-HYDROS.pdf Accessed 25 Jan 2020.

Thrasher, Jason, et al. "Pulsed Plasma Thruster Development Using a Novel HAN-Based Green Electric Monopropellant." *52nd AIAA/SAE/ASEE Joint Propulsion Conference*. 2016.

Tsuchiyama, Akira, et al. “Three-Dimensional Structure of Hayabusa Samples: Origin and Evolution of Itokawa Regolith.” *Science (New York, N.Y.)*, vol. 333, no. 6046 (2011): 1125–1128.

Tsuda, Yuichi, et al. "Hayabusa2 Mission Status: Landing, Roving and Cratering on Asteroid Ryugu." *Acta Astronautica* (2020).

VACCO. “CubeSat Propulsion Systems from VACCO Industries.” *VACCO Industries*, 10 Sept. 2019, www.cubesat-propulsion.com, Accessed 25 Jan 2020.

Valdes, Arturo, and Khashayar Khorasani. "A pulsed plasma thruster fault detection and isolation strategy for formation flying of satellites." *Applied Soft Computing* 10.3 (2010): 746-758.

Veverka, J, et al. “Galileo's Encounter with 951 Gaspra: Overview.” *Icarus*, vol. 107, no. 1, (1994): 2–17.

Walsh, K. J., and A. Morbidelli, The effect of an early planetesimal-driven migration of the giant planets on terrestrial planet formation *Astronomy and Astrophysics*, *526*, 8, (2011).

Wertz, James R., David F. Everett, and Jeffery J. Puschell. *Space mission engineering: the new SMAD*. Microcosm Press, 2011.

West, Adam D., et al. "An underappreciated radiation hazard from high voltage electrodes in vacuum." *Health physics* 112.1 (2017): 33-41.

Weston, Sasha, et al. "State of the Art: Small Spacecraft Technology." (2018).

Zakrzwski, Chuck, et al. "On-orbit testing of the EO-1 pulsed plasma thruster." *38th AIAA/ASME/SAE/ASEE Joint Propulsion Conference & Exhibit*. 2002.

Ziemer, John K. "A review of gas-fed pulsed plasma thruster research over the last half-century." *Electric Propulsion and Plasma Dynamics Lab report, Princeton University* (2000).

Appendix

List of Telemetry packets and commands

The Telemetry handbook of the flight code can be found at:

https://github.com/UWCubeSat/DS1Ops/blob/master/COSMOS/flight/outputs/handbooks/command_handbook.pdf

The Command handbook of the flight code can be found at:

https://github.com/UWCubeSat/DS1Ops/blob/master/COSMOS/flight/outputs/handbooks/command_handbook.pdf

Programming for Flight PPT MSP430

```
#include
<msp430.h>
#include "PPT.h"

#include "bsp/bsp.h"
#include <core/timers.h>
#include "interfaces/canwrap.h"
#include "core/agglib.h"

#define OPCODE_COMMON_CMD 0
#define OPCODE_START_FIRE 2
#define OPCODE_STOP_FIRE 3
#define OPCODE_GET_TIMING 4
#define OPCODE_SET_TIMING 5

#define LED_DIR P1DIR
#define LED_OUT P1OUT
#define LED_BIT_IDLE BIT0
#define LED_BIT_FIRING BIT1
#define CHARGE_DIR P4DIR
#define CHARGE_OUT P4OUT
#define MAIN_CHARGE_BIT BIT3
#define IGN_CHARGE_BIT BIT1
#define SMT_IN P4IN
#define SMT_IN_BIT BIT0
#define MAIN_DONE_BIT BIT6

#define BATTERY_CHARGE_SUFFICIENT_STATE 31000 //TODO: verify this value

//Things that determine whether the PPT can fire:
uint8_t aboveGrndStation = 0;
uint8_t battChargeOK = 0;

//FLAGS:
uint8_t sendRcFlag = 0;

// Main status (a structure) and state and mode variables
```

```
// Make sure state and mode variables are declared as volatile
FILE_STATIC volatile ModuleStatus mod_status;

FILE_STATIC uint8_t firing;
FILE_STATIC uint8_t currTimeout;
FILE_STATIC uint8_t withFiringPulse;
FILE_STATIC uint8_t smtOverride;

// These are sample "trigger" flags, used to indicate to the main loop
// that a transition should occur
FILE_STATIC flag_t triggerState1;
FILE_STATIC flag_t triggerState2;
FILE_STATIC flag_t triggerState3;

#pragma PERSISTENT(mainChargeTime)
#pragma PERSISTENT(mainIgniterDelay)
#pragma PERSISTENT(igniterChargeTime)
#pragma PERSISTENT(cooldownTime)

FILE_STATIC uint16_t mainChargeTime = 36045;
FILE_STATIC uint16_t mainIgniterDelay = 32;
FILE_STATIC uint16_t igniterChargeTime = 655;
FILE_STATIC uint16_t smtWaitTime = 262; //~8ms
FILE_STATIC uint16_t cooldownTime = 28461;

//MEASURED Values:
#pragma PERSISTENT(lastMainChargeTime)
uint16_t lastMainChargeTime = 0;

//firing flag (used to determine state after reset)
#pragma PERSISTENT(fireAttempt)
volatile uint8_t fireAttempt = 0;

FILE_STATIC ppt_main_done mainDone;
FILE_STATIC meta_segment mseg;
FILE_STATIC health_segment hseg;
FILE_STATIC timing currTiming;
FILE_STATIC fireInfo fireSeg; //ID: 7

aggVec_f mspTempAg;
#pragma PERSISTENT(fireCount)
uint16_t fireCount = 0;
#pragma PERSISTENT(faultCount)
uint16_t faultCount = 0;
#pragma PERSISTENT(lastFireResult)
LastFireResult lastFireResult = 3;//Result_FireSuccessful;

void initData()
{
    aggVec_init_f(&mspTempAg);
}

FILE_STATIC void sendMainDone()
{
         if(mod_status.ss_state == State_Main_Charging)
         {
                  mainDone.timeDone = mainChargeTime + TB0R - TB0CCR1;
                  lastMainChargeTime = mainDone.timeDone;
                  bcbinSendPacket((uint8_t *)&mainDone, sizeof(mainDone));
         }
         else
         {
                  mainDone.timeDone = 0;
         }
}

FILE_STATIC void sendMeta()
{
    // TODO:  Add call through debug registrations for INFO on subentities (like the buses)
    bcbinPopulateMeta(&mseg, sizeof(mseg));
    bcbinSendPacket((uint8_t *) &mseg, sizeof(mseg));
}

FILE_STATIC void sendHealth()
{
    // For now, everythingis always marginal ...
```

```
    hseg.oms = OMS_Unknown;
    hseg.reset_count = bspGetResetCount();
    hseg.inttemp = asensorReadIntTempC();
    aggVec_push_f(&mspTempAg, hseg.inttemp);
    bcbinSendPacket((uint8_t *) &hseg, sizeof(hseg));
}

FILE_STATIC void sendTiming()
{
    currTiming.mainChargeTime = mainChargeTime;
    currTiming.mainIgniterDelay = mainIgniterDelay;
    currTiming.igniterChargeTime = igniterChargeTime;
    currTiming.cooldownTime = cooldownTime;
    bcbinSendPacket((uint8_t *)&currTiming, sizeof(currTiming));
}

////////////////////////////////////////////////////////////////

void initPins()
{
    LED_DIR |= (LED_BIT_FIRING | LED_BIT_IDLE);
    CHARGE_DIR |= (IGN_CHARGE_BIT| MAIN_CHARGE_BIT);

    //main done interrupt
    P2IFG = 0; //clear the interrupt
    P2REN |= MAIN_DONE_BIT; //enable pullup/down resistor
    P2IES |= MAIN_DONE_BIT; //falling edge capture mode
    P2IE |= MAIN_DONE_BIT; //enable interrupt
}

void checkFireState()
{
    if(fireAttempt)
    {
        if(SMT_IN & SMT_IN_BIT)
        {
            lastFireResult = Result_MainFailedDischarge;
            faultCount++;
        }
        else
        {
            lastFireResult = Result_FireSuccessful;
            fireCount++;
        }
        fireAttempt = 0;
    }
}

void sendRC()
{
    while(sendRcFlag && canTxCheck() != CAN_TX_BUSY)
    {
        CANPacket pkt = {0};
        if(sendRcFlag == 4)
        {
            rc_ppt_h1 rc = {0};
            rc.rc_ppt_h1_reset_count = bspGetResetCount();
            rc.rc_ppt_h1_sysrstiv = bspGetResetReason();
            rc.rc_ppt_h1_temp_avg = compressMSPTemp(aggVec_avg_f(&mspTempAg));
            rc.rc_ppt_h1_temp_max = compressMSPTemp(aggVec_max_f(&mspTempAg));
            rc.rc_ppt_h1_temp_min = compressMSPTemp(aggVec_min_f(&mspTempAg));
            encoderc_ppt_h1(&rc, &pkt);
            aggVec_as_reset((aggVec *)&mspTempAg);
        }
        else if(sendRcFlag == 3)
        {
            rc_ppt_h2 rc = {0};
            rc.rc_ppt_h2_canrxerror = canRxErrorCheck();
            rc.rc_ppt_h2_last_fire_result = lastFireResult;
            encoderc_ppt_h2(&rc, &pkt);
        }
        if(sendRcFlag == 2)
        {
            rc_ppt_1 rc = {0};
            rc.rc_ppt_1_fault_count = faultCount;
            rc.rc_ppt_1_fire_count = fireCount;
```

```
            rc.rc_ppt_1_last_main_charge = lastMainChargeTime;
            rc.rc_ppt_1_smt_wait_time = smtWaitTime;
            encoderc_ppt_1(&rc, &pkt);
        }
        else if(sendRcFlag == 1)
        {
            rc_ppt_2 rc = {0};
            rc.rc_ppt_2_cooldown_time = cooldownTime;
            rc.rc_ppt_2_ign_charge_time = igniterChargeTime;
            rc.rc_ppt_2_main_charge_time = mainChargeTime;
            rc.rc_ppt_2_main_ign_delay = mainIgniterDelay;
            encoderc_ppt_2(&rc, &pkt);
        }
        canSendPacket(&pkt);
        sendRcFlag--;
    }
}

void sendFire()
{
    fireSeg.faultCount = faultCount;
    fireSeg.fireCount = fireCount;
    fireSeg.lastFireResult = (uint8_t)lastFireResult;
    bcbinSendPacket((uint8_t *)&fireSeg, sizeof(fireSeg));
}

void blinkLED()
{
    if(firing)
        LED_OUT ^= LED_BIT_FIRING;
    else
        LED_OUT ^= LED_BIT_IDLE;
}

void startFiring(uint8_t timeout);
void stopFiring();
void mainLow();
void igniterHigh();
void fire();
void can_packet_rx_callback(CANPacket *packet);

/*
 * main.c
 */
int main(void)
{

    /* ----- INITIALIZATION -----*/
    // ALWAYS START main() with bspInit(<systemname>) as the FIRST line of code, as
    // it sets up critical hardware settings for board specified by the __BSP_Board... definition used.
    // If module not yet available in enum, add to SubsystemModule enumeration AND
    // SubsystemModulePaths (a string name) in systeminfo.c/.h
    //bspInit(__SUBSYSTEM_MODULE__);  // <<DO NOT DELETE or MOVE>>
    bspInit(Module_PPT);
    asensorInit(Ref_2p5V);
    canWrapInitWithFilter();
    // This function sets up critical SOFTWARE, including "rehydrating" the controller as close to the
    // previous running state as possible (e.g. 1st reboot vs. power-up mid-mission).
    // Also hooks up sync pulse handlers.  Note that actual pulse interrupt handlers will update the
    // firing state structures before calling the provided handler function pointers.
    mod_status.ss_mode = Mode_Undetermined;
    mod_status.ss_state = State_Uncommissioned;

    canWrapInitWithFilter();
    setCANPacketRxCallback(can_packet_rx_callback);

    initPins();
    initData();
    checkFireState();

    TB0CTL = TBSSEL__ACLK | MC__CONTINOUS | TBCLR | TBIE;

#if defined(__DEBUG__)
    // Insert debug-build-only things here, like status/info/command handlers for the debug
    // console, etc.  If an Entity_<module> enum value doesn't exist yet, please add in
    // debugtools.h.  Also, be sure to change the "path char"
```

```
    debugRegisterEntity(Entity_SUBSYSTEM, NULL,
                                          NULL,
                                          handleDebugActionCallback);

    //hBus handle = uartInit(BackchannelUART, 1, DEBUG_UART_SPEED);
    //uartRegisterRxCallback(handle, handleDebugActionCallback); //debugReadCallback

#endif  //  __DEBUG__

    /* ----- CAN BUS/MESSAGE CONFIG -----*/
    // TODO:  Add the correct bus filters and register CAN message receive handlers

    debugTraceF(1, "CAN message bus configured.\r\n");

    /* ----- SUBSY\STEM LOGIC -----*/
    // TODO:  Finally ... NOW, implement the actual subsystem logic!
    // In general, follow the demonstrated coding pattern, where action flags are set in interrupt
handlers,
    // and then control is returned to this main loop

    debugTraceF(1, "Commencing subsystem module execution ...\r\n");

    uint32_t counter = 0;

    bcbinPopulateHeader(&currTiming.header, 5, sizeof(currTiming));
    bcbinPopulateHeader(&(hseg.header), TLM_ID_SHARED_HEALTH, sizeof(hseg));
    bcbinPopulateHeader(&mainDone.header, 3, sizeof(mainDone));
    bcbinPopulateHeader(&fireSeg.header, 6, sizeof(fireSeg));

    withFiringPulse = 1;
    smtOverride = 0;

    while (1)
    {
        __delay_cycles(SEC * 0.1);
        if (!(counter % 8))
        {
            blinkLED();
        }
        if (!(counter % 16))
        {
            sendMeta();
            sendHealth();
            sendFire();
        }
        sendRC();
        counter++;
    }
}

void startFiring(uint8_t timeout)
{
    if(!firing && timeout)
    {
        LED_OUT &= ~LED_BIT_IDLE;
        currTimeout = timeout - 1;
        mod_status.ss_state = State_Cooldown;
        TB0CCR1 = TB0R + cooldownTime;
        TB0CCTL1 = CCIE;
        firing = 1;
    }
}

void stopFiring()
{
    if(firing)
    {
        TB0CCTL1 &= ~CCIE;
        LED_OUT &= ~LED_BIT_FIRING;
        mod_status.ss_state = State_Uncommissioned;
        firing = 0;
        CHARGE_OUT &= ~(MAIN_CHARGE_BIT | IGN_CHARGE_BIT);
        withFiringPulse = 1;
        smtOverride = 0;
    }
}
```

```
uint8_t handleDebugActionCallback(DebugMode mode, uint8_t * cmdstr) //this should be the one that gets
called when a cmd comes in
{
    if (mode == Mode_BinaryStreaming)
    {
        //this is the one
        switch(cmdstr[0])
        {
            case OPCODE_COMMON_CMD:
                break;
            case OPCODE_START_FIRE://OPCODE_MY_CMD:
                startFiring(((start_firing *) (cmdstr + 1))->timeout);
                break;
            case OPCODE_STOP_FIRE:
                stopFiring();
                break;
            case OPCODE_GET_TIMING:
                sendTiming();
                break;
            case OPCODE_SET_TIMING:
            {
                set_timing *fireTiming = (set_timing *)(cmdstr + 1);
                if(fireTiming->mainChargeTime)
                    mainChargeTime = fireTiming->mainChargeTime;
                if(fireTiming->mainIgniterDelay)
                    mainIgniterDelay = fireTiming->mainIgniterDelay;
                if(fireTiming->igniterChargeTime)
                    igniterChargeTime = fireTiming->igniterChargeTime;
                if(fireTiming->cooldownTime)
                    cooldownTime = fireTiming->cooldownTime;
                sendTiming();
                break;
            }
            default:
                break;
        }

        // handle actions, any output should be ground-segment friendly
        // "packet" format
    }
    return 1;
}

void can_packet_rx_callback(CANPacket *packet)
{
    gcmd_ppt_halt pktHalt = {0};
    cmd_ppt_time_upd pktTime = {0};
    cmd_ppt_single_fire pktFireSingle = {0};
    rc_adcs_estim_8 pktEstim = {0};
    rc_eps_batt_7 pktBatt = {0};
    gcmd_ppt_multiple_fire pktMultFire = {0};
    switch(packet->id)
    {
        case CAN_ID_CMD_ROLLCALL:
            sendRcFlag = 5;
            break;
        case CAN_ID_GCMD_PPT_HALT:
            //stop firing, but with a flag
            decodegcmd_ppt_halt(packet, &pktHalt);
            if(pktHalt.gcmd_ppt_halt_confirm)
                stopFiring();
            break;
        case CAN_ID_CMD_PPT_SINGLE_FIRE:
            //fire once, with flags for pulse and override
            decodecmd_ppt_single_fire(packet, &pktFireSingle);
            if (pktFireSingle.cmd_ppt_single_fire_override || readyToFire())
            {
                withFiringPulse = pktFireSingle.cmd_ppt_single_fire_with_pulse;
                smtOverride = pktFireSingle.cmd_ppt_single_fire_override_smt;
                startFiring(1);
            }
            break;
        case CAN_ID_CMD_PPT_TIME_UPD:
            //updates all times
            decodecmd_ppt_time_upd(packet, &pktTime);
```

```
            if(pktTime.cmd_ppt_time_upd_charge)
                mainChargeTime = pktTime.cmd_ppt_time_upd_charge;
            if(pktTime.cmd_ppt_time_upd_ign_delay)
                mainIgniterDelay = pktTime.cmd_ppt_time_upd_ign_delay;
            if(pktTime.cmd_ppt_time_upd_ign_charge)
                igniterChargeTime = pktTime.cmd_ppt_time_upd_ign_charge;
            if(pktTime.cmd_ppt_time_upd_cooldown)
                cooldownTime = pktTime.cmd_ppt_time_upd_cooldown;
            break;
        case CAN_ID_RC_ADCS_ESTIM_8:
            decoderc_adcs_estim_8(packet, &pktEstim);
            aboveGrndStation = pktEstim.rc_adcs_estim_8_sc_above_gs;
            break;
        case CAN_ID_RC_EPS_BATT_7:
            decoderc_eps_batt_7(packet, &pktBatt);
            //determine whether the charge is in an acceptable range
            battChargeOK = pktBatt.rc_eps_batt_7_acc_charge_avg > BATTERY_CHARGE_SUFFICIENT_STATE;
            break;
        case CAN_ID_GCMD_RESET_MINMAX:
        {
            gcmd_reset_minmax pktRst;
            decodegcmd_reset_minmax(packet, &pktRst);
            if(pktRst.gcmd_reset_minmax_ppt)
            {
                aggVec_reset((aggVec *)&mspTempAg);
            }
        }
            break;
        case CAN_ID_GCMD_PPT_MULTIPLE_FIRE:
            decodegcmd_ppt_multiple_fire(packet, &pktMultFire);
            if(pktMultFire.gcmd_ppt_multiple_fire_override || readyToFire())
                startFiring(pktMultFire.gcmd_ppt_multiple_fire_count);
            break;
        case CAN_ID_GCMD_DIST_RESET_MISSION: //clear persistent flags here
            bspClearResetCount();
            break;
    }
}

BOOL readyToFire() //okay to fire
{
    return aboveGrndStation & battChargeOK;
}

#pragma vector=PORT2_VECTOR
__interrupt void Port_2(void)
{
    switch(P2IV)
    {
        case P2IV__P2IFG6:
          sendMainDone();
          break;
        default:
            break;
    }
    P2IFG = 0; //clear the interrupt flag
}

void fire()
{
    fireAttempt = 1;
    CHARGE_OUT |= IGN_CHARGE_BIT;
}

#pragma vector = TIMER0_B1_VECTOR
__interrupt void Timer0_B1_ISR (void)
{
    switch(TB0IV)
    {
        case TBIV__NONE: break;
        case TBIV1:
            switch(mod_status.ss_state)
            {
                case State_Main_Charging:
                    CHARGE_OUT &= ~MAIN_CHARGE_BIT;
                    TB0CCR1 += mainIgniterDelay;
```

```
                    mod_status.ss_state = State_Main_Igniter_Cooldown;
                    break;
                case State_Main_Igniter_Cooldown:
                    mod_status.ss_state = State_Igniter_Charging;
                    TB0CCR1 += igniterChargeTime;
                    if(smtOverride || SMT_IN & SMT_IN_BIT) //smt trigger high
                   {
                            if(withFiringPulse)
                                    fire();
                            else
                            stopFiring();
                   }
                   else //fault: main didn't charge
                   {
                            faultCount++;
                            lastFireResult = Result_MainFailedCharge;
                            stopFiring();
                   }
                    break;
                case State_Igniter_Charging:
                    CHARGE_OUT &= ~IGN_CHARGE_BIT; //set igniter low
                    fireAttempt = 0;
                    mod_status.ss_state = State_SMT_Wait;
                    TB0CCR1 += smtWaitTime;
                    break;
                case State_SMT_Wait:
                    if(smtOverride == 0 && SMT_IN & SMT_IN_BIT) //fault: main didn't discharge
                    {
                        stopFiring();
                        lastFireResult = Result_MainFailedDischarge;
                        faultCount++;
                    }
                    else
                    {
                        lastFireResult = Result_FireSuccessful;
                        fireCount++;
                        if(currTimeout)
                        {
                            currTimeout--;
                            mod_status.ss_state = State_Cooldown;
                            TB0CCR1 += cooldownTime;
                        }
                        else
                            stopFiring();
                    }
                    break;
                case State_Cooldown:
                    CHARGE_OUT |= MAIN_CHARGE_BIT;
                    mod_status.ss_state = State_Main_Charging;
                    TB0CCR1 += mainChargeTime;
                default:
                    break;
            }
            break;
        default: break;
    }
}
```